

UC Merced

UC Merced Electronic Theses and Dissertations

Title

Numerical Simulation of Interactive Transport in a Proton Exchange Membrane Fuel Cell

Permalink

<https://escholarship.org/uc/item/42g5266c>

Author

Rahman, Md Azimur

Publication Date

2021

Copyright Information

This work is made available under the terms of a Creative Commons Attribution-NonCommercial-NoDerivatives License, available at <https://creativecommons.org/licenses/by-nc-nd/4.0/>

Peer reviewed|Thesis/dissertation

UNIVERSITY OF CALIFORNIA, MERCED

**Numerical Simulation of Interactive Transport in a Proton
Exchange Membrane Fuel Cell**

A Thesis submitted in partial satisfaction of the requirements
for the degree of Doctor of Philosophy

in

Mechanical Engineering

by

Md Azimur Rahman

Committee in charge:

Professor Po-Ya Abel Chuang, Chair

Professor Min-Hwan Lee

Professor Venkattraman Ayyaswamy

Professor James Palko

2021

© Md Azimur Rahman, 2021

All rights reserved.

This Thesis of Md Azimur Rahman is approved, and it is acceptable in quality and form for publication on microfilm and electronically:

Po-Ya Abel Chuang, Chair

Date

Min-Hwan Lee

Date

Venkatraman Ayyaswamy

Date

James Palko

Date

University of California, Merced

2021

To

My parents for their endless love and sacrifices.

ACKNOWLEDGEMENTS

I started my PhD with a very basic knowledge of PEMFC operation principles. Since day one Prof. Po-Ya Abel Chuang mentored me how to take little research steps to making big leaps and eventually being able to independently identify and solve research problems. I am immensely grateful to Professor Po-Ya Abel Chuang for all his guidance and suggestions through this journey. Without his help and support it would be impossible for me to finish this journey.

I would like to thank my PhD committee members Professor Min-Hwan Lee, Professor Venkattraman Ayyaswamy and Professor James Palko for providing technical feedback and supporting my research ideas.

In this long enduring journey, I was privileged to have my parents (Prof. Md Mizanur Rahman, Kawser Pervin) and wife Tahsin Salam Nodi by my side. Without their encouragement and support I would never have been able finish this work.

I want thank my colleague Felipe Mojica and Mrittunjoy Sarker for conducting the fuel cell experiments based on the design of experiments and for helping me understand the fuel cell experimental conditions. Thanks to Shirin Mehraji for providing the scanning electron microscopy images of gas diffusion media. In addition, I would like to thank Dr. Nitul Kakati for helping me understand the critical concepts related to fuel cell electrodes.

ABSTRACT

Proton exchange membrane fuel cell (PEMFC) is clean electrochemical energy generation device that generates electricity by electrochemical reactions between hydrogen and oxygen and the only byproducts of this reaction are heat and water. PEMFCs are considered to be the most promising technology to replace internal combustion engines for automotive application however for the commercialization of PEMFCs many technical challenges need to be overcome including decreasing Pt loading, increasing high current density performance, better water and thermal management and cell durability. Understanding the transport inside the PEMFC components are crucial for solving the technical challenges. In PEMFCs, most of the cell components are of nano to micro meter length scale which makes experimental characterization and diagnostics extremely difficult. Numerical models built on fundamental physics are critical for further development of this technology.

In my doctoral research I took a comprehensive simulation approach by first building a single-phase model, followed by expanding the physics towards two-phase simulation, and completed by a full down-the-channel model. At first a single phase steady state 1-D modeling framework is developed which accounts accurate membrane water balance considering electro-osmotic drag and back diffusion, non-isothermal heat transfer inside thin PEMFC components, oxide coverage dependent ORR kinetics, proton transport loss in electrode with respect to I/C ratio, convective and diffusive gas transport, shorting and cross over current to accurately capture open circuit voltage, effects of land/channel geometry on transport and non-fickian resistance in electrode and microporous layer.

Next to expand the modeling capability in high humidity or high current density operations two-phase water transport in the GDL and in electrode is added to the 1-D modeling framework. To model liquid water transport in the gas diffusion media, a novel approach has been proposed that only requires the GDL porosity and

tortuosity to formulate. To capture the effects of liquid water condensation in the electrode an empirical approach is adopted which correlates local water activity with catalyst utilization factor. The developed 1-D model establishes a robust modeling framework and it is validated with polarization and limiting current experimental results.

Finally, the 1-D two-phase model is expanded to a down-the-channel performance model to study the effects of stoichiometric flow rate, flow orientation (co-flow and counter-flow), channel pressure drop and coolant temperature on cell performance. The developed down-the-channel model can simulate species and current density distribution in along-the-channel direction and the results from developed 1+1-D model has been validated with experimental measurements from literature. In addition, parametric numerical studies on asymmetric GDL thickness, membrane thickness and asymmetric channel RH have been conducted to study internal water circulation mechanism. Down-the-channel simulation results show that counter-flow operation at low stoichiometric conditions enables efficient internal water circulation inside the cell, which improves membrane humidification and cell performance under extremely dry conditions. The findings from the newly developed model provide critical insights on the interaction of coupled heat and mass transfer, charge transport and down-the-channel distribution at realistic fuel cell operating conditions.

TABLE OF CONTENTS

ACKNOWLEDGEMENTS	ii
ABSTRACT	iii
LIST OF FIGURES	ix
LIST OF TABLES	xv
LIST OF SYMBOLS	xvi
1 INTRODUCTION	1
1.1 Motivation	1
1.2 Proton Exchange Membrane Fuel Cells	2
1.3 PEMFC Components	4
1.3.1 Flow-field	5
1.3.2 Gas diffusion layer	7
1.3.3 Microporous layer	7
1.3.4 Catalyst layer	8
1.3.5 Membrane	10
1.4 Technical Challenges	11
1.5 Research objectives and approach	13
1.6 Thesis outline	15
2 LITERATURE REVIEW	16
2.1 PEMFC models with gas phase transport	17
2.2 PEMFC models with liquid water transport	19
2.3 Down-the-channel distribution models	21
2.4 Summary	22

3	EXPERIMENTS	25
3.1	Materials	25
3.2	Fuel cell tests	26
4	DEVELOPMENT OF 1-D MODEL	29
4.1	Modeling domain	29
4.2	Reversible cell voltage	30
4.3	Hydrogen oxidation reaction (HOR)	30
4.4	Oxygen reduction reaction (ORR)	31
4.5	Charge transport	32
4.5.1	Proton transport in membrane	33
4.5.1.1	Water uptake	36
4.5.1.2	Electro-osmotic drag	36
4.5.1.3	Water back-diffusion	37
4.5.2	Membrane water balance and membrane ohmic loss	38
4.5.3	Proton transport electrode	39
4.5.4	Electron transport	41
4.5.5	Shorting and cross-over	42
4.6	Mass transport	42
4.6.1	Mass transport in channel	42
4.6.2	Mass transport in GDL	44
4.6.2.1	Fick's diffusion in porous GDL	44
4.6.2.2	Mixture diffusivity calculation	44
4.6.2.3	Effective diffusivity in porous media	45
4.6.2.4	Land and channel geometric effect	46
4.6.3	Mass transport in MPL	48
4.6.4	Mass transport in CL	48
4.6.5	Calculating mass transport loss	49
4.7	Heat transfer	51

4.8	Solution algorithm	52
4.9	Results: 1-D Dry Model	54
4.9.1	Simulation comparison with limiting current tests	54
4.9.2	Simulation comparison with polarization test	56
4.9.3	Impact of coupled heat and mass transfer	56
4.9.4	Dry Oxygen transport resistance	60
4.10	Investigation water transport in GDL	63
4.10.1	Experimental Observations	64
4.10.2	1-D modeling analysis	65
4.11	Summary	68
5	MODELING TWO-PHASE WATER TRANSPORT	69
5.1	Water tendril model in the GDL	69
5.1.1	Two-phase heat transfer	73
5.1.2	Boundary Conditions	73
5.2	Local oxygen transport resistance	74
5.3	Results: 1-D Wet Model	75
5.3.1	Experimental validation of the tendril model	75
5.3.2	Additional Performance losses	77
5.3.3	Polarization experiment	81
5.3.4	GDL and electrode flooding	82
5.3.5	Effect of membrane water transport properties on tendril model	85
5.4	Summary	87
6	DEVELOPMENT OF DOWN-THE-CHANNEL MODEL	90
6.1	Down-the-Channel Framework	90
6.2	Channel discretization	90
6.3	Results: Down-the-Channel Model	94
6.3.1	Experimental validation	94

6.3.2	Effect of Stoichiometry and Flow-orientation on PEMFC performance	94
6.3.3	Down-the-channel distribution	97
6.4	Investigation of water balance	100
6.4.1	Asymmetric GDL	101
6.4.2	Membrane thickness	101
6.4.3	Asymmetric channel inlet RH	102
7	CONCLUSION	109
8	FUTURE WORK	113
 APPENDIX		
A	115

LIST OF FIGURES

1.1	Schematic of fuel cell $i - V$ curve showing major voltage loss regions	3
1.2	Schematic diagram of PEMFC components and their corresponding functions (image obtained from Yuan et. el. [159]).	5
1.3	Conventional fuel cell flow field designs (a) straight parallel (b) multiple channel serpentine (c) single channel serpentine [99]	6
1.4	Microscopic images of (a) Toray TGP-H-060 and (b) Freudenberg H23C8 gas diffusion layer [28]	8
1.5	Microscopic images of (a) micro porous layer and (b) micro porous layer coated on gas diffusion layer	9
1.6	Schematic representation of the catalyst layer elements and the pathways for electron, proton and oxygen transport.	10
1.7	Current challenges in PEMFC technology based on DOE report [35]	12
4.1	Modeling domain for the 1-D PEMFC model and through plane transport processes	30
4.2	Experimentally measured Pt-oxide coverage by subramanium et. al. [131]	32
4.3	Tafel slope determined from the Pt-Oxide coverage dependent ORR kinetics model	33
4.4	Chemical structure of Nafion membrane showing the PTFE backbone for mechanical stability and sulfonic acid groups for proton conduction. (Image source: O'Hayre et. al. [106])	34

4.5	Conductivity of Nafion vs water uptake based on the experimental measurements by Springer et. al. [130]	35
4.6	Conductivity of Nafion vs temperature showing exponential correlation	35
4.7	Membrane water uptake (λ) with respect to membrane water activity a_w	37
4.8	Schematic diagram of convective mass transport in PEMFC channels showing in-plane and through plane transport process.	43
4.9	Sherwood number for various channel cross section under laminar flow region where $\alpha = b/a$ (obtained from O'hayre et. al. [106])	44
4.10	Schematic representation of tortuosity in porous diffusion media	46
4.11	Computational domain and boundary condition for modeling the geometry effect of land and channel in PEMFC diffusion media	47
4.12	Comparison of parallel Knudsen and molecular diffusivity vs pure molecular effective diffusivity of Oxygen at 150kPa 80°C	49
4.13	Thermal resistance network and heat flux direction for the through plane heat transfer in PEMFC	52
4.14	Solution algorithm for solving the governing equations of the 1-D PEMFC model	53
4.15	(a) Validation with dry polarization results at limiting current conditions of 150 kPa, 80°C and 62% RH. (b) Oxygen dry mole fraction at four different pressures at 80°C and 64% RH. (c) Dry transport resistance plotted as a function of total pressure (<i>solid line represents simulation and symbols represent experiment</i>)	55
4.16	Model validation with dry polarization performance at three different operating conditions	57
4.17	Effect of water balance, electrode proton transport loss, non-isothermal heat transfer, mass transport iteration on PEMFC modeling	58

4.18	Temperature distribution in the PEMFC sandwich at three different current densities	60
4.19	Membrane water uptake, λ , distribution in the membrane at three different current densities	61
4.20	Simulation results of transport resistance contribution of diffusion media, channel and non-fickian resistances	62
4.21	Limiting current as a function oxygen dry mole fraction for (a) Toray TGP-H-060 and (b) Freudenberg H23C8 and (c) the comparison of oxygen transport resistance as a function a pressure at 80 °C and 64 % RH.	63
4.22	Wet oxygen transport as a function of relative humidity and limiting current for (a) Toray TGP-H-060 and (b) Freudenberg H23C8 at 70 °C and 300 kPa.	64
4.23	Simulation results of (a) Water vapor and saturation pressure and (b) Relative humidity distribution in Toray TGP-H-060 and Freudenberg H23C8 at 1.50 $A\ cm^{-2}$, 300 kPa, 70 °C and 90 % RH.	66
5.1	Experimental results from limiting current result showing the change of Oxygen transport resistance with increase in limiting current density at 300 kPa 70°C 90% RH	70
5.2	Schematic representation of water transport in GDL based on Caulk and Baker's [22] water tendrils model (a) partially wet GDL ($t_{tendrils} < t_{GDL}$) (b) fully wet GDL ($t_{tendrils} = t_{GDL}$)	71
5.3	Comparison of 1-D simulation results with limiting current experiment for Oxygen transport resistance under (a) dry operating condition, 100-300 kPa, 80°C, 64% RH (b) wet operating conditions 300kPa 70°C 80/90% RH (c) polarization performance compared with 1-D dry and 1-D dry with water tendrils model under wet operating condition 300kPa 70°C 90%RH	76
5.4	Experimental results showing rapid performance loss due to low catalyst utilization at electrode flooding at 300kPa 70°C 90%RH. Shaded region represents the performance loss not captured with GDL tendrils model.	78

5.5	Simulated catalyst utilization factor with local water activity in the electrode at different wet operating conditions at 300kPa 70°C 90%RH.	80
5.6	Simulation of polarization performance at 300kPa 90%RH, 70°C showing the performance comparison between dry and two-phase PEMFC model.	82
5.7	1-D simulation of water tendril growth in GDL with increasing limiting current density at 300 kPa 70°C 80%, 90%RH.	84
5.8	Simulation result of local water activity and liquid water coverage in electrode at 300 kPa 70°C and 90%RH	85
5.9	Simulation of Oxygen transport resistance with different values of electro-osmotic drag [39, 160, 123, 41, 62] reported on literature. . .	87
5.10	Simulation of Oxygen transport resistance with different values membrane water diffusivity [20, 40, 160, 100, 98] reported on literature.	88
6.1	Implementation of co-flow orientation with the resistance network of the 1+1-D model where multiple 1-D cells are represented by electric circuits coupled with the gas flow in the flow-channels . . .	91
6.2	Counter-flow orientation implementation of the 1+1-D model where multiple 1-D cells are represented by electric circuits coupled with the gas flow in the flow-channels	92
6.3	Solution algorithm for obtaining equipotential cathode BP and current density distribution in the down-the-channel model.	95
6.4	Pseudo code showing the algorithm for obtaining equipotential cathode bipolar plate	96
6.5	Down-the-channel current distribution experiment and model predictions at 1.50 A/cm ² current density and counter-flow orientation. Operating condition 176 kPa 30/60%RH 80°C, Pressure drop 30/45 kPa, Coolant temperature difference 7.8°C	97

6.6	1+1-D simulation result showing the effect of stoichiometric flow rate on PEMFC under dry operating conditions with co-flow and counter-flow orientation. Operating condition: 150 kPa 80°C, 20% RH (Dry), 100%RH (Wet), Pressure drop 30/45 kPa, Coolant temperature difference 7.8°C	98
6.7	1+1-D simulation result showing the effect of stoichiometric flow rate on PEMFC under wet operating conditions with co-flow and counter-flow orientation. Operating condition: 150 kPa 80°C, 20% RH (Dry), 100%RH (Wet), Pressure drop 30/45 kPa, Coolant temperature difference 7.8°C	99
6.8	Down-the-channel current distribution at 1.50 A/cm ² applied current density and counter-flow orientation. Operating condition 150 kPa 20/20%RH 80°C, Pressure drop 30/45 kPa, Coolant temperature difference 7.8°C	100
6.9	Down-the-channel distribution of (a) water transport from cathode to anode (b) HFR at co-flow and counter-flow orientation for stoichiometric flow rates of 2 and 10. Operation conditions: 150 kPa 80°C 20% RH.	103
6.10	Relative humidity distribution in down-the-channel direction at stoich of 10 and 2 for (a) co-flow orientation (b) counter-flow orientation. Operation conditions: 150 kPa 80°C 20% RH.	104
6.11	Down-the-channel distribution of (a) cathode to anode water transport (b) channel relative humidity with varying anode/cathode GDL thickness at 150 kPa 80°C, 20% RH	105
6.12	Effect of GDL thickness on along the-channel distribution of (a) membrane water uptake (b) HFR distribution at at 150 kPa 80°C, 20% RH	106
6.13	Effect of membrane thickness on along the-channel distribution of (a) membrane water uptake (b) HFR distribution at at 150 kPa 80°C, 20% RH	107
6.14	Down-the-channel distribution of (a) cathode to anode water transport (b) channel relative humidity with varying membrane thickness at 150 kPa 80°C, 20% RH	107

6.15	Effect of asymmetric channel inlet RH on (a) membrane water uptake (λ) (b) membrane proton transport resistance (HFR) at at 150 kPa 80°C, 20% RH	108
6.16	Effect of asymmetric channel inlet RH on (a) water transport from cathode to anode (f_w) (b) RH distribution in the down-the-channel direction at at 150 kPa 80°C, 20% RH	108
A.1	Iteration loops for calculating fraction of generated water transported towards anode side from cathode side	116
A.2	Iteration loops for solving 1-D heat equation	117
A.3	Iteration loop for solving 1-D mass conservation equation	118

LIST OF TABLES

3.1	Single cell 2 cm ² testing protocol.	26
4.1	Parameters for 1-D simulation	41
4.2	Diffusion properties of common PEMFC gases [153].	45
4.3	Through-plane thermal conductivity and gas diffusivity of the GDL in Toray TGP-H-060 and Freudenberg H23C8.	65
5.1	Simulation parameters for the water tendril, ORR kinetics and electrode catalyst utilization model	83

LIST OF SYMBOLS

C	Molar concentration, mol/m^3
D_{OM}	Diffusion coefficient in open media, cm^2/s
$D_{i,mix}$	Diffusivity of component i in mixture
D_h	Hydraulic Diameter
f_{geo}	Factor to include increased diffusion length reactant travel under the land
f_w	Fraction of water transported from cathode to anode
f_t	Factor for electrode thickness calculation
F	Faraday constant
h_m	Convective mass transfer coefficient
Δh	Thermal conductivity, W/m-K
Δg	Reaction Gibb's free energy, kJ/mol
Δs	Reaction Entropy, kJ/mol
$(\frac{I}{C})$	Ionomer to Carbon weight ratio in electrode
i_0	Exchange current density, A/cm^2
n_i''	Molar flux of species i
K_i	Thermal conductivity of material i , $\frac{mol}{cm^2s}$
EW	Membrane equivalent weight
n_{drag}^{sat}	Electro-osmotic drag coefficient
P	Pressure, Pa
Q_i	Heat flux of i
rf	Roughness factor, $cm_{pt}^2/cm_{geometry}^2$
RH	Relative humidity
R_{other}	Pressure independent transport resistance, s/cm
R_{sheet}	Proton transport resistance in electrode
a_w	Water activity
P_{sat}	Water saturation pressure, Pa
T	Temperature, K
v	Diffusion volume
X_i	Mole fraction of i
D_λ	Water diffusivity in membrane, cm^2/s
δ_i	Thickness, cm
ϵ	Porosity

κ	Ionomer conductivity in electrode, S/cm
η	Voltage loss/Overpotential, V
λ	Membrane water content
ρ_i	Density of i
α	Transfer coefficient
σ	Conductivity, S/cm
τ	Tortuosity
ζ	Correlation factor for effective proton transport resistance in cathode
ω	Mass fraction
θ_{PtOx}	Pt oxide coverage of cathode electrode
θ_w	Liquid water coverage in cathode electrode
χ	Normalized roughness factor

Chapter 1

INTRODUCTION

Since the industrial revolution in the 19th century, CO₂ levels in atmosphere has been rising consistently. The increase of CO₂ emission has contributed largely to the greenhouse effect. In the last 100 years the temperature of the earth has increased more than 1 degree Celsius. The temperature shift has forced us to face the biggest challenge of 21st century, “Climate change”. EPA data [3] from 2013 has shown that in United States the transportation, energy and industrial sector account for more than 70% of the total CO₂ emission. In fact, the transportation sector alone contributes to a one third of total CO₂ emission. Therefore finding a clean power train device for transportation industry is critical for reduction CO₂ emission.

1.1 Motivation

Two most promising technologies to replace internal combustion engines are batteries and fuel cells and both are electrochemical devices that produce electrical power by converting chemical energy. Fuel cells combine hydrogen and oxygen by electrochemical reaction to generate electricity. It can be viewed as an “open” thermodynamic systems. The fuel cell engine can generate electricity as long as it is continually supplied with fuel and oxidizer. If the operating condition are maintained, fuel cells can effectively produce a constant current at a constant voltage. In contrast batteries are “closed” thermodynamic systems that stores a finite amount of chemical energy. As electrical energy is drawn from the battery, the reactants deplete and the battery efficiency is decreased. Essentially battery is a energy storage device and the only possibility to increase energy storage capacity is by increasing the battery size, which includes volume and weight. This is a major setback for the use of battery in automotive applications with heavy duty cycle (bus or trucks) or

long drive cycle (highway driving). In addition, battery charging time is also a concern for automotive applications. Due to this inherent operational characteristics, battery based technologies alone are not sufficient to completely replace internal combustion engines.

Fuel cell was originally discovered by a Welsh Physicist William Grove in 1839. Since then fuel cell technology has gained significant attention from scientists and researchers. Due to the advancement in nanotechnology, fuel cell technology had made substantial improvement in performance, durability and cost. There are different fuel cell technologies currently under development. They can be differentiated based on their electrolyte and operating temperature range. The major fuel cell types are : Proton exchange membrane fuel cell (PEMFC), solid oxide fuel cell (SOFC), alkaline fuel cell (AFC), direct methanol fuel cell (DMFC), phosphoric Acid fuel cell (PAFC) and molten carbonate fuel cell (MCFC). Even though all fuel cells the work based on the same electrochemical principles, they can operate at different temperature range, use different materials and the performance can also vary a lot. PEMFC is the only fuel cell type that can operate at a low temperature range ($< 100^{\circ}C$) with high power density. Proton exchange membrane fuel cell was first used in 1960s for NASA's Gemini space flights for their first manned spaceship [145]. It was developed by General Electric in USA and had a lifetime of 500 hour, catalyst loading of 28 mg/cm^2 compared to 4000 hour and $< 0.15 \text{ mg/cm}^2$ of current PEMFCs [11]. Beside the operating temperature PEMFC also has several other advantages like fast start-up, quick refueling time and durability[19, 109, 117, 61, 157]. Because of these advantages, most automotive companies consider PEMFCs as one of the most clean and sustainable technology for automotive applications.

1.2 Proton Exchange Membrane Fuel Cells

A PEM fuel cell has the following reactions. In anode side Hydrogen is supplied as fuel and hydrogen oxidation reaction (HOR) occurs as shown in equation 1.1. In cathode side generally air is supplied and the oxygen participates in Oxygen reduction reaction (ORR) shown in equation 1.2.



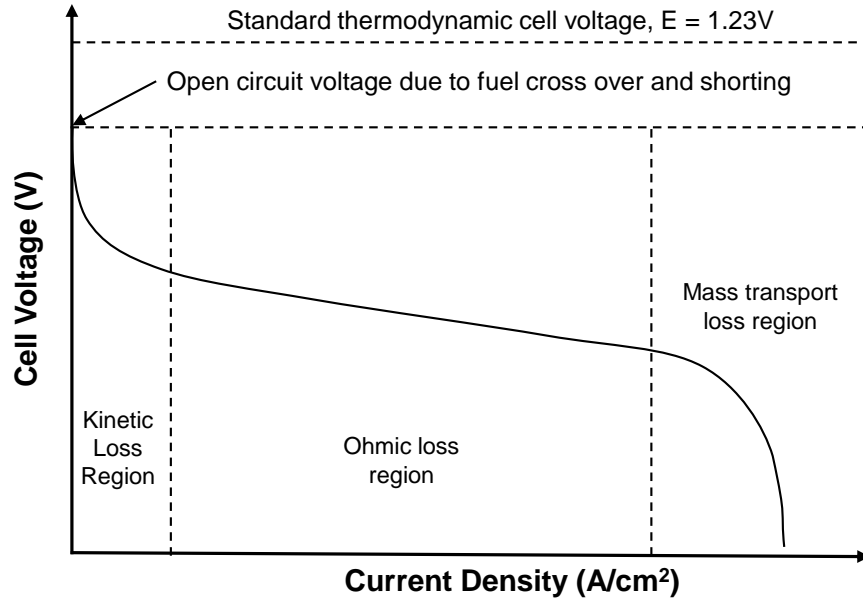
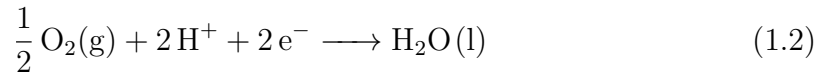
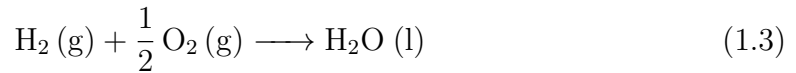


Figure 1.1: Schematic of fuel cell $i - V$ curve showing major voltage loss regions



The net exothermic reaction can be written as



PEMFC generates electricity and the byproducts are waste heat and water. Reactants are transported by diffusion and convection to the electrodes surface where the electrochemical reactions take place.

A schematic of fuel cell performance $i - V$ curve is shown in figure 1.1. The voltage output of a fuel cell is always less than thermodynamically predicted cell voltage. Like any other system in universe, fuel cells also go suffer through irreversible losses. These losses increases as more current is drawn from the cell. Three major losses can be clearly identified in figure 1.1. At low current densities cell performance loss is mainly due to activation loss. Activation loss occurs due to electrochemical reactions. Electrochemical reaction involve charge transfer and the current generated is proportional to reaction rate. To achieve higher current more

reactants need to be converted to products. A portion of cell voltage is compromised to lower the activation barrier for the conversion of reactants to products. This is known as activation loss. In $H_2 - O_2$ fuel cell hydrogen kinetics are generally 4 to 5 orders of magnitude higher than oxygen reduction kinetics. The sluggish reaction kinetics of oxygen is the major contributor to activation loss. As current density is further increased ohmic losses are dominant. Ohmic loss refers to the voltage losses due to ionic and electronic conduction. Protons are generated in the anode electrode during the HOR reaction. To complete the ORR reaction, the protons need to transport through the anode, membrane and cathode electrode. This causes a major voltage loss in intermediate current density. Proton conduction in the ionomer is strongly coupled with local water content. So a proper balance between cell hydration and flooding is critical. As current density is further increased, the cell performance drops due to mass transport loss. Mass transport loss occurs due to reactant (H_2 , O_2) depletion in the electrode. Under dry operating condition, reactant depletion occurs due to insufficient reactant supply. However under wet operating condition or high current density, liquid water may condense in the electrode or GDL. This blocks the pathway for oxygen diffusion and results in a reactant depletion in the electrode. However, these are three operational regions of PEMFC.

1.3 PEMFC Components

A PEMFC generally consists of a proton exchange membrane, two electrodes (anode and cathode), gas diffusion layer (GDL) and flow field (FF). These layers are compressed together to form a PEMFC sandwich. The membrane and the two electrodes are often commonly referred as the membrane electrode assembly (MEA). The electrodes are typically made out of carbon, ionomer and catalyst particles and is considered as the heart of the fuel cell where all electrochemical reactions occur. Between the electrode and the flow field a gas diffusion media is used. The purpose of the gas diffusion media is to transport oxygen to the electrode, remove product water and conduct electron. Flow field is assembled right after the gas diffusion media. The primary functions the flow field in PEMFCs are to supply fuel and oxidant to the reaction sites, remove product water, transport heat and electrons and provide mechanical support to MEA. But flow fields mostly transport reactants

and products by convection. A schematic diagram for PEMFC components is shown in figure 1.2.

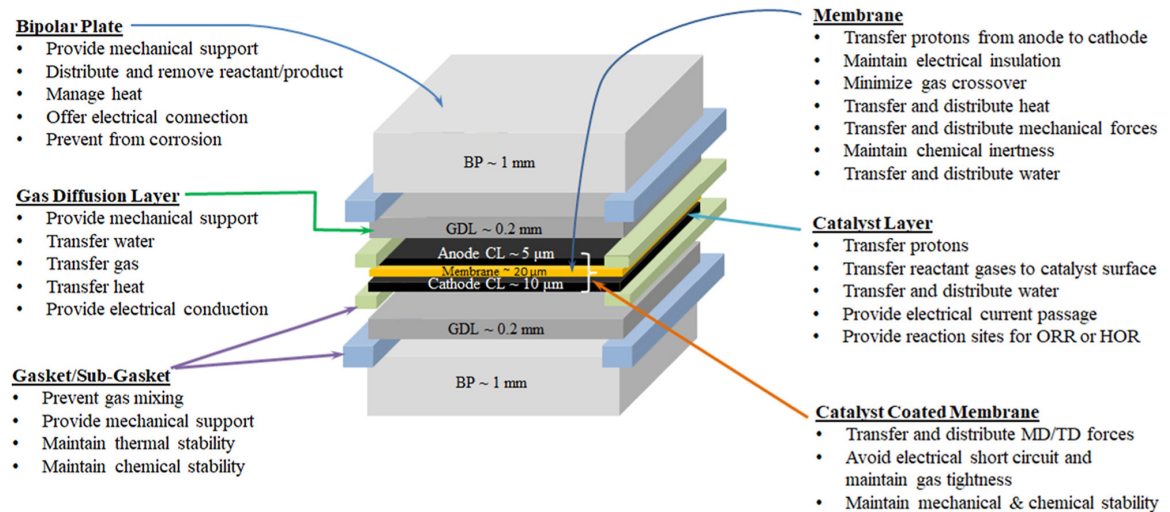


Figure 1.2: Schematic diagram of PEMFC components and their corresponding functions (image obtained from Yuan et. el. [159]).

1.3.1 Flow-field

Flow field is one of the most important component of fuel cell. It performs several important tasks such as:

- Supplying reactant gases to the MEA.
- Collecting the generated current
- Removing the generated water
- Removing waste heat
- Uniformly distributing reactants
- Providing mechanical support to the cell

For a given MEA the flow field design can heavily impact the the cell performance. Desirable flow field designs uniformly distribute reactant gases and also prevent flooding by removing the generated water as non-uniform reactant distribution or

flooding can cause higher ohmic and mass transport losses. To improve the reactant distribution flow fields designs are often optimized with channel geometric parameters, such as width, length, depth, cross-sectional shape, and crosssection profile from inlet to exit. Simplest form of channel designs are straight parallel or serpentine type as shown in figure 1.3. In recent years more novel channel designs has been proposed and auto manufacturers often use more intricate and complex flow field designs to improve performance. However, complex flow field designs often comes at cost of high pressure drop which requires higher pumping power.

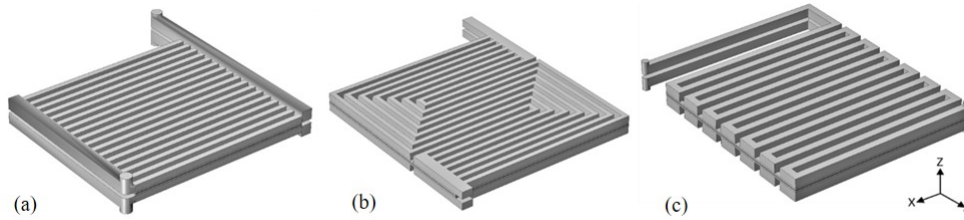


Figure 1.3: Conventional fuel cell flow field designs (a) straight parallel (b) multiple channel serpentine (c) single channel serpentine [99]

Flow fields also need to have high electrical and thermal conductivity so that the generated current can be collected with minimal voltage loss and the heat can be removed easily too. To achieve this goal flow fields are generally made of materials which have high electrical and thermal conductivity such as metals or graphite. Metals can be an excellent candidate as they have high electrical and thermal conductivity, they are low cost and easy to manufacture materials. But operating environment inside the PEMFC is highly corrosive with low pH levels, high humidity and high temperatures. At such harsh conditions typical metals aluminum or steel starts to corrode and the metal ions from corrosion diffuse to the fuel cell membranes which degrades the membrane and reduce durability [51]. To solve this issue graphite is used for flow field material even though the conductivity is order of magnitude lower than metals and the manufacturability is not as easy as the metals. In addition a large fraction of PEMFC stack weight comes from flow fields and stack performance and durability is also highly dependent on flow field designs.

1.3.2 Gas diffusion layer

The gas diffusion layer (GDL) is a porous gas transport layer that is sandwiched between the electrode and the flow field. It performs four major tasks during PEMFC operation including oxygen transport, electron conduction, product water removal and providing mechanical support to cell compression loads. Carbon based products such as woven carbon cloth, non-woven carbon paper or carbon foam is typically used to fabricate GDLs as carbon is highly conductive and stable in acidic environment. The pores in the GDL provides pathways for Oxygen to diffuse from the flow channels towards the electrode and the highly conductive carbon fibers conduct the electron to the bipolar plates. GDL also removes the product water from the electrode and plays a crucial role in the overall water management of the cell. GDL can transport water in both liquid and vapor form and it is typically wet-proofed by a hydrophobic agent PTFE to make the surface and pores in the GDL hydrophobic. The micro-structure of the GDL such as fiber orientation, pore structure and size distribution can vary significantly between GDLs from different manufacturers. A microscopic image of two commercially available gas diffusion layer Toray and Freudenberg is shown in figure 1.4.

In general, the goal of a PEMFC is to generate higher current density and a higher current density operation will require higher flux of reactant gases and product water removal. So optimizing gas diffusion layer properties is critical for effectively transporting the gases to the electrode [112, 154].

1.3.3 Microporous layer

Microporous layer (MPL) is one of the more recent developments in PEMFC technology and it is often considered an extension of the GDL as the inclusion of this layer is optional for PEMFC operation. The microporous layer is a thin layer made of fine carbon black powder and PTFE and it is typically coated on the GDL. This layer has high PTFE content generally more than 20% and as a result it exhibits extreme hydrophobicity with a contact angle of more than 120°. Different kind of carbon powder is used to fabricate MPL such as Vulcan or Acetylene black and the pores sizes in MPL is also one or two order of magnitude lower than the GDL with mean pore radius being in the range of 80-150 nm [108]. Because of its small pore diameter gas in the MPL is primarily transported by knudsen diffusion instead

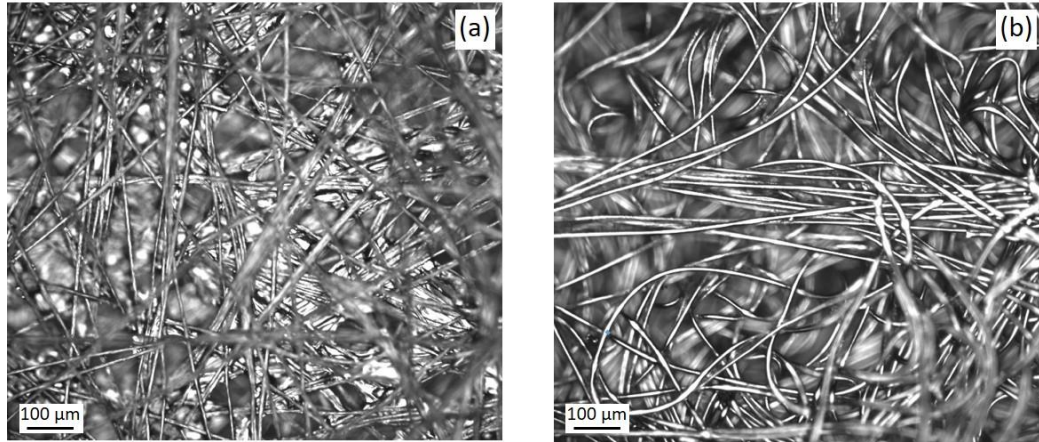


Figure 1.4: Microscopic images of (a) Toray TGP-H-060 and (b) Freudenberg H23C8 gas diffusion layer [28]

of molecular diffusion. The MPL gets in contact with the electrode providing a much lower thermal and electrical contact resistance compared to bare GDL [135]. MPL has been extensively studied in literature and several performance advantages of the MPL has been clearly identified all though exact physical mechanisms for these performance gain is still not well understood. Firstly, MPL lowers electronic contact resistance by providing better contact with the electrode and it also keeps the membrane hydrated during dry operation [147]. Both of which reduces the ohmic loss during cell operation. In addition, MPL is critical to improve mass transport losses at high humidity operation as it helps to reduce flooding levels in the cell. Finally MPL acts as a buffer region between the GDL and the electrode in terms of structural stability [147].

1.3.4 Catalyst layer

The catalyst layer (CL) in PEMFCs is a highly porous layer where all the chemical reaction takes place and it is the most important component of the cell. CL remains in direct contact with the MPL and membrane and it usually comprises of the following elements

- Catalysts (Platinum group metal (PGM) or PGM free)
- Electron conducting medium such as carbon to support the metal catalysts

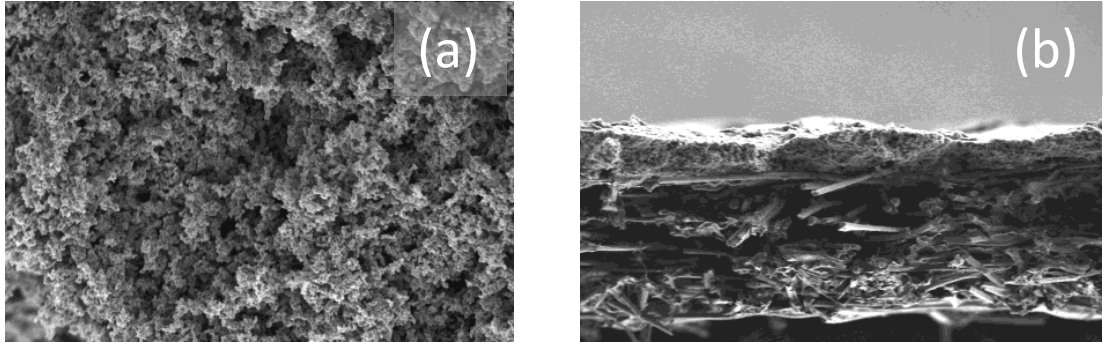


Figure 1.5: Microscopic images of (a) micro porous layer and (b) micro porous layer coated on gas diffusion layer

- Perfluorosulfonate acid (PSFA) ionomer binders that provide pathway for proton transport

In addition often a hydrophobic agent such as polytetrafluoroethylene (PTFE) is also added to improve liquid water removal capability of the catalyst layer [86]. The carbon, Pt and ionomer binders form agglomerates of different size and shapes inside the catalyst layer which results in a porous catalyst structure which is necessary to achieve high electrochemical reaction surface area [25, 23]. The large pores inside the CL are called secondary pores and the small pores are called primary pores. The catalyst layer is present both on anode and cathode side. In anode CL the hydrogen oxidation reaction (HOR) takes place which converts hydrogen to protons and releases two electrons whereas in cathode oxygen is reduced to water with a four electron process in the oxygen reduction reaction (ORR). Even though both HOR and ORR are both heterogeneous electrochemical reactions the reaction rate for HOR is several orders of magnitude higher than the ORR reaction. As a result HOR reaction is completed without a very significant voltage loss for the cell. The ORR reaction on the other hand is significantly more complex and exhibits a lot slower reaction rates. For the ORR reaction to take place, electrons, protons and oxygen need to meet at the Pt catalyst surface and the location where these three phases meet (e^- , H^+ and O_2) is called the triple phase boundary [44]. The waste heat from the reaction is transferred through solid carbon matrix and the gases in the pores. Depending the local electrode condition product water from the reaction may exist in several different phases like vapor, liquid or adsorbed in ionomer.

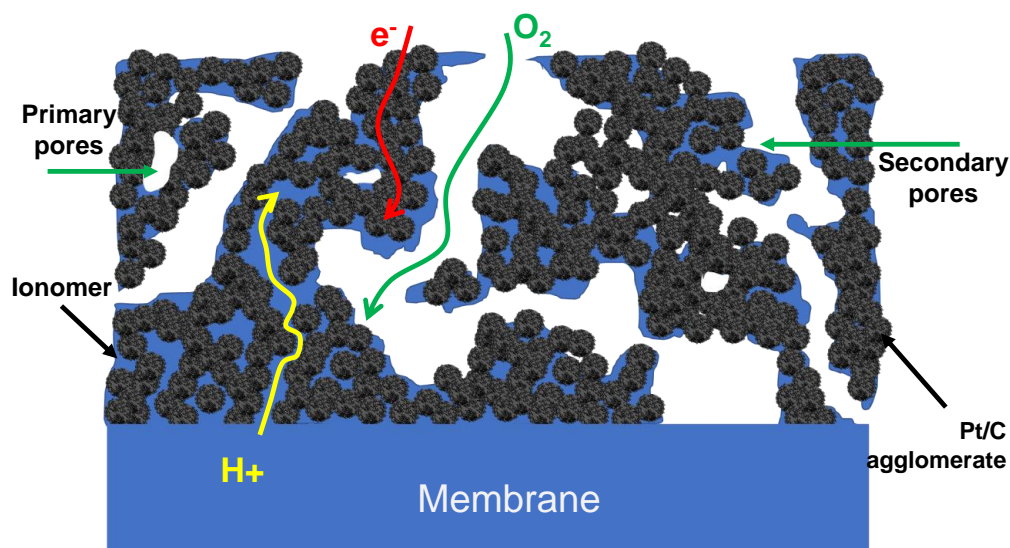


Figure 1.6: Schematic representation of the catalyst layer elements and the pathways for electron, proton and oxygen transport.

PEMFCs employ a acidic environment with humidified PFSA ionomers. In such adverse environment Pt or Pt-based alloys are the only catalyst which have exhibited high specific/mass activity for the slow ORR reaction. However the Pt is an extremely precious metal and the use of Pt in PEMFC catalyst layers makes the technology very expensive for commercialization. In order to reduce the cost of the PEMFC system much extensive research effort is currently put into reducing the amount of Pt (Pt loading) in the CL and to the search for alternative inexpensive PGM free catalysts. Many PGM-free catalysts have been studied in literature such as heteroatom-doped carbon, transition metal oxides, nitrides or carbides, transition metal-nitrogen-carbon which is often abbreviated as M-N-C catalysts where M=Fe, Co, Ni, Cu, Mn. Among various PGM-free catalysts Fe-N-C catalysts have shown great promise with improving catalytic activity [143].

1.3.5 Membrane

The PEMFC membrane is a polymer made of tetrafluoroethylene (PTFE) and perfluorocarbon-sulfonic acid (PSFA) ionomer. The catalyst layers are coated on boths sides of the membrane and the membrane electrode assembly is generally

known as the MEA. PEMFC membranes only conduct protons and exhibit high protonic conductivity. They are also highly impermeable to gases and act as the barrier for gas cross-over. Most commonly used commercial membrane is Nafion from DuPont. Other commercial membranes include Asahi Glass (Flemion), Asahi Chemical (Aciplex) and Dow Chemical. W.L. Gore associates (GoreSelect). Regardless of the manufacturer in all membranes the PSFA ionomers act as the proton conductor whereas the PTFE backbone provides the mechanical integrity. Nafion membranes can absorb high amount of water and they generally swell with higher water content. Water can transport through the membrane in dissolved form and the conductivity of the membrane is a strong function water content. Since the protons need to travel the total thickness of the membrane to reach cathode catalyst layer the thickness of the membrane plays a crucial role in voltage loss from proton transport. To reduce the voltage loss very thin nafion membranes are used (15-25 micron). The water transport mechanisms and conductivity of membrane is discussed in detail in section 4.5.1.

1.4 Technical Challenges

Several challenges need to be solved for the commercialization PEMFC technology. Based on Department of Energy's fuel cell status report [35], major challenges currently faced in PEMFC technology are shown in figure 1.7 shows the current challenges. Broadly the current challenges can be divided into fuel supply and PEMFC technology itself. One of the major issue that is impeding PEMFC commercialization in automotive sector is the supply of hydrogen fuel. Even though hydrogen is the most abundant element in the universe we do not get pure hydrogen in environment. Common hydrogen generation techniques all have different challenges . In addition hydrogen is the smallest element of the periodic table and as a result transport and storage of hydrogen is very difficult . For a sustainable and reliable hydrogen fuel supply, efforts from both research sector and policy makers are necessary.

Fuel cell degradation is another challenge that has drawn much attention from researchers recently. The PEMFC used in NASA's gemini spaceship in 1960s had a lifetime of 500h only. Current fuel cells have a lifetime of 2500h which is a big improvement. But the DOE target for 2020 is to achieve a lifetime of 5000h.

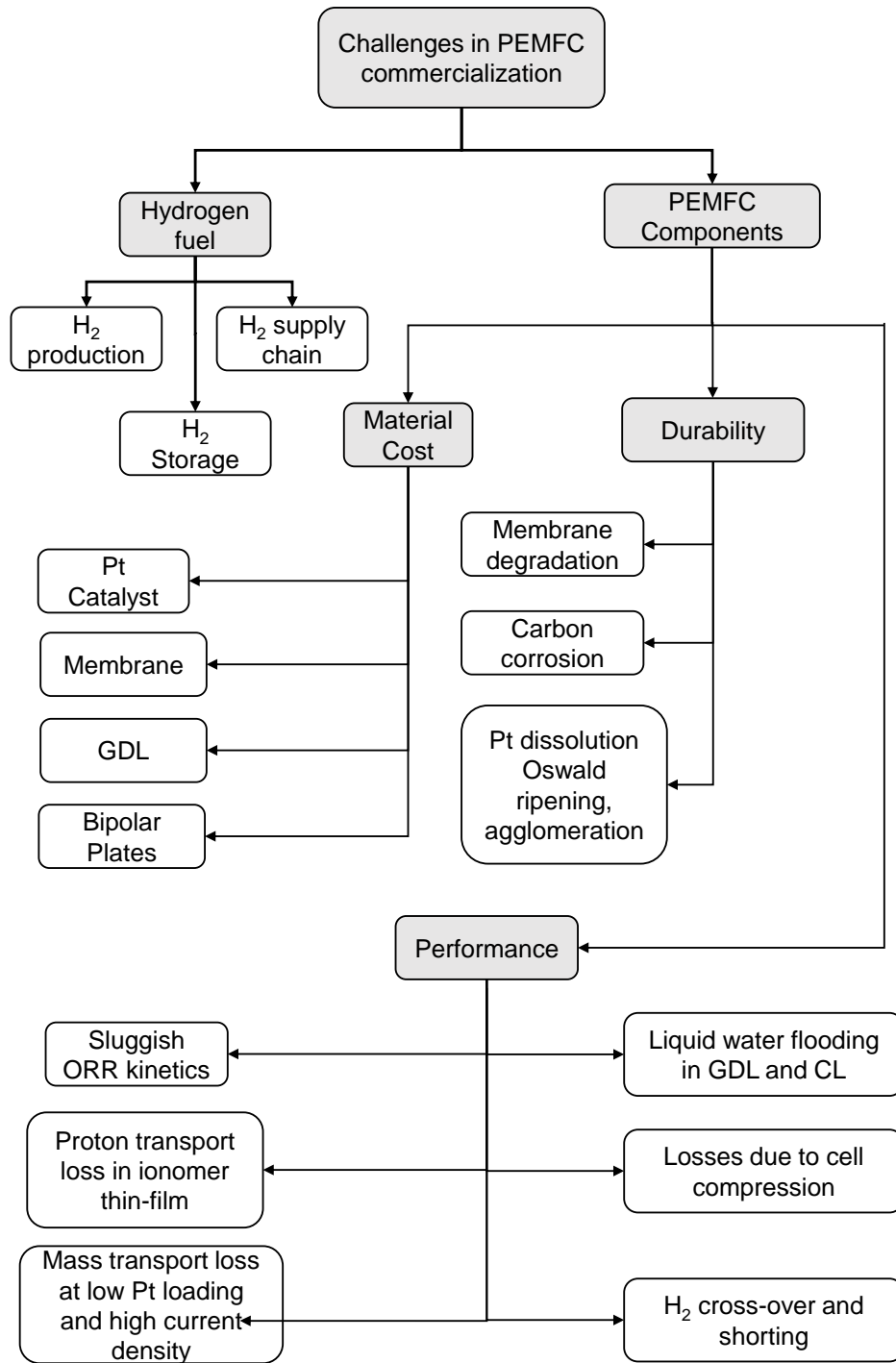


Figure 1.7: Current challenges in PEMFC technology based on DOE report [35]

Lastly, the major focus for PEMFC research now is cost reduction. As shown in figure 1.7 major cost drivers for PEMFC are the Pt-catalyst used in cathode electrode, gas diffusion media, membrane and the bipolar plates. Majority of the performance loss originates in the cathode side due to the sluggish reaction kinetics of oxygen reduction reaction. To overcome this issue expensive catalyst materials such as Pt in the electrode. A large share of PEMFC research is currently devoted to finding inexpensive Pt group metal (PGM) free catalyst material to reduce the cost.

Besides electrode, improving the power density of the cell is another challenge. To achieve high power density PEMFCs need to be operated at a high current density (HCD). However, at HCD operation several complex phenomena occur at the same time which makes the performance optimization process extremely challenging. To improve PEMFC performance under HCD operation, understanding the transport phenomena inside the cell is important. Most of the PEMFC components are nano to micro scale thin. Due to this small scale issue, experimental tools are often not adequate to understand transport. Numerical models can be very effective in modeling transport inside these components and providing new insights. The aim of this research is to develop a PEMFC model that can be used a performance diagnostic and material optimization tool.

1.5 Research objectives and approach

PEM fuel cell operation is a multi-scale and multiphysics phenomena. The length scale spans from few nano meters in the catalyst layer to few hundred microns in the gas diffusion media. The complex interaction of mass, heat and charge transport in such small scale makes it an extremely challenging problem to solve. For efficient operation, the reactant gases (H_2 and O_2) need to be transported from the flow channels to the reactions sites which is achieved by convective and diffusive mass transport. The protons generated in anode side also need to be transported to the reaction sites in the cathode to complete the electrochemical reaction and the transport of protons is a complex interactive problem between mass, heat and charge transport. In addition, the product water may condense inside the GDL or in the catalyst layer which hinders mass transport significantly and causes rapid decline in PEMFC performance. The electrochemical reaction also generates waste

heat which impacts all the aforementioned events. Understanding the complex interaction of these physics is critical for improving fuel cell performance and reducing the cost of the system.

The nano to micrometer length scale of the PEMFC components makes it extremely difficult to make in-situ measurement and characterization of the transport processes. Due to this limitations mathematical models are critical to understand the interactive transport phenomena in PEMFCs. However there is significant knowledge gap in the current PEMFC mathematical modeling literature particularly in two-phase water transport modeling in the GDL and in electrode and simulation PEMFCs under realistic operating conditions. In order to address this gaps the research objectives of this thesis are to :

- Study liquid water condensation in the GDL and electrode
- Investigate the effect of liquid water condensation on oxygen transport..
- Investigate the effect of coupled heat and water transport on water condensation behavior.
- Understand the performance losses that originate due to liquid water condensation inside the catalyst layer.
- Investigate down-the-channel distribution of species and current density under realistic PEMFC operating conditions such as: low stoichiometry, counter-flow, high pressure and coolant temperature gradient.

In order to achieve the targets, at first a 1-D modeling framework is developed which can account the critical physics for simulating PEMFC transport under dry operating conditions. Then two-phase water transport in the GDL and electrode is added to the 1-D model to simulate the effect of water condensation on PEMFC performance. Finally the two-phase 1-D model is expanded to a down-the-channel model to investigate distribution of current and gas components in along the channel direction at realistic automotive operating condition with low stoichiometry and counter-flow.

1.6 Thesis outline

In the current chapter, an overview of PEMFC operating principle, components and current technical challenges has been presented, followed by the objectives of this thesis research. In chapter 2 a comprehensive literature review of the PEMFC models with gas phase and liquid phase transport along with down-the-channel distribution is presented. In chapter 3 the materials used for fuel cell and the experiment protocol for limiting current and polarization test is discussed. In chapter 4, the framework of the 1-D model is presented and model results under dry operating condition is discussed in detail. In chapter 5, a novel technique to model the effects of liquid water condensation in the GDL and catalyst layer is presented followed by experimental validations. In chapter 6, the two-phase 1-D model is expanded to a down-the-channel model to investigate transport in realistic operating conditions with low stoichiometry and counter-flow. Finally in chapter 9, the summary of the thesis research and future research scopes are provided.

Chapter 2

LITERATURE REVIEW

Over the last decade significant progress has been made in cost reduction and performance improvement of PEMFCs. Major auto manufacturers have introduced commercial fuel cell powered electric vehicles for consumer purchase [157, 97, 54]. In this rapid development of PEMFC technologies, both experimental research and continuum scale modeling have made important contributions. Modeling, both computational and analytical has enabled the researchers to gain insights into the complex phenomena that are not possible to explain with experiments. Fuel cell modeling started getting interests from researchers in early 1990s. More than hundreds of PEMFC models have been published since then. Early PEMFC models were mostly analytical and considered gas phase transport only but after the computing capabilities increased, much of the focus shifted towards computational modeling from early 2000. Computational models, based on finite volume and finite element method, can calculate complicated 3D transport and electrochemical phenomena occurring inside the cell. These 3D results provide valuable local distribution information, which are difficult to measure physically. However, the 3D computational models are extremely computational demanding, and the results are highly sensitive to boundaries across the multi-physics, like heat transfer, fluid flow, electrochemistry, and phase change. These drawbacks make 3D computational modeling very challenging and often less desirable for quick cell diagnosis. In contrast, developing an analytical model based on fundamental physics is less computational demanding and can help understand the fundamental physics easier. A well-constructed 1-D analytical model can be used as a tool for cell diagnostics and material optimization. However, Analytical models have its limitations too. Complex physical phenomena that occurs during PEMFC operation are very difficult to solve analytically with accuracy at high spatial resolution (2D, 3D). So analytical models are mostly restricted to 0D, 1D or pseudo 2D (1+1D) scales. But even with these limitations,

a well-constructed analytical model can be extremely useful. Empirical models are simple and efficient in predicting the performance of a typical PEM fuel cell however, these models are unable to capture the transport processes in the fuel cell. To capture the details of the transport processes, it is required to develop a detailed mathematical model of PEM fuel cell and its numerical simulation.

2.1 PEMFC models with gas phase transport

Early PEMFC models found in literature mostly considered gas phase transport. The models by Springer et. al [130], Bernardi [14] and Verbrugge [13] laid the PEMFC modeling foundation for the further advancement of mathematical modeling in this field. Both Springer and Bernardi-Verbrugge considered a 1D sandwich consisting of MEA and diffusion media. While Bernardi and Verbrugge assumed a fully hydrated membrane, Springer et al. solved membrane water transport with varying water content. Springer’s model discussed importance hydrating the Nafion membrane for lower ohmic losses. However, both these models assumed isothermal temperature distribution in the 1D sandwich. Later, Bernardi [13] also developed a simple 1D model to emphasis the effect of water balance in PEMFC operation under different temperature, pressure and relative humidity ranges. But he considered fully humidified membrane in this model as well. X. Li et al. [96, 95] added a isothermal electrochemical PEMFC model to the water transport model of Bernardi and Verbrugge to study various operating and design parameters on cell performance. Following Springers modeling approach, Nguyen and White [105] developed a pseudo 2D down the channel model and discussed variation of reactant gas and water in down the channel direction. This model was non-isothermal but considered membrane water balance. They showed the importance of the coupling heat and water balance equations. However, for simplicity, they assumed a linear profile for water concentration in the membrane which does not represent the accurate physics for membrane water profile.

Besides these two approaches, Fuller and Newman [40] applied the concentrated solution theory in membrane to formulate a 1-D model which was an advancement from Springer’s approach and they were one of the first to include non-isothermal effects in a down the channel model. Later Amphlett et al. [5, 6, 94] developed empirical models specifically for Ballard Mark IV cells and stacks using a

constant water flux condition. W.Gu et al formulated a down-the-channel or pseudo 2D model including membrane water transport [47]. Kulikovsky [72, 76, 75, 77, 73, 74] also developed several analytical and semi analytical model focusing on non-isothermal effects along the channel and showed that the cell can operate in three limiting current regions due to oxygen limiting, water limiting and mixed regime. Shamardina et al. [126] developed a 1-D isothermal model for a high temperature PEMFC that can account gas cross over through the membrane. J.X Liu et al [89] developed an isothermal 1-D model that includes the full cell geometry, but they assumed a constant membrane conductivity. Among other pseudo 1-D models, Lin [30] assumed a linear water content in membrane and Tsai [137] [31] and Chevalier [27] used a constant membrane conductivity and Vijayaraghavan [141] formulated a transient model to predict the voltage response the cell.

A.Z. Weber developed [152, 149] a 1D physical and analytical model for two phase water transport in a Nafion membrane applying the concentrated solution theory. Later they added a fuel cell electrochemical model [151] [36] and microporous layer [150] to study the effects of flooding on PEMFC performance. They also included coupled heat transfer and water transport model [150] to their previous models and showed the importance of non-isothermal effects on water management. However, they applied numerical techniques to solve the governing equations of the model. Researchers have also developed analytical models which focuses only the cathode side of the cell. For example, Neyerlin et al. [103, 102, 136] modeled only the catalyst layers and studied the effects of RH on oxygen reduction kinetics. They also obtained the current density distribution anode and cathode catalyst layer. Gurau et al. [48] also developed an isothermal half-cell analytical model for the cathode side. He discretized the gas diffusion media to obtain liquid water concentration variation in the diffusion media. However, this model also did not include the membrane water balance. Abdin et al [1] developed a MATLAB Simulink based isothermal 1D analytical model. Falcao et al. [36] also developed a 1D analytical model for PEMFC performance considering heat transfer, membrane water balance. They used an iterative approach for water transport across the membrane. Later they added two phase transport phenomena to their model [38] There are several other notable isothermal models. Too name a few - Eikerling [34], Okada [107], Sena [125], Baschuk [10] , Maggio [92], Das [30, 29], Haji [50], Salva et al. [124], Liso [85],

Chavan [26], Raman [121], Rahimian [119], Hosseinzadeh [55].

2.2 PEMFC models with liquid water transport

While single phase PEMFC models are good at explaining the physics at dry operating conditions, they fail to account for the mass transport loss that originate due to cell flooding under fully humidified operating conditions. Two-phase flow modeling of PEMFCs are very challenging and still not very well-understood. There have been several approaches to model two phase water transport using both macroscopic and microscopic approaches. Two phase macroscopic models are based on volume averaged method and the governing equations for water transport are solved using CFD techniques. Macroscopic models can be coupled to a full PEMFC performance model, but they are computationally very expensive and require accurate measurement of the liquid water transport properties which is often very difficult to obtain. In recent years, microscopic approaches based on Lattice Boltzmann Method (LBM) has been applied on detailed morphological geometric domain of GDL. Another computationally efficient approach is the pore-network approach where the GDL is modeled using regular network of cubic pore and throats. While these approaches do provide useful information on liquid water transport through the porous network, they cannot be coupled to a full geometry electrochemistry model of a PEM fuel cell. For performance optimization and diagnostics, a simple computationally effective PEMFC performance model is necessary.

Djilali et al [16, 15, 129] developed multfluid model where they considered air as a multicomponent mixture and liquid phase as immiscible water. Each phase is modeled with separate governing equations. With this model they observed non-uniform distribution of temperature and pressure has a large impact on PEMFC performance. Hwang [60, 59, 58] and Zhou [161] also developed two-phase PEMFC models based on a similar approach. Wang et al [144, 139, 140] developed multfluid mixture (M2) model where they described the water transport as a mixture of vapor and liquid with traditional mixture averaged technique. This approach has been adopted by Sun et al. [132], He et al [52, 57] and Lou et al [158] in their two-phase PEMFC models too. Nguyen et al [53, 84, 104, 101] developed a two phase flow model based on unsaturated flow theory (UFT). UFT only requires one additional equation for water transport and considers only driving force for liquid

water transport is capillary pressure. Pasaogullari et al. [116, 115, 114] developed a two-phase PEMFC model to simulate liquid water transport model inside the GDL and MPL using a capillary pressure and saturation function. They provided physical insights into the effect of micro-porous layer using the two-phase flow model. Weber et al [150, 152, 149, 150] also developed a PEMFC model to simulate the effects diffusion media wettability on PEMFC performance. They developed an analytic expression which accounts the diffusion media pore size distribution and saturation behavior. There are numerous other two phase models published in literature [29, 2, 49, 155, 93, 31, 32, 38, 118, 66, 37, 90]. Detailed review on transport modeling in PEMFCs has been done by Weber et al. [148], Wang et al. [142].

While these rigorous computational modeling approaches are useful in resolving 3-D distribution and motion of liquid water, they are computationally very expensive, often numerically unstable at high saturation levels and lack experimental validations. As a result, the complex models are not preferable as a diagnostic or material optimization tool. In addition, almost all of the PEMFC two phase models use the generalized form of Darcy equation to model liquid water transport in fuel cell porous media.

$$\mathbf{u} = -\frac{\kappa_R(s)\kappa}{\mu}\nabla p_c(s) = -\frac{\kappa_R(s)k}{\mu}\frac{\partial p_c}{\partial s}\nabla s \quad (2.1)$$

Where, \mathbf{u} is liquid water velocity (m/s), p_c is capillary pressure (Pa), κ_R is relative permeability ($1/m$), s is liquid water saturation and μ refers to water viscosity ($Pa-s$). However, the material properties for Darcy law are very difficult to measure experimentally since they depend on the local saturation level. For capillary pressure and liquid saturation correlation, Leverett's polynomial fit is the most widely used which was derived based on the water transport in sand [83, 138]. Leverett's approach assumes a uniform wettability while ignoring hysteresis and consistently over-predicts diffusion media saturation levels [80]. Gostick [43], Mench and Kumbar [79, 80, 81] reported the relationship for capillary pressure and saturation for some commonly used GDL that can be used to calculate liquid water saturation in PEMFC diffusion media [127]. Still the relative permeability measurement remains a challenge due to uncertainty in small pressure differences across sample. Further

more, liquid water transport in the GDL is dominated more by the water condensation inside the pores than just liquid water permeation. Local source terms due to water condensation are greatly dependent on the thermodynamic rate constants that are extremely difficult to measure from a direct experiment. Lastly, the application of zero saturation boundary condition at the flow channel-GDL interface to solve Darcy law is not realistic. Most of the models set the saturation boundary condition at zero which is not realistic. Due to these issues, it difficult to model accurate oxygen transport resistance in the GDL using Darcy law.

Benziger et al.[12] showed that for liquid water removal only a small portion of void fraction of the GDL are required. Rest of the smaller pores remain free for gas diffusion between the flow channel and electrode. In addition, liquid water formed at the electrode needs to build up enough pressure to penetrate the largest pores of the GDL. Once water penetrates the pores, liquid water can be freely transported with a very small pressure gradient. Lister et al. [87] investigated the dynamic behavior and distribution of liquid water transport through GDL using fluorescent microscopy. They also found that transport of liquid water is a process of pressure buildup and break through. Using this technique, they showed water forms finger like tendrils through the GDL and droplets grow out of the GDL to flow channel. The observation agrees with wet limiting current measurement of Toray gas diffusion media materials by Caulk[21, 22] and Chuang et al [28]. Currently none of the two-phase fuel cell models can simulate the oxygen transport resistance under wet operating conditions.

2.3 Down-the-channel distribution models

The 1+1-D approach was first adopted by Fuller and Newman [40] and Nguyen [105] to study the gas composition and membrane hydration in along-the-channel direction. Since then, the pseudo 2-D or 1+1-D approach has been adopted by studies to investigate species or current density distribution in the channel direction. Kulikovsky et. al. developed 1+1-D analytical model to investigate the effect of oxygen stoichiometry on cell performance [78]. Based on the semi-analytical model he observed the PEMFC may operate in oxygen limiting or water limiting (low membrane hydration) current or mixed regime [76]. However, only dry operating conditions with co-flow operation was investigated. In a similar approach,

Chevalier et. al. also developed a analytical down-the-channel model to study reactant distribution in along the channel direction [27]. While these analytical models are extremely simplistic they are primarily focused on a very few transport phenomena and boundary conditions. The complex Multiphysics interactions are not captured in the analytical 1+1-D models. Jung S. Yi et. al. developed a 1+1-D single phase model to study the effect of flow orientation but these numerical studies were conducted at high stoichiometric ratios [64]. Yi et. al. also studied water distribution in the down-the-channel direction with co-flow performance [156]. Um et. al. developed a 1+1-D model based on CFD approach to investigate current and reactant distribution [139] but with co-flow orientation only. Wang et. al. developed a down-the-channel two-phase model using the multifluid mixture model to investigate water saturation distribution and observed for co-flow operation high water saturation is present near the cathode exit. Siegel et. al. developed a 1+1-D model but focused only on find the optimal catalyst layer void fraction. Weber et. al. investigated the effect of membrane and catalyst layer thickness using a down-the-channel model with co-flow and high stoichiometric flow rates and observed that membrane thickness caused large deviations in water management under dry conditions [146]. Pant et. al. in a new approach formulated a 1+2-D model considering full 2-D geometry with land and channel. They observed high flow-rates are optimal for wet inlet conditions and low flow-rates for dry inlet conditions [110]. However, only co-flow orientation was considered for these studies. Gu et. al. developed the most comprehensive 1+1-D model where the current density distribution is validated with experimental measurements [46]. They also illustrated water can be internally recirculated inside the cell when counter-flow orientation is used.

2.4 Summary

From the aforementioned, literature review it can be observed that there is a clear gap in literature in both 1-D and 1+1-D models. For example, the 1-D models that consider gas phase transport only validate their results with dry polarization curves but do not extend their simulations to the limiting current region. So, it is difficult to determine how effective these models are in capturing the oxygen transport resistances. From the literature review it is also evident that, even

though there are numerous models available, most of them ignore important physical phenomena like heat transfer and membrane water balance. Even the models that include thermal effects, often do not consider the thermal contact resistances. Besides these, a few other important factors to consider while constructing a 1-D model are electronic contact resistance, shorting and cross over current, and inclusion of land-channel geometric effect to account for increased diffusion path. Similar observations are also found in 1-D models that considers liquid water transport. The numerous two-phase PEMFC models in the literature only validate with wet polarization performance and none show how effective these models are in predicting the non-linear oxygen transport resistance under the wet operating condition. In addition Darcy law based capillary pressure driven approach is taken to formulate two phase transport inside the GDL and to solve the water transport equations inaccurate boundary conditions (zero saturation at flow-channel-GDL interface) are applied. More importantly, most of the models utilize the Leverette's correlation for saturation and capillary pressure which was developed for water transport in sands. The 1+1-D models available in literature only investigate the cell performance and channel distributions at co-flow orientation and often at relatively high stoichiometric flow rates. However, the channel distribution becomes extremely complex at low stoichiometry and counter-flow operations. To this date the effect of low stoichiometry and flow-orientation on overall water balance and cell performance have not been comprehensively studied.

In this thesis research a 1+1-D PEMFC model has been developed which aims at addressing the current gap in literature. A 1-D steady state modeling framework is developed at first which can be to simulate PEMFC performance under dry operating condition. The fundamental physics including membrane water balance, non-isothermal heat transfer, mass transport with geometric effect, shorting and hydrogen cross over current have been carefully included in the 1-D model. Next, the two-phase water transport in the gas diffusion media and in electrode has been added to the 1-D model. The electrode water transport model is developed in a empirical approach where catalyst utilization is correlated predicted electrode water activity based on experimental data to investigate the reduction of catalyst at high water saturation conditions. Results from the developed 1-D steady state,

two-phase PEMFC model has been validated limiting current and polarization experiments under both dry and wet operating conditions. Even with these interactive physics, the constructed 1-D model retains the simplicity of mathematical iteration. Therefore, the model can be easily used as a design and diagnostic tool. Finally the 1-D two-phase model is expanded to a 1+1-D down-the-channel framework to study the effects of flow-orientation and low stoichiometry on along the channel distribution of gas species and the corresponding cell performance.

Chapter 3

EXPERIMENTS

3.1 Materials

For the fuel cell experiments, the cell was built with parallel flow channel flow fields with active area of 2 cm^2 . The flow field contained total 17 channels, and each channel had width of 0.61 mm, height of 0.80mm, and rib width of 0.61 mm. The membrane electrode assembly used in this experiment was Nafion 211 membrane of 25 micron thickness with $0.3\text{ mg}_{Pt}/\text{cm}^2$ catalyst loading purchased from Ion Power, USA. Wetproofed Toray 060 with microporous layer was used in both anode and cathode for this experiment. To seal in reactant gases within the active area, PTFE gaskets were used. The thickness of the gaskets was chosen to ensure adequate compression throughout the active area. Other cell hardware consisted of end plates and current collectors. The material for the end plate was aluminum alloy with a cross-section of $108\text{ mm} \times 108\text{ mm}$ and a thickness of 19.15 mm. The collector plates were made of highly conductive gold-plated copper to increase their surface conductivity and reduce contact resistance to flow field plates.

A G20 Greenlight Innovation fuel cell test station was used to evaluate the performance of the cells. The test stand was used to control and monitor the electronic load, flow rate, temperature, humidity, and back pressure through control and data logging software (HyWare®). All gases used were 99.99% purity. For the measurement and control of pressure, Wika-10 pressure transmitters were used. The test station controlled relative humidity by passing gas streams through temperature-controlled bubbler humidifiers and inlet tubing. The cell temperature was measured by thermocouples inserted within the flow field plates. Heating and cooling were controlled through heating cartridges inserted into the end plate and fans placed on each side of the cell. All the tests were run with constant flow control.

3.2 Fuel cell tests

Single cell 2 cm² tests were performed on an automated G20 fuel cell test station manufactured by Greenlight Innovation [4]. High frequency resistances were measured using a Gamry Reference 3000 with 30k booster [42]. Polarization curves at 70 °C under both wet (100% RH and 300 kPa) and dry (60% RH and 100 kPa) conditions were tested with constant flow rates of 0.4 slpm of pure hydrogen and 2.0 slpm of air to evaluate fuel cell performance. In addition, limiting current experiments under different pressure and oxygen mole fraction were conducted to study dry and wet oxygen transport properties in the GDL. Detailed operating conditions of break-in, polarization, and limiting current are listed in Table 3.1.

Protocol	Temp.	Inlet RH	Pressure	Flow Rate (An/Ca)	Load Control	Step hold time
	(C)	(%)	(kPa)	($\times 10^{-6} m^3 s^{-1}$)	(V)	(sec)
Break-in	80	100	50	10/10 (Stoich)	OCV-0.6	900
Wet Polarization	80	100	300	6.64/33.2	OCV-0.3	600
Dry Polarization	80	64	100	6.64/33.2	OCV-0.3	600
Dry Limiting Current	80	64	300, 200, 150, 100	6.64/33.2	0.3-0.09	130
Wet Limiting Current	70	90	300	6.64/33.2	0.3-0.09	130

Table 3.1: Single cell 2 cm² testing protocol.

The limiting current method is an in-situ experimental technique to quantify oxygen-transport resistance in a fuel cell. Following the protocol developed by Baker et al. [7], we conducted limiting current tests under both dry and wet conditions to study the oxygen transport properties in both Toray and Freudenberg GDL materials. To ensure uniform conditions in the cell, a low pressure drop flow channel design with high stoichiometric flow was applied. During fuel cell operation at a current density of, “ i ” ($A cm^{-2}$), the through-plane oxygen molar flux, N''_{O_2} ($mol cm^{-2} s^{-1}$) can be expressed by total oxygen transport resistance $R_{O_2}^{Total}$ ($s cm^{-1}$) as follows:

$$N''_{O_2} = \frac{i}{4F} = \frac{\Delta P_{O_2}}{(RT) \times R_{O_2}^{Total}} \quad (3.1)$$

where ΔP_{O_2} (kPa) is the gradient of oxygen partial pressure between the flow channel and the CL, R is the universal gas constant, F is the Faraday constant and T

(K) is the cell temperature. Under limiting current conditions, the oxygen partial pressure at the CL approaches zero. Therefore, the oxygen partial pressure gradient in Equation 3.1 is equal to the oxygen partial pressure in the flow channel. Since the cell is operating under uniform condition, the channel oxygen partial pressure is controlled by the dry mole fraction of oxygen, $x_{O_2}^{dry}$, and can be written as:

$$P_{O_2}^{channel} = x_{O_2}^{dry} (P_{total} - P_{sat} \times RH) \quad (3.2)$$

where P_{total} is the total absolute pressure in the channel, P_{H_2O} is the water vapor pressure in the channel, and RH is the relative humidity in the channel. From Equations 3.1 and 3.2, the total oxygen transport resistance can be obtained by:

$$R_{O_2}^{Total} = \frac{4F}{i_{lim}} \left[\frac{x_{O_2}^{dry} (P_{total} - P_{sat} \times RH)}{RT} \right] \quad (3.3)$$

The total oxygen transport resistance in a fuel cell is composed of resistances from each component including the channel, $R_{O_2}^{Ch}$, the gas diffusion layer, $R_{O_2}^{GDL}$, the micro-porous layer, $R_{O_2}^{MPL}$ and the catalyst layer, $R_{O_2}^{CL}$, and can be expressed as:

$$R_{O_2}^{Total} = R_{O_2}^{Ch} + R_{O_2}^{GDL} + R_{O_2}^{MPL} + R_{O_2}^{CL} \quad (3.4)$$

Oxygen transport in the flow channel is driven by both convection and inter-molecular diffusion [120]. In the GDL, the inter-molecular diffusion, which is pressure dependent, is the dominating transport mechanism because of the large pore size ($> 50 \mu m$). In the MPL and CL, the Knudsen diffusion may become an important transport method in the small size pores ($< 100 nm$). In addition, oxygen gas can also diffuse through liquid water and ionomer films in the CL. Unlike inter-molecular diffusion, transport resistances resulted from both Knudsen and thin film diffusion are independent of pressure. Based on the transport mechanism, we can separate oxygen transport resistance into pressure dependent, (R_P), and pressure independent, R_{NP} , as:

$$R_{O_2}^{Total} = R_P + R_{NP} \quad (3.5)$$

In limiting current tests, we performed the experiments at four different pressure

conditions to quantify pressure-dependent and pressure-independent resistances under dry conditions [7].

Chapter 4

DEVELOPMENT OF 1-D MODEL

The 1-D model is developed in a galvanostatic approach where cell voltage is calculated based on the input applied current density. The voltage losses in PEMFC operation are a strong function of current density and final cell voltage obtained by subtracting all the voltage losses from the reversible cell voltage.

$$V = E_{rev} - \eta_{HOR} - \eta_{ORR} - \eta_{ohmic} - \eta_{mass} \quad (4.1)$$

Here η_{HOR} and η_{ORR} refers to the voltage loss due to HOR and ORR kinetics, η_{ohmic} is the voltage loss due to electron transport and proton transport in the membrane and porous electrodes and η_{mass} is the mass transport loss due to reactant depletion in the electrode.

4.1 Modeling domain

The modeling domain includes the anode catalyst layer (aCL), cathode catalyst layer (cCL), membrane (Mem), anode and cathode microporous layers (aMPL, cMPL), anode and cathode gas diffusion layers (aGDL and cGDL), and the flow channels. A schematic diagram of the modeling domain is shown in Figure 1. From here on, the term diffusion media refers to the GDL and MPL domains combined. Fully developed flow is assumed in the flow channels and a constant reactant concentration in the flow channel is used as a boundary condition for the mass transport equations. Pressure in the modeling domain is considered as isobaric. For mass transport in the gas diffusion layer and microporous layer, diffusion is considered as the only transport mechanism. Both Fickian and Non-Fickian diffusion is included in transport resistance but the pressure independent Non-Fickian diffusion terms like Knudsen diffusion are lumped into a constant resistance parameter term in the transport equations, R_{others} , which is obtained experimentally. Anisotropic

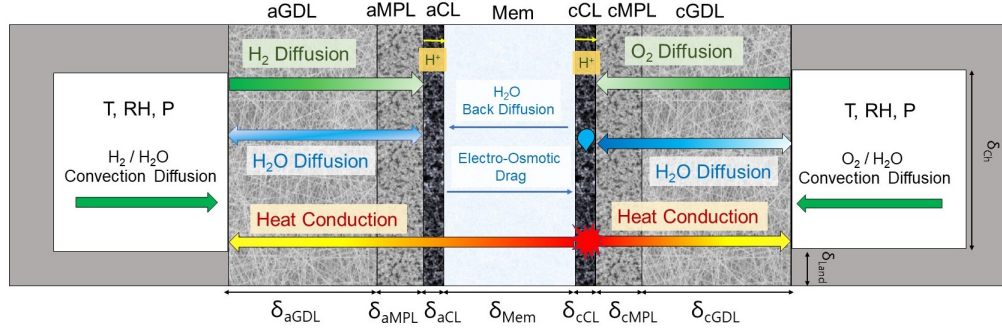


Figure 4.1: Modeling domain for the 1-D PEMFC model and through plane transport processes

diffusion in the gas diffusion media is modeled with a correction factor f_{geo} . Homogeneous and isotropic properties for porosity, tortuosity and thermal conductivity are assumed throughout the spatial domain. The developed model is a single-phase model that assumes water to be present in vapor phase only. The main objective of the developed modeling framework in this chapter is to accurately predict the dry polarization performance.

4.2 Reversible cell voltage

The temperature and pressure dependent reversible cell voltage of equation 4.1 is be calculated from the Nernst equation [106].

$$E_{rev} = \frac{\Delta g}{2F} + \frac{\Delta s}{2F}(T - T_0) - \frac{RT}{2F} \ln \left(\frac{1}{\frac{P_{H_2}}{P_{ref}} \times \left(\frac{P_{O_2}}{P_{ref}} \right)^{1/2}} \right) \quad (4.2)$$

Here $\Delta g = \Delta h - T\Delta s$ is the Gibb's free energy of the reaction that can be calculated from the reaction enthalpies which are provided in table 1. F is Faraday's constant, P_{O_2} and P_{H_2} are the oxygen and hydrogen partial pressure at the channel and $P_{ref} = 1$ atm is the reference atmospheric pressure.

4.3 Hydrogen oxidation reaction (HOR)

In PEMFCs hydrogen oxidation reaction kinetics is several orders of magnitude faster than the ORR kinetics and very low Pt is needed to facilitate the

HOR reaction. Due to the simplicity of HOR reaction it can be modeled using the Butler-Volmer equation as:

$$i = i_{0a} \left[\left(\frac{P_{H_2, ch}}{P_{ref}} \frac{T_0}{T} \right) \exp \left(\frac{2\alpha F \eta_{HOR}}{RT} \right) - \exp \left(\frac{-2\alpha F \eta_{HOR}}{RT} \right) \right] \quad (4.3)$$

Here the exchange current density can be obtained as $i_{0a} = i_{0a}^0 \times rf \times \exp\left(\frac{-\Delta G_{HOR}}{R}\left(\frac{1}{T} - \frac{1}{T_0}\right)\right)$, α is the reaction symmetry coefficient, η_{HOR} is the activation overpotential for HOR reaction, R is the universal gas constant, T is the temperature, P_{H_2} is the partial pressure of hydrogen in channel. The exchange current density for both HOR and ORR is multiplied by roughness factor. The roughness factor, rf , is the product of platinum loading and the electrochemically active surface area ($ECSA$), which is obtained experimentally by cyclic voltammetry. Kinetic parameters used in this model are provided in Table 1.

4.4 Oxygen reduction reaction (ORR)

The oxygen reduction reaction is significantly a more complex reaction compared to the HOR and ORR kinetics cannot be explained completely by the simple butler-volmer equation specially when low Pt loading is used or at high current densities. Experimental studies have shown that at low Pt loading the tafel slope ($b=2.303 RT/\alpha F$) significantly deviates due to surface oxies. To capture the effects of surface oxides, a Pt-oxide coverage dependent ORR kinetic model developed by subramaniam et. al. [131] has been implemented

$$i = i_{oc} \times (1 - \theta_w) rf \times \left(\frac{P_{O_2}}{P_{O_2, ref}} \right)^m (1 - \theta_{PtO_x}) \exp \left(\frac{-\alpha F \eta}{RT} \right) \exp \left(\frac{-\omega \theta_{PtO_x}}{RT} \right) \quad (4.4)$$

where $i_{oc} = i_{oc}^0 \times rf \times \exp\left(\frac{-\Delta G_{ORR}}{R}\left(\frac{1}{T} - \frac{1}{T_0}\right)\right)$, i_{oc}^0 is the exchange current density (A/cm_{pt}^2) ORR reactions, α is the reaction transfer coefficient, θ_{PtO_x} is the oxide coverage, R is the universal gas constant, and η is the ORR activation loss. Exchange current density, i_{oc} is obtained by fitting the kinetic data of dry polarization performance. The Pt-oxide coverage is calculated from the experimentally measured

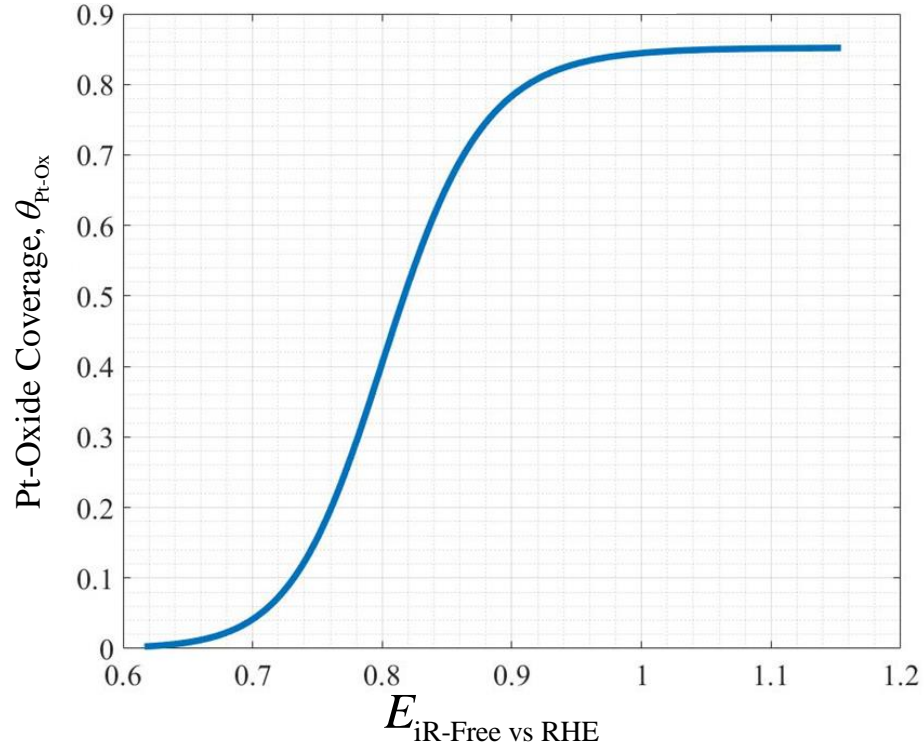


Figure 4.2: Experimentally measured Pt-oxide coverage by subramanium et. al. [131]

θ_{PtO_x} vs E-iR free voltage as shown in figure 4.2. Generally a constant Tafel slope of 70mV is assumed for ORR kinetics. The predicted Tafel slope from the ORR kinetic model is plotted in figure 4.3. It can be observed that oxide coverage dependent ORR kinetic model predicts the doubling of the Tafel slope at low iR free cell voltages (high current densities).

4.5 Charge transport

Fuel cell operation involves two types of charged species: electrons and protons (ions) and both of the charged species need to be transported in order to complete the electrochemical reactions and generate electricity. The transport mechanism for electrons and protons are very different with proton transport being the more complex and difficult one. The charge conductors for electrons and protons are also very different and none of the conductors have a infinite conductivity. The resistance to charge transport process results in a voltage loss and the voltage loss

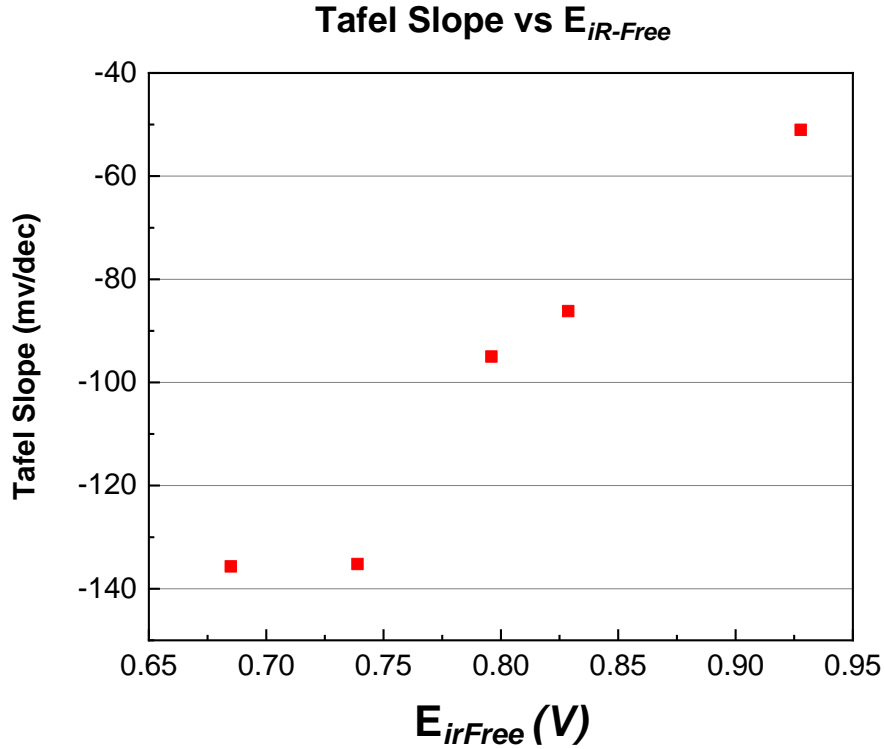


Figure 4.3: Tafel slope determined from the Pt-Oxide coverage dependent ORR kinetics model

follows Ohm’s law. In this thesis the voltage associated with electron and proton transport is referred as the “Ohmic loss”. The main focus of this section will be on modeling proton transport mechanisms in membrane and in fuel cell electrodes since it is the major source of ohmic loss in PEMFCs.

4.5.1 Proton transport in membrane

In a PEMFC protons are generated in the aCL from the HOR reaction and the generated protons are transported to the cCL by the proton conducting membrane (electrolyte). PEMFC membrane is a polymer made a copolymer of tetrafluoroethylene (TFE) and various perfluorocarbon-sulfonic-acid (PFSA) monomers [82]. The fuel cell membrane must exhibit high proton conductivity in order to reduce the ohmic loss from proton transport and the commercial membrane Nafion produced by DuPont is the most commonly used membrane for PEMFC applications for its extremely high proton conductivity. In this thesis the proton transport mechanisms

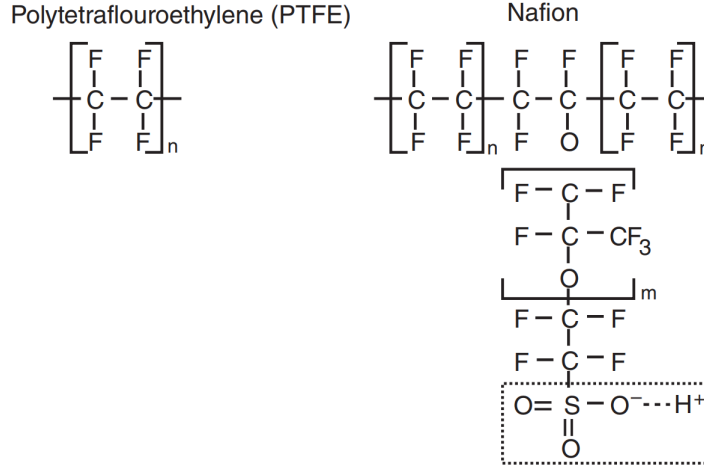


Figure 4.4: Chemical structure of Nafion membrane showing the PTFE backbone for mechanical stability and sulfonic acid groups for proton conduction. (Image source: O’Hayre et. al. [106])

and the critical transport properties discussed are for Nafion membranes. Figure 4.4 shows the chemical structure of Nafion. It can be observed that Nafion includes PTFE backbones that provide mechanical stability of the membrane and also includes sulfonic acid functional chains that provide charge sites for the vehicular proton transport mechanism. Proton conductivity of Nafion membrane is strongly correlated with water absorption of the membrane (a phenomenon also known as water uptake) and the membrane temperature. Springer et. al. measured the conductivity of Nafion membrane [130] as:

$$\sigma_{303K(\lambda)} = 0.005193\lambda - 0.00326 \quad (4.5)$$

$$\sigma(T, \lambda) = \sigma_{303K(\lambda)} \exp \left[1268 \left(\frac{1}{303} - \frac{1}{T} \right) \right] \quad (4.6)$$

Where σ is the membrane conductivity (S/cm), λ is the water uptake and T is the membrane temperature. The relationship between water conductivity, temperature and membrane conductivity is shown in figure 4.5 and 4.6. It can be observed that conductivity of the Nafion membrane is linearly correlated with water content λ and exponentially correlated with the membrane temperature T .

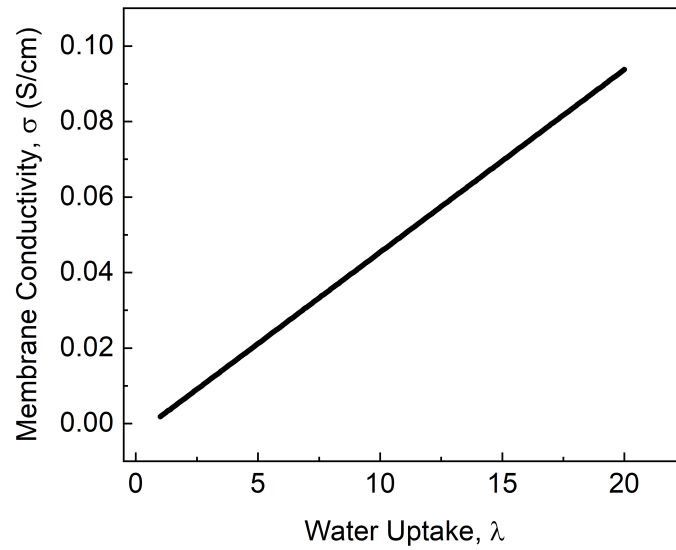


Figure 4.5: Conductivity of Nafion vs water uptake based on the experimental measurements by Springer et. al. [130]

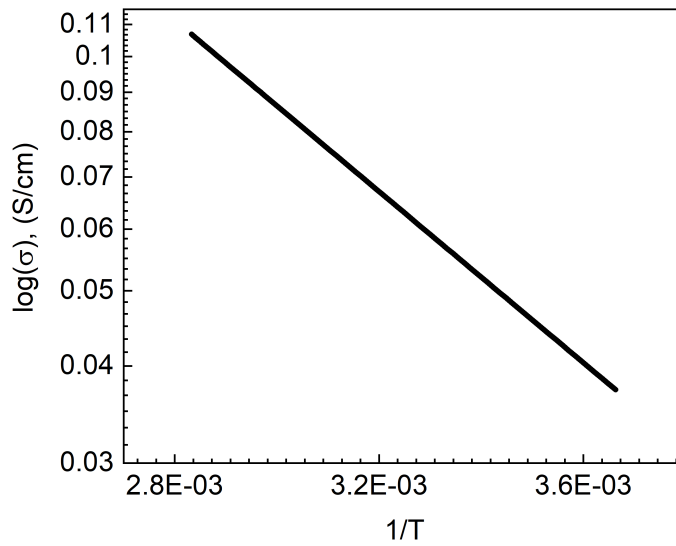


Figure 4.6: Conductivity of Nafion vs temperature showing exponential correlation

4.5.1.1 Water uptake

Because of the chemical structure of Nafion, PEMFC membranes contain high amount of water. The water content in membrane is also referred as membrane water uptake and it is usually expressed as the number of water molecules per sulfonic acid groups present in the polymer. Under completely dry condition (completely dehydrated membrane) water uptake value is 0 and for fully saturated membrane with liquid water, the water uptake value of 22 has been measured experimentally. Generally water uptake is correlated with water activity levels in the membrane. Zawodzinski et. al. [160] measured the water uptake values of Nafion membrane as:

$$\lambda = \begin{cases} 0.0043 + 17.81a_w - 39.85a_w^2 + 36.0a_w^3 & \text{for } 0 \leq a_w \leq 1 \\ 14 + 1.4(a_w - 1) & \text{for } a_w > 1 \end{cases} \quad (4.7)$$

Here a_w is the water activity in the membrane calculated as $a_w = P_{H_2O}/P_{sat}$ where P_{H_2O} is the partial pressure of water vapor and P_{sat} is the saturation pressure. Figure 4.7 shows the highly non-linear distribution of water uptake (λ) with respect to water activity (a_w) based on equation 4.7. At low water activity levels water uptake becomes lower than 4 which results in very low conductivity. Membrane hydration is critical specially under dry operating condition as the performance losses due to proton transport can be very high.

4.5.1.2 Electro-osmotic drag

As protons move through Nafion membrane it drags water molecules in the form of hydronium ions which is known as electro-osmotic drag. The electro-osmotic drag coefficient is defined as the number of water molecules dragged by each proton ($n_{drag} = n_{H_2O}/H+$) and is a function of membrane hydration and current density. This coefficient is generally measured by nuclear magnetic resonance or electrochemical method and depending on experimental and data fitting technique the values of electro-osmotic drag coefficient may vary significantly. Zawodzinski et. al. reported a the drag coefficient varies linearly with water uptake levels [160]. The water flux due to electro-osmotic drag can be calculated as:

$$N''_{H_2O,drag} = n_{drag} \frac{i}{F} = \left(n_{drag}^{sat} \frac{\lambda}{22} \right) \times \frac{i}{F} \quad (4.8)$$

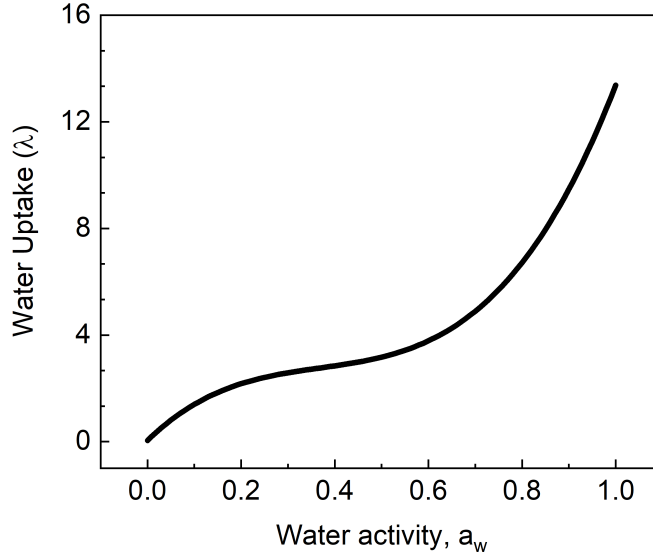


Figure 4.7: Membrane water uptake (λ) with respect to membrane water activity a_w

Where $N_{H_2O,drag}$ is the water flux due to electro-osmotic drag, n_{drag} is the electro-osmotic drag coefficient, n_{drag}^{sat} is the drag coefficient for fully hydrated membrane which has been reported as 2.5 by Zawodzinski et. al. [160]. A detailed discussion on the uncertainty associated with electro-osmotic drag values is discussed in section 5.3.5.

4.5.1.3 Water back-diffusion

During PEMFCs operation water is generated from the ORR reaction at cathode and in addition electro-osmotic drag transports water from anode to cathode. As a result water concentration in cathode generally becomes higher than anode if symmetric channel RH conditions are maintained. Because of this concentration gradient between cathode and anode water diffuses towards the anode side and this phenomenon is known as the water back diffusion. Back-diffusion counter balances the effects of electro-osmotic drag as it occurs in the opposite direction to

osmotic-drag. The water flux from back diffusion can be calculated as:

$$N_{H_2O,back-diffusion}'' = -\frac{\rho_{dry,mem}}{M_{mem}} D_\lambda \frac{d\lambda}{dz} \quad (4.9)$$

Where $\rho_{dry,mem}$ is the dry density of membrane, EW is the equivalent weight of membrane, D_λ is the water diffusivity coefficient through the membrane. Similar to the electro-osmotic drag coefficient, the water back diffusion co-efficient also varies widely in literature. For this 1-D framework the back-diffusion correlation measured by Springer et. al. [130] has been used (equation 4.10)

$$D_\lambda = \exp \left[2416 \left(\frac{1}{303} - \frac{1}{T} \right) \right] \times (2.563 - 0.33\lambda + 0.0264\lambda^2 - 0.000671\lambda^3) \times 10^{-6} \quad (4.10)$$

In equation 4.10 the exponential part shows the temperature dependence of the back-diffusivity and the polonomial part explains the dependence with water uptake.

4.5.2 Membrane water balance and membrane ohmic loss

Accurately modeling water uptake distribution inside the membrane is critical for simulating ohmic loss as membrane conductivity is a strong function of the water uptake. As water is transported across the membrane both back-diffusion and electro-osmotic drag, the coupling effects makes water transport inside the fuel cell a function of many factors including channel inlet relative humidity, flow stoichiometry, operating current density, operating pressure and temperature and material properties. Although the total water transport inside the cell can be measured experimentally, the quantification of water transport by each mechanism is nearly impossible. In this model, an iteration loop was used to determine water transport from the cathode to anode, f_w . The details of this water transport iteration are shown in Figure 4.14(a) of the supplementary material. The governing equation of water transport can be written as:

$$n_{H_2O}'' = -f_w \frac{i}{2F} = \frac{i}{F} n_{drag}^{sat} \frac{\lambda}{22} - \frac{\rho_{dry,mem}}{M_{mem}} D_\lambda \frac{d\lambda}{dz} \quad (4.11)$$

The first order ordinary differential equation of equation 4.11, can be solved to obtain membrane water content distribution, λ , throughout the membrane thickness.

The membrane water content boundary conditions are $\lambda = \lambda_a$ at the anode catalyst layer and membrane interface, and $\lambda = \lambda_c$ at the cathode catalyst layer and membrane interface. Since the water content distribution is non-linear, integrating the local resistance over the membrane thickness, δ , is used to obtain the area specific resistance ASR_{H^+} for proton transport through the membrane.

$$ASR_{H^+} = \int_0^{\delta} \frac{dz}{\sigma[\lambda(z)]} \quad (4.12)$$

The ohmic loss due to proton transport resistance in membrane can be calculated as:

$$\eta_{ohmic,mem} = i \times ASR_{H^+,mem} \quad (4.13)$$

4.5.3 Proton transport electrode

Once the protons move to the cathode electrode after crossing the membrane, they still need to reach the reaction sites in the electrode. Unlike the membrane, proton transport in the electrode is more difficult as the protons need to transport through the tortuous thin-film ionomers. The proton transport loss in electrode can be significantly high especially under dry operating conditions. The temperature and relative humidity (RH) dependent effective proton conduction in electrode can be obtained by multiplying the ionomer conductivity by the ratio of ionomer volume fraction to tortuosity.

$$\kappa_{eff(T,RH)} = \frac{\epsilon_i}{\tau(\epsilon_i)} \kappa(T,RH) \quad (4.14)$$

Here ϵ_i is the ionomer volume fraction, which can be obtained from the ionomer to carbon ratio in the electrode [91].

$$\epsilon_i = \left(\frac{I}{C}\right) \left(\frac{10}{f_t \rho_{dry,ionomer}}\right) \times \left(1 + \frac{M_w \rho_{dry,ionomer} \lambda}{\rho_{water} EW}\right) \quad (4.15)$$

where f_t is an empirically from [91]. $\left(\frac{I}{C}\right)$ is the ionomer to carbon weight ratio, M_w and ρ_{water} are the molar weight and density of water, respectively. EW is the equivalent weight of the ionomer. As noted from equation 4.15, the ionomer volume fraction in the electrode is a strong function of $\left(\frac{I}{C}\right)$ ratio. The tortuosity

Table 1. Geometric and Kinetic Parameters	
Geometric Parameters	
Channel hydraulic diameter, D_h	$723\mu m$
Sherwood number (S_H)	2.4
Gas diffusion layer thickness δ_{GDL}	$124.7\mu m$
Microporous layer thickness δ_{MPL}	$30\mu m$
Catalyst layer thickness δ_{CL}	$15\mu m$
Membrane thickness δ_{mem}	$25\mu m$
Thermodynamic Parameters	
Gibb's free energy, Δg [106]	$-237.13 (kJ/mol)$
Reaction Entropy, Δs [106]	$-163.46 (J/mol - K)$
Reaction Enthalpy, Δh [106]	$-285.83 (kJ/mol)$
Kinetic Parameters	
HOR activation energy, ΔG_{HOR}^{act} [47]	$1 \times 10^3 (kJ/mol)$
ORR activation energy, ΔG_{ORR}^{act} [47]	$50 \times 10^3 (kJ/mol)$
ORR reference exchange current density, i_{oc}^o , (<i>fitted</i>)	$5 \times 10^{-8} (A/cm_{pt}^2)$
HOR reference exchange current density, i_{oa}^o [47]	$1 \times 10^{-3} (A/cm_{pt}^2)$
HOR transfer coefficient, α_a	0.5
Tafel slope, $b = \frac{-2.303RT}{2\alpha_c F}$ [47]	$-70 (mV/decay)$
Pt loading	$0.3 (mg/cm^2)$
ECSA, (<i>measured</i>)	$39.33 (cm^2/mg_{pt})$
Shorting current, (<i>fitted</i>), i_{sh}	$3 (mA/cm^2)$
Cross over current, (<i>measured</i>), i_x	$2.19 (mA/cm^2)$
Faraday constant, F	96485

is dependent on the ionomer volume fraction and is obtained from reported in [91]. Thompson [136] derived an analytical solution for the proton conduction resistance based on linear approximation of HOR kinetics for the anode electrode.

$$R_{eff,anode}^{H^+} = \frac{1}{\kappa_{eff}s} \left(\frac{e^{s\delta_{anode}} + e^{-s\delta_{anode}}}{e^{s\delta_{anode}} - e^{-s\delta_{anode}}} - \frac{1}{s\delta_{anode}} \right) \quad (4.16)$$

where the s (cm^{-1}) is a kinetic parameter that reflects the relative magnitude of the ratio of the effective proton conduction resistance in the anode electrode over the charge transfer resistance.

$$s = \left[\frac{ECSA \times Pt_{loading} i_0}{\kappa_{eff} \delta_{anode}} \times \frac{(\alpha_a + \alpha_c) F}{RT} \right]^{1/2} \quad (4.17)$$

Table 2. Heat and mass transport parameters	
Material Thermal Properties	
Bipolar plate conductivity, K_{FF} [67]	$55 \times 10^{-2}(W/cm - K)$
GDL conductivity, K_{GDL} [67]	$1.71 \times 10^{-2}(W/cm - K)$
MPL conductivity, K_{MPL} [67]	$0.33 \times 10^{-2}(W/cm - K)$
CL conductivity, K_{CL} [67]	$0.27 \times 10^{-2}(W/cm - K)$
Membrane conductivity, K_{Mem} [67]	$0.12 \times 10^{-2}(W/cm - K)$
MPL-CL contact resistance R_{MPL-CL} [67]	$0.98(cm^2 - K/W)$
Flowfield-GDL contact resistance, R_{FF-GDL} [67]	$2(cm^2 - K/W)$
Mass Transport Properties	
Tortuosity/Porosity (τ/ϵ) of GDL, (<i>measured</i>)	5.05
Land/channel geometry factor, f_{geo}	1.54
Pressure independent transport resistance, R_{other} , (<i>measured</i>)	$0.1976(s/cm)$
Electron transport ASR_{e^-} , (<i>measured</i>)	$15(m\Omega - cm^2)$
Equivalent weight of membrane (Nafion 211)[47]	$1000g/mol$ of SO_3^- ion
Dry density of membrane [106], $\rho_{dry,mem}$	$2g/cm^3$
Electro-osmotic drag coefficient [130], n_{drag}^{sat}	2.5

Table 4.1: Parameters for 1-D simulation

The effective proton transport loss in the cathode electrode is obtained from the analytical solution derived by Neyerlin et al. [102].

$$R_{eff,cathode}^{H^+} = \frac{R_{sheet}}{3 + \zeta} \quad (4.18)$$

Here $R_{sheet} = \delta_{cathode}/\kappa_{eff(T,RH)}$ is the sheet resistance of the cathode electrode, ζ is a correlation factor which is a function of the ratio of iR_{sheet} and the Tafel slope b . While deriving the analytical solution, Neyerlin et al.[102] assumed a Tafel approximation to model the ORR kinetics. Since the Tafel approximation shows very good accuracy at high overpotential region, this analytical expression should be applicable to proton transport loss in the cathode electrode.

4.5.4 Electron transport

Electrons conduct through the carbon phase in the CL, MPL and GDL. The conductivity of electron is several orders of magnitude higher compared to proton conductivity. Primary sources of ohmic loss from electron transport comes from the contact resistances between different PEMFC layers. In this model, a constant

electronic resistance has been considered to model the ohmic loss from electron transport.

$$\eta_{ohmic,e^-} = i \times ASR_{e^-,mem} \quad (4.19)$$

4.5.5 Shorting and cross-over

As hydrogen is the smallest molecule in universe it permeates through the Nafion membrane even though Nafio is impermeable to reactant gases. The hydrogen molecule that permeates through the membrane reacts with oxygen on the cathode side and the generated electron does not travel through the external circuit. This current is known as "cross-over current". In addition, some electron may also reach the cathode from the anode resulting in "shorting current". The effect of shorting and cross-over current is not noticeable at high current densities as the hydrogen consumption or the electron generation rate is several orders of magnitude higher. However, at open circuit voltage (OCV) when the cell is operated at close to zero current densities, the losses associated with the internal currents become significant and as a result the OCV is lower than the reversible cell potential. In this model, shorting and cross-over current is considered in the total current term

$$i_{internal} = i_{shorting} + i_{cross-over} \quad (4.20)$$

$$i = i_{external} + i_{internal} \quad (4.21)$$

4.6 Mass transport

4.6.1 Mass transport in channel

In PEMFCs gases flow in along the channel direction from inlet to the exit of the channel. However, because of the concentration difference of the species between the electrode and the channel mass transport also occurs in the through-plane direction from channel to electrode. For example, the concentration of oxygen in the electrode is much lower than the concentration in the channel as a result oxygen is transported from the channel to the electrode via the gas diffusion media. The convective mass transport from channel can be expressed as:

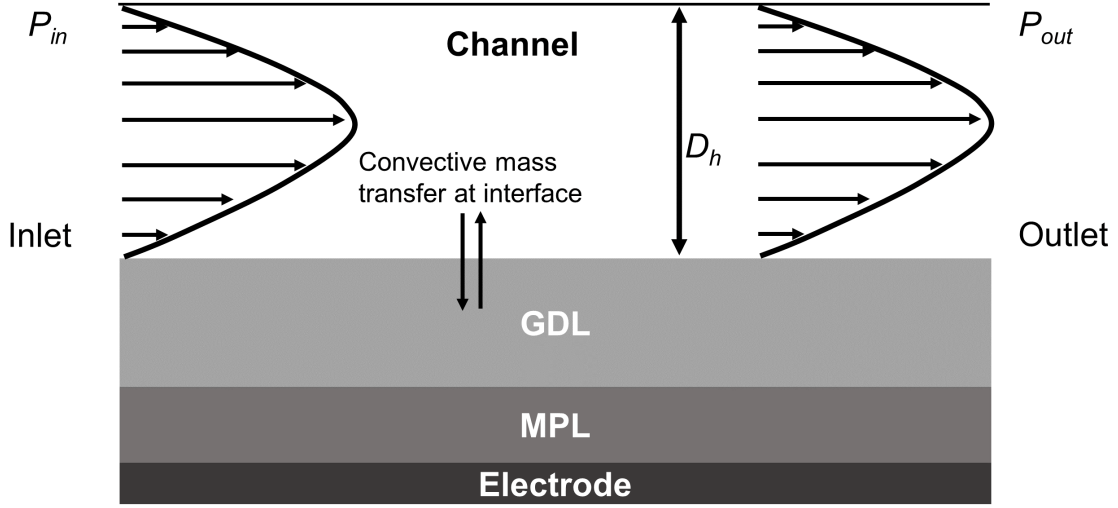


Figure 4.8: Schematic diagram of convective mass transport in PEMFC channels showing in-plane and through plane transport process.

$$N_i'' = h_m (C_i^{Ch} - C_i^{GDL}) \quad (4.22)$$

Where N_i'' is the molar flux of species i , ($i = O_2, H_2, H_2O$), C_i is the concentration of species i and h_m is the convective mass transfer coefficient. h_m is a function of channel geometry and diffusivity of species and it can be calculated from the non-dimensional Sherwood number as:

$$h_m = Sh \frac{D_{i,mix}}{D_h} \quad (4.23)$$

Where D_h refers to the hydraulic diameter of the channel and $D_{i,mix}$ is the mixture diffusivity of species i . Because of the micron scale channel geometry Reynold's number is generally much less than 2300. The Sherwood number for common channel cross section under laminar flow is provided in figure 4.9. Expressing equation 4.22 in resistance form we obtain

$$N_i'' = \frac{(C_i^{Ch} - C_i^{GDL})}{R_i^{CH}} \quad (4.24)$$

Where R_i^{CH} is the convective mass transport resistance of the channel calculated as:

$$R_i^{CH} = \frac{D_h}{Sh \times D_{i,mix}} \quad (4.25)$$


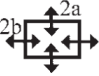

Cross Section	$\alpha = 0.2$	$\alpha = 0.4$	$\alpha = 0.7$	$\alpha = 1.0$	$\alpha = 2.0$	$\alpha = 2.5$	$\alpha = 5.0$	$\alpha = 10.0$
	Sh_D			4.36				
	Sh_F			3.66				
	Sh_D	4.80	3.67	3.08	2.97	3.38	3.67	4.80
	Sh_F	5.74	4.47	3.75	3.61	4.12	4.47	5.74
	Sh_D	0.83	1.42	2.02	2.44	3.19	3.39	3.91
	Sh_F	0.96	1.60	2.26	2.71	3.54	3.78	4.41

Figure 4.9: Sherwood number for various channel cross section under laminar flow region where $\alpha = b/a$ (obtained from O’hayre et. al. [106])

4.6.2 Mass transport in GDL

4.6.2.1 Fick’s diffusion in porous GDL

The mass transport in PEMFC gas diffusion media driven by the concentration gradient of the transport species across its boundaries. Due to the electrochemical reaction in the catalyst layer reactants are depleted and they are transported by molecular diffusion from the gas channel to the electrode. The gas phase transport flux in PEMFC diffusion media is expressed as:

$$N_i'' = -D_{i,mix}^{eff} \frac{dC_i}{dx} \quad (4.26)$$

Where $-D_{i,mix}^{eff}$ is the effective diffusivity of species i in the mixture. Equation 4.26 is discretized to solved over the diffusion media and MPL to obtain species distribution inside the cell.

4.6.2.2 Mixture diffusivity calculation

In PEMFC cathode, generally a multicomponent gas mixture of oxygen, nitrogen and water vapor is used as the feed gas and the mixture diffusivity $D_{i,mix}$

need to be accounted instead of the binary diffusivity. It is calculated from the Wilke formula [153] as .

$$D_{i,mix} = \frac{1 - X_i}{\sum_{j \neq i}^n \frac{X_j}{D_{i,j}}} \quad (4.27)$$

where $X_i = P_i/P_{total}$ is the mole fraction of component i and $D_{i,j}$ is the binary diffusion coefficient calculated by the Fuller-Schetter-Giddings correlation [47]

$$D_{i,j} = \frac{1.013 \times 10^{-3} T^{1.75}}{P(v_i^{1/3} + v_j^{1/3})^2} \left[\frac{1}{M_i} + \frac{1}{M_j} \right]^{1/2} \quad (4.28)$$

Here v and M are the diffusion volume and molecular weight of a component. The correlation for binary diffusivity is been developed the kinetic theory. For binary gas mixtures the diffusivity is inversely proportional to pressure and increases with increasing pressure. The diffusion properties of common PEMFC gases is provided in table 4.2.

Gas	Diffusion volume	Molecular weight
Hydrogen, H ₂	7.07	2.016
Helium, He	2.88	4.003
Nitrogen, N ₂	17.9	28.013
Oxygen, O ₂	16.6	31.999
Carbon di-oxide, CO ₂	26.9	44.010
Water vapor, H ₂ O	12.7	18.015

Table 4.2: Diffusion properties of common PEMFC gases [153].

4.6.2.3 Effective diffusivity in porous media

To account for the geometric effects of the porous diffusion media open media diffusivity is corrected with geometric factors such as porosity and tortuosity. The porous gas diffusion media in PEMFCs is a multiphase system where solids conduct electron and the void space transport gaseous species. The porosity of the porous media is defined as:

$$\epsilon = \frac{\text{Void volume}}{\text{Total volume}} \quad (4.29)$$

Common PEMFC diffusion materials generally exhibit a porosity in the range of 65-75%[67, 88]. The tortuosity is defined as the ratio of actual path length for diffusion over the point to point normal path length as shown in figure 4.10.

$$\tau = \frac{\text{Actual path length}}{\text{Point to point normal path length}} \quad (4.30)$$

To open media diffusivity is corrected with the ratio of porosity and tortuosity to obtain the effective diffusivity as shown in equation 4.31

$$D_{i,mix}^{eff} = \frac{\epsilon}{\tau} D_{i,mix} \quad (4.31)$$

The ratio of porosity over tortuosity is obtained from limiting current experiments and implemented to correct the diffusivity.

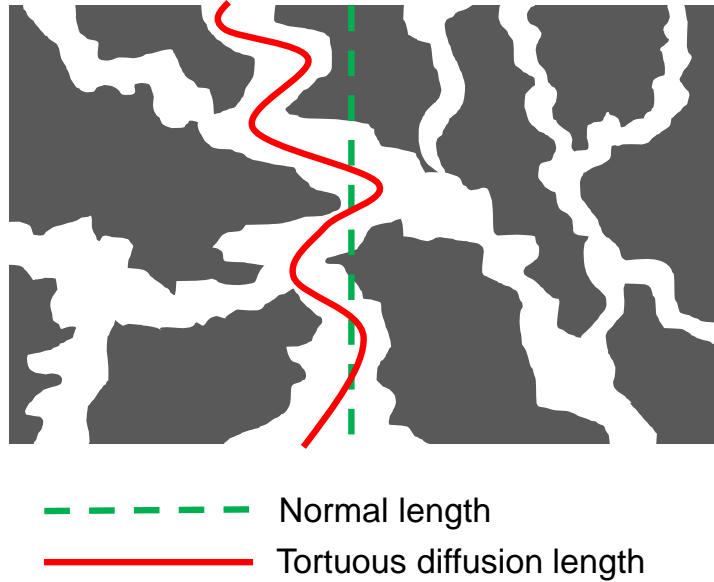


Figure 4.10: Schematic representation of tortuosity in porous diffusion media

4.6.2.4 Land and channel geometric effect

In addition to the porosity and tortuosity effect land and channel geometry of the flow channel also impact diffusivity mass transport in PEMFC gas diffusion media. Land and channel are unique features of the flow field design, where lands

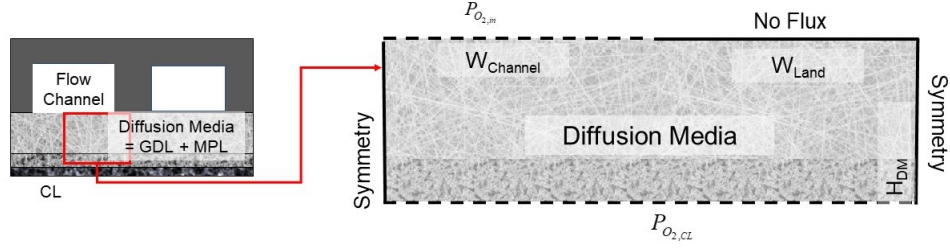


Figure 4.11: Computational domain and boundary condition for modeling the geometry effect of land and channel in PEMFC diffusion media

provide heat and electron conduction paths and channels transport fluids. Therefore, the fluids diffuse in the GDL and MPL from the flow channel is not a simple 1-D phenomenon. Gas transport between the catalyst layer and channel involves the transport of the species under both the land and channel. To account for this increased diffusion path, a geometric factor, f_{geo} , is incorporated in the model as a pseudo 1-D parameter for gas diffusion. Baker et al. [Baker citation] solved the Laplace's equation to obtain the f_{geo} . In our simulation, the Fick's diffusion with anisotropic diffusion coefficient is employed to obtain the f_{geo} . The governing equation for the simulation is

$$\nabla J_i = -\nabla \left(\rho D_i \nabla \omega_i + \rho \omega_i D_i \frac{\nabla M_n}{M_n} \right) = R_i \quad (4.32)$$

$$M_n = \left(\sum_i \frac{\omega_i}{M_i} \right)^{-1} \quad (4.33)$$

Figure 4.11 shows the modeling domain and the boundary conditions for the simulation. COMSOL Multiphysics was used to solve the governing equations and the value of f_{geo} is obtained from the following expression [63]

$$f_{geo} = \frac{P_{O_2}^{channel}}{avg(\partial P_{O_2} / \partial n) h} \quad (4.34)$$

Here $avg(\partial P_{O_2} / \partial n)$ is the average value of the normal derivative of P_{O_2} at the electrode.

4.6.3 Mass transport in MPL

Mass transport in the microporous layer is still governed by the Fick's diffusion but due to the length scale of the micro-porous layer the diffusion mechanism is different. In the microporous layer the mean pore radius of the pores are in the order of 80-150 nm and the mean free path for molecule to molecule interaction is much larger than the mean pore radius. As a result the molecule to pore-wall interaction becomes dominant and the diffusion falls under the Knudsen regime. Similar to molecular diffusion equation, the species flux is still dependent on the concentration gradient but the diffusivity is defined as the Knudsen diffusivity. The Knudsen diffusivity in the MPL can be calculated as

$$D_k^i = \frac{2r_p}{3} \sqrt{\frac{8RT}{\pi M_i}} \quad (4.35)$$

Where r_p is the mean pore radius, M is the molecular weight. It can be observed from equation 4.35 that Knudsen diffusivity is independent of pressure and the composition of the gas mixture.

For modeling mass transport in PEMFC MPL, we consider a parallel molecular and Knudsen diffusivity.

$$D_i = \left(\frac{1}{D_k^i} + \frac{1}{D_{molecular}^i} \right)^{-1} \quad (4.36)$$

4.6.4 Mass transport in CL

The catalyst layer is the most complex component of the cell which is made of carbon supported Pt catalysts and PSFA ionomeric binders. The structure of the electrode is highly porous with primary pores and secondary pores with Pt nano particles deposited inside and outside these pores. In addition ionomer thin-films surround the Pt/C agglomerates. Oxygen diffuses through the secondary pores and also dissolves in ionomer to reach the reaction sites (triple phase boundaries). Modeling oxygen and water vapor transport inside the CL is not straight-forward as multiple transport processes happen in parallel and in series and the transport properties are very difficult to obtain. In this model, we took an empirical approach to model oxygen transport in the electrode where the total non-pressure dependent transport resistance is obtained from the limiting current experimental data

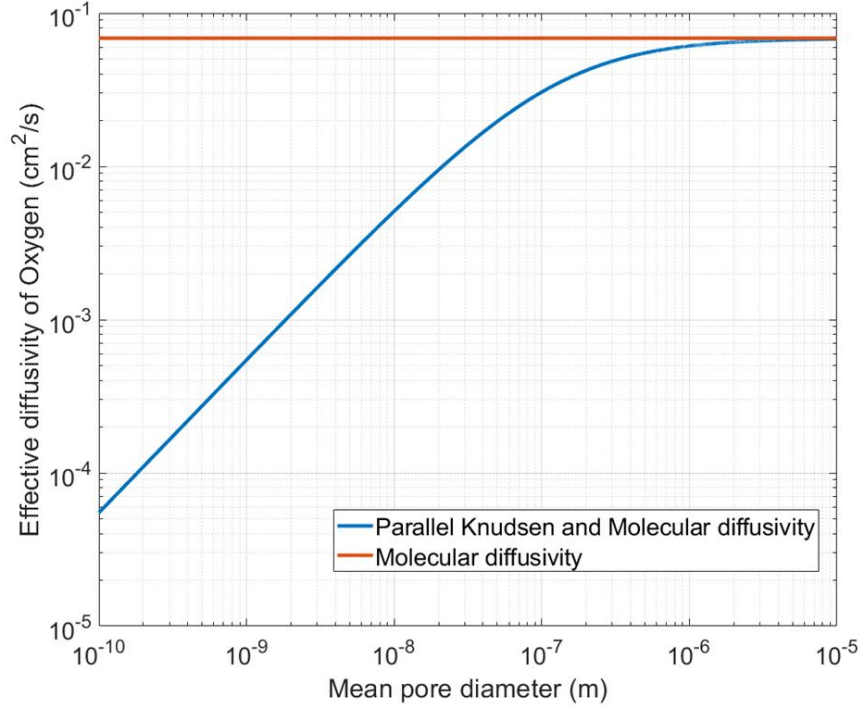


Figure 4.12: Comparison of parallel Knudsen and molecular diffusivity vs pure molecular effective diffusivity of Oxygen at 150kPa 80°C

and provided to the model as input. A more detailed discussion on the empirical formulation is provided on chapter 5.

4.6.5 Calculating mass transport loss

Mass transport loss also known as the concentration loss refers to the voltage loss due to the activity difference of oxygen, hydrogen and water at the catalyst layer compared to the flow channels. Oxygen and hydrogen concentrations in flow channel are higher compared to their concentrations on the catalyst active sites. As the value of current density is increased, reactant depletion in the catalyst layer starts to occur. Mass transport loss is calculated from equation 4.37.

$$\eta_{conc} = \frac{RT}{2F} \ln \left[\frac{\left(P_{H_2} P_{O_2}^{1/2} \right)_{CH}}{\left(P_{H_2} P_{O_2}^{1/2} \right)_{CL}} \right] + \frac{RT}{2\alpha F} \ln \left[\frac{P_{H_2,CH}}{P_{H_2,CL}} \right] + \frac{RT}{2\alpha F} \ln \left[\frac{P_{O_2,CH}}{P_{O_2,CL}} \right]^{1/2} \quad (4.37)$$

As can be seen from equation 4.37 to evaluate the η_{conc} the values of gas partial pressures, P_{H_2} , P_{O_2} , P_{H_2O} and temperature T at the catalyst layer are needed. To obtain the species and temperature distribution in the through-plane direction, the modeling domains need to be discretized. Flow channel resistance is calculated from the Sherwood number accounting for channel geometry. Fick's diffusion model is used to calculate the concentration in the diffusion media. The transport of hydrogen, oxygen and water in porous media is governed by Fick's law of diffusion

$$n_i'' = -D_{i,mix}^{eff} \nabla C_i \quad (4.38)$$

Here n_i'' represents the molar flux of species i . For hydrogen and water, the molar flux is $i/2F$ and for Oxygen $i/4F$. $D_{i,mix}^{eff}$ is the effective diffusivity of gas species i in the porous media. Finally, the partial pressure of any species i at catalyst layer can be calculated as:

$$P_i^{CL} = P_i^{CH} - \frac{iRT}{nF} [R_i^{CH} + R_i^{GDL} + R_i^{MPL} + R_i^{other}] \quad (4.39)$$

$$P_{H_2O}^{aCL} = P_{H_2O}^{ch} + f_w \frac{iRT}{2F} [R_{H_2O}^{CH} + R_{H_2O}^{GDL} + R_{H_2O}^{MPL}] \quad (4.40)$$

$$P_{H_2O}^{cCL} = P_{H_2O}^{ch} + (1 - f_w) \frac{iRT}{2F} [R_{H_2O}^{cCH} + R_{H_2O}^{cGDL} + R_{H_2O}^{cMPL}] \quad (4.41)$$

For equation 4.39, R_{other} is the non-fickian transport resistance obtained through limiting current experiments. The transport resistance in the channel for any species i is calculated from

$$R_i^{CH} = \frac{D_h}{Sh \times D_{i,mix}} \quad (4.42)$$

Here Sh is the Sherwood number and D_h is the hydraulic diameter of the channel. The transport resistance in the gas diffusion layer for any species i is obtained by the summation of all transport resistances of each discretized layer.

$$R_i^{DM} = \sum_{k=1}^N \frac{f_{geo} \delta_k^{DM}}{D_{i,mix}^{eff}} \quad (4.43)$$

Here, f_{geo} is the geometry factor that accounts for the increased diffusion length due

to land/channel design. Detail calculation method for f_{geo} is discussed in section 2.6. Partial pressure of hydrogen, oxygen and water at the catalyst layer can be calculated from equation 4.38. The gas diffusion media, MPL and catalyst layer are discretized to be solved numerically. Upwind finite difference scheme was used and the resulting equations were solved using the explicit method. The iteration converges for partial pressure when the oxygen diffusivity calculated from equation 4.27 reaches a specified numerical tolerance of 10^{-6} . The details of the oxygen diffusivity iteration are shown in Figure 4.14(c). The initial gas mole fractions at the catalyst layer are assumed to be the same as those in the channel.

4.7 Heat transfer

At an energy conversion efficiency of 50%, PEMFC produces the same amount of waste heat and electricity [65, 113]. Therefore, modeling the non-isothermal effects [33, 63, 122] of heat transfer inside a cell becomes particularly important for high current density operation. The reaction of oxygen and hydrogen is exothermic and the generated heat can be calculated by the energy balance equation:

$$q''_{total} = \left(\frac{|\Delta h|}{2F} - V_{cell} \right) \times i \quad (4.44)$$

where Δh is the reaction enthalpy. The reaction occurs in the cathode catalyst layer and the generated heat that is transported to both the anode side and cathode side. Heat transfer is governed by the heat conduction equation.

$$\dot{q}'' = -K\nabla T \quad (4.45)$$

Heat is being generated in the cathode catalyst layer and transported away to the coolant in anode and cathode plates. Heat transported to the anode side q''_a and cathode side q''_c is evaluated from the thermal resistance network. The thermal resistance network results in a 3 equations with 3 unknowns, q''_a , q''_c and cathode electrode temperature T_{cCL} . They can be solved by the matrix inversion problem in

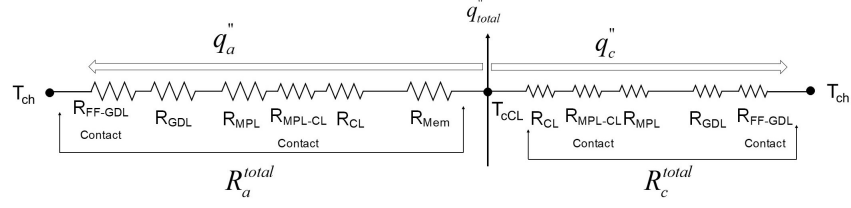


Figure 4.13: Thermal resistance network and heat flux direction for the through plane heat transfer in PEMFC

the following equation:

$$\begin{pmatrix} q_c'' \\ q_a'' \\ T_{cCL} \end{pmatrix} = \begin{pmatrix} 1 & 1 & 0 \\ R_c^{total} & 0 & -1 \\ 0 & R_a^{total} & -1 \end{pmatrix}^{-1} \begin{pmatrix} q_{total}'' \\ -T_{ch} \\ -T_{ch} \end{pmatrix} \quad (4.46)$$

In the thermal model, total resistance consists of bulk and contact resistances of GDL, MPL, catalyst layer, and membrane. Bulk thermal resistance, R_i , is equal to the thickness, δ_i , divided by the thermal conductivity, k_i . To obtain model output parameters at a given operating condition, the model performs three iterations. Detailed schematic diagrams of each iteration is provided in figure 4.8.

4.8 Solution algorithm

The programming code 1-D model is developed and solved numerically in MATLAB. Figure 4.14 shows the algorithm for the 1-D dry model. The model takes in the operating conditions (temperature, pressure, relative humidity and dry mole fraction of Oxygen) at the flow channel and the material properties of the PEMFC layers. For a input current density i , the temperature T and mole fraction X matrix is initialized with channel conditions. From the initial condition activation and concentration overpotentials are calculated. For the calculation of the ohmic loss knowledge of membrane water content is needed. Membrane water content is dependent on f_w . The value of “ f_w ” is calculated from the solution of membrane water balance equation 4.11 through the iterative loop shown in Figure A.1(a). As ohmic loss is calculated, the heat flux is obtained from equation and the temperature at all nodes are updated from temperature iteration loop as shown in Figure A.2. With

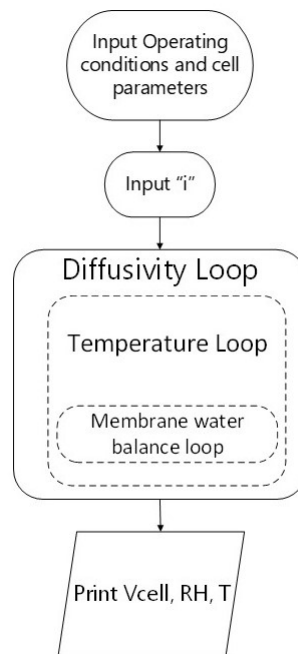


Figure 4.14: Solution algorithm for solving the governing equations of the 1-D PEMFC model

the updated temperature at the nodes, all the temperature dependent properties are updated and mole fractions are updated from the Diffusivity loop as shown in Figure A.3

4.9 Results: 1-D Dry Model

4.9.1 Simulation comparison with limiting current tests

The developed 1-D dry model is validated by both limiting current and dry polarization tests conducted under various operating conditions. Accurate measurement of limiting current is very challenging when a high concentration of oxygen is fed to the cell because the cell voltage reaches close to 0 V due to ohmic loss at high current densities. To avoid such condition, dilute oxygen concentrations (dry mole fraction of 4%, 3%, 2% and 1%) were used in this experiment. Another obstruction in limiting current studies occurs when the cell is run below 0.10 V under low oxygen concentrations. Under these conditions, the PEMFC converts into a concentration cell and hydrogen evolution reaction occurs on the cathode side [7]. The protons are converted to hydrogen in the cathode catalyst layer instead of producing water. This creates a hydrogen evolution current shift on the polarization curve. So, the limiting current was measured prior to the onset of the hydrogen evolution reaction.

Figure 4.15(a) shows the experimental measurements and model prediction of current density between 0.10 to 0.3 V at four dry mole fractions of oxygen when the pressure at the outlet was set to 150 kPa. The same experiment was repeated at four different pressure levels: 118 kPa, 150 kPa, 201 kPa, and 300 kPa. Results show that there is an almost negligible increase in current density as the cell voltage is lowered from 0.30 V to 0.10 V. This vertical slope of the polarization curve at low voltage is an indication that the cell is operating at the limiting current condition. It can be observed from Figure 4.15(a) that the model under-predicted the experimental results. This error was caused by the inaccuracy of the mass flow controller at such low flow rate ($< 2\%$ of the full range). Nevertheless, the slopes observed from Figure 4.15(b) agree well and are used for later calculation of total oxygen transport resistance.

The total oxygen transport resistance from the experiment and model are plotted against pressure in Figure 4.15(c). As can be seen from the graph, the total transport resistance increases linearly with pressure. This indicates that there was

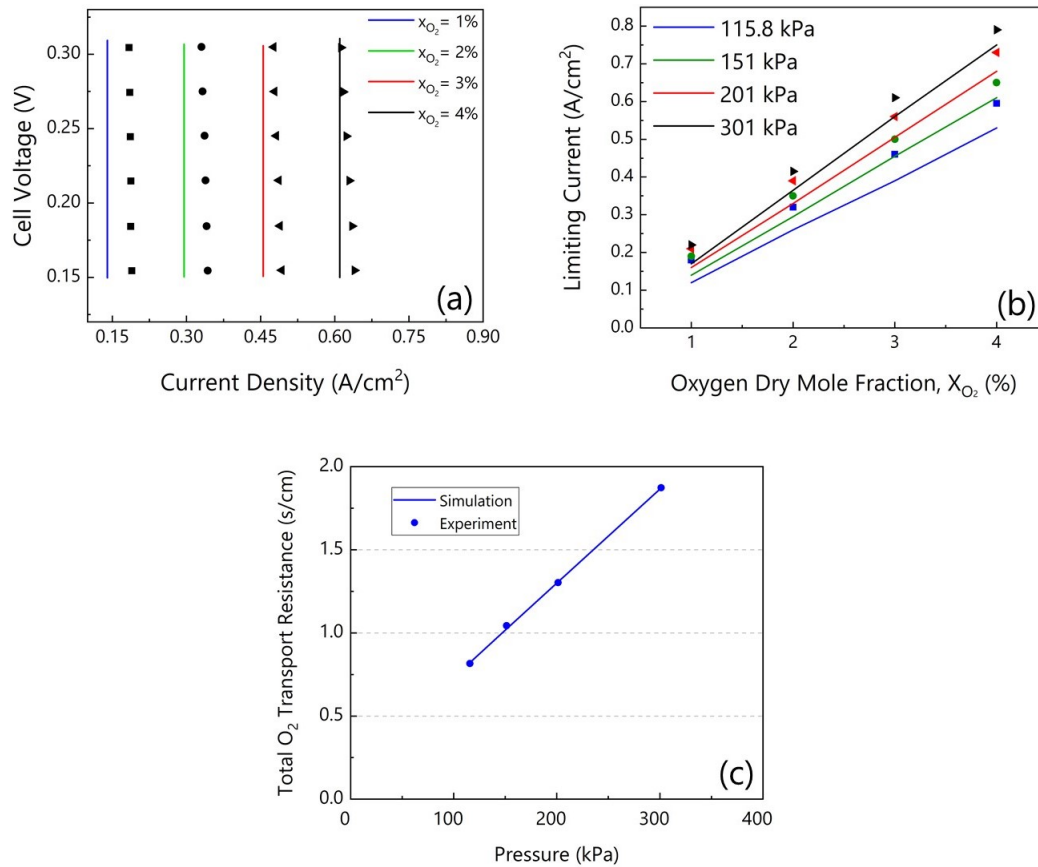


Figure 4.15: (a) Validation with dry polarization results at limiting current conditions of 150 kPa, 80°C and 62% RH. (b) Oxygen dry mole fraction at four different pressures at 80°C and 64% RH. (c) Dry transport resistance plotted as a function of total pressure (*solid line represents simulation and symbols represent experiment*)

no liquid water condensation during the test for all pressure levels. From the slope of the line fitted to experimental data, the ratio D/D_{eff} was calculated. Owejan et al. [109] and Baker et al [7] also conducted limiting current tests on Toray 060 gas diffusion media. Baker [8] reported the value of D/D_{eff} to be 4.41 under 26% cell compression. The overall transport resistance of the diffusion media is a function of many parameters, including fiber dimension, fiber loading, thickness, PTFE impregnation, MPL composition, MPL thickness, land/channel design, and compression of cell assembly. Simon et al. [128] showed that the total transport resistance is dependent on the cell compression. Therefore, we used the limiting current tests to directly measure the oxygen transport resistance. The ratio of D/D_{eff} under 23% cell compression was 5.05 obtained from the slope of the transport resistance vs pressure graph. The Y-intercept is used to calculate the non-pressure dependent resistance and later in the model as R_{other} . The R_{other} term includes the transport resistances from the catalyst layer, Knudsen diffusion in MPL, and interfacial resistance from GDL/MPL etc. The accuracy of this method can be observed from the model's prediction shown in figure 4.15(c).

4.9.2 Simulation comparison with polarization test

Dry polarization tests were performed on the same cell built for the limiting current tests to ensure consistency of the comparison. Experiments were conducted at three different operating conditions: 1) 100kPa 60%RH 80°C, 2) 100kPa 50%RH 70°C and 3) 300kPa 50% RH 80°C. Flow stoichiometry was set to 2 on both anode and cathode sides. The value of exchange current density is adjusted to the cell performance in kinetic region. Other kinetic parameters are obtained from the literature [47] as listed in table 2. Comparison between the simulation and experimental results are shown in Figure 4.16. The simulation shows good agreement with experiment in the kinetic and ohmic regions. The model successfully simulate the change in kinetic, ohmic, and transport losses under different pressure, temperature and relative humidity.

4.9.3 Impact of coupled heat and mass transfer

Figure 4.17 demonstrates the need to incorporate the important fuel cell physical phenomena to accurately predict PEMFC dry polarization performance.

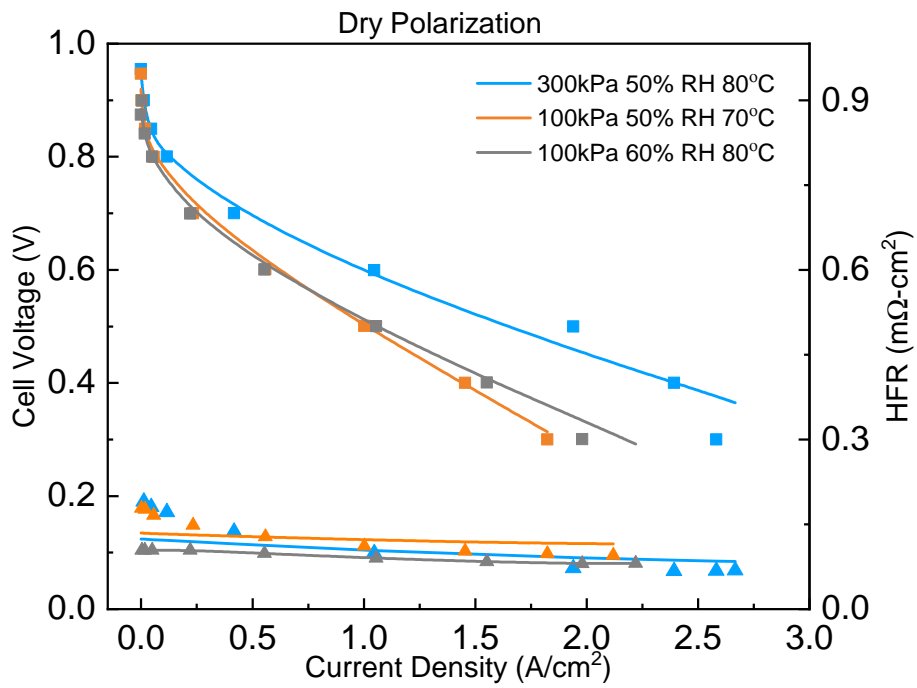


Figure 4.16: Model validation with dry polarization performance at three different operating conditions

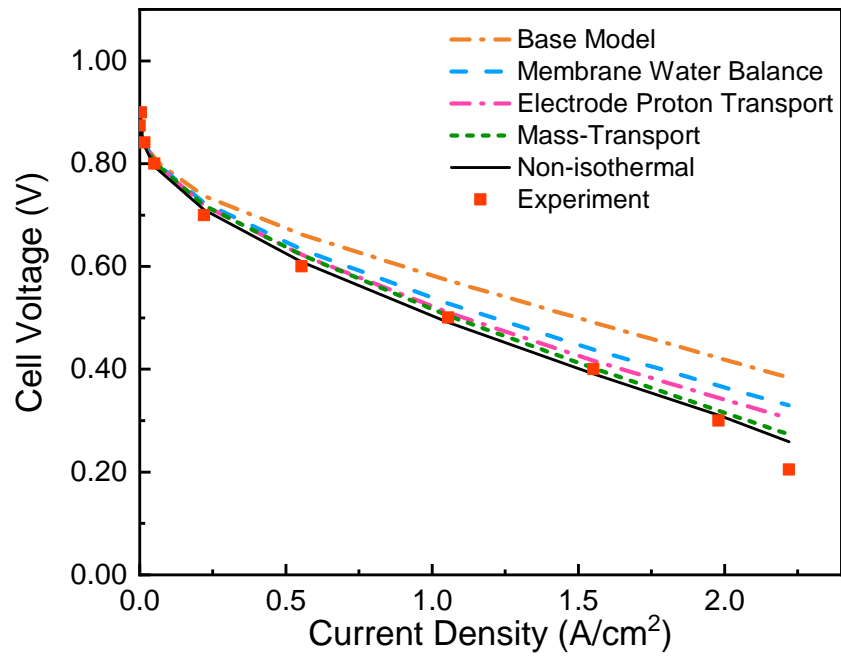


Figure 4.17: Effect of water balance, electrode proton transport loss, non-isothermal heat transfer, mass transport iteration on PEMFC modeling

The base model consists of a basic electrochemistry with no membrane water balance, electrode proton transport loss, heat transfer, mass transport iteration with a geometry factor and the R_{other} term. While it is possible to fit the base model results with experimental data, it would require adjustment of the membrane conductivity with a trial and error approach and the model would not be able to capture the fundamental physics. To include this physics in the base model, we added water balance equation and with the inclusion of the water balance, the model can capture the slope of the ohmic region more accurately. However, it can be observed that even adding the water balance, the model's prediction deviates significantly from the experimental data. Next, the electrode proton transport loss is added to the model. It is evident that the addition of proton transport loss in the electrode is also crucial for PEMFC performance prediction. Next, heat transfer is added to the water balance model and it can be observed that, with inclusion of a non-isothermal temperature distribution, the model's prediction becomes more accurate. Finally, we added the mass transport iteration to the non-isothermal model. The mass transport model includes the geometry factor " f_{geo} " and non-pressure dependent resistance term R_{other} . The need to couple thermal and water management has been demonstrated in literature [63, 150, 122, 33]. This study successfully integrated all important physics through iterative methods to improve the accuracy of the simulated results. In Figure 4.18, the temperature distribution inside a PEMFC sandwich and membrane water content distribution at a low ($0.5A/cm^2$), medium ($1.5A/cm^2$) and high ($2.5A/cm^2$) current density is plotted. Even though the total thickness of the PEMFC sandwich is relatively thin, a temperature gradient of 5 degrees exist at high current densities. This temperature gradient is very significant, especially at two phase flow regions due to the exponential nature of the water vapor curve. Figure 4.19 shows the membrane water content, λ , at three different current densities. It can be observed that the membrane water content distribution becomes very non-linear at high current densities, thus assuming linear water content in the membrane, especially at high current density, is not a good approximation for PEMFC simulations.

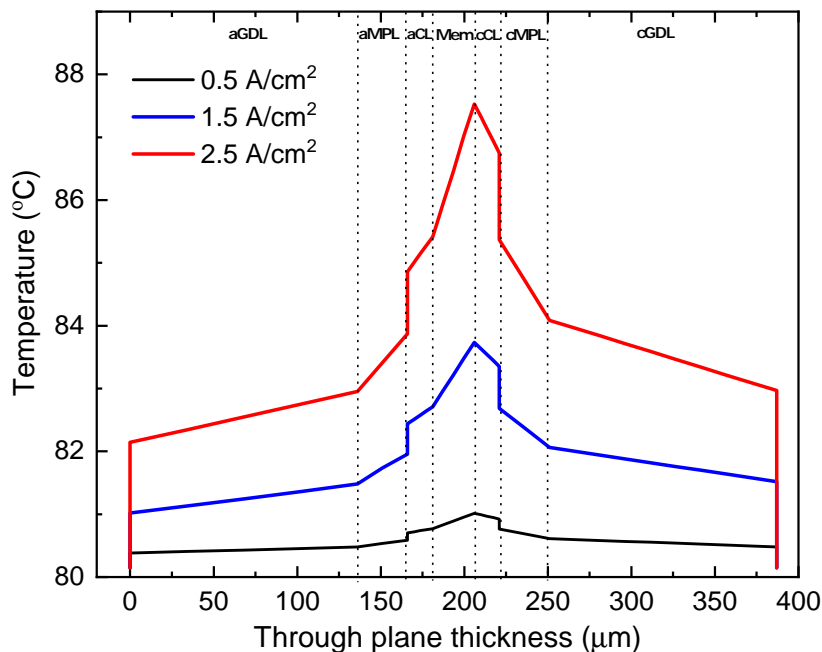


Figure 4.18: Temperature distribution in the PEMFC sandwich at three different current densities

4.9.4 Dry Oxygen transport resistance

The relative magnitudes of the various sources oxygen transport resistance at different operating pressure is shown in Figure 4.20. The resistances strongly depend on material properties, geometric properties and operating condition. Results are shown here for the cell built with PTFE treated Toray 060 DM, with 30 μm thick MPL and 125 μm GDL. Temperature was set to 80° C and RH was kept constant at 64%. Diffusion media (MPL and GDL) are the major source of oxygen transport resistance. More than half of the total resistance comes from the diffusion media and at 301 kPa, the diffusion media resistances contribute to almost three quarters of the total resistance.

Figure 4.20 also shows that non-pressure dependent resistance is not negligible for calculation. Most of the pressure independent resistance comes from the electrode. Diffusion media transport resistance depend on the ratio of porosity to

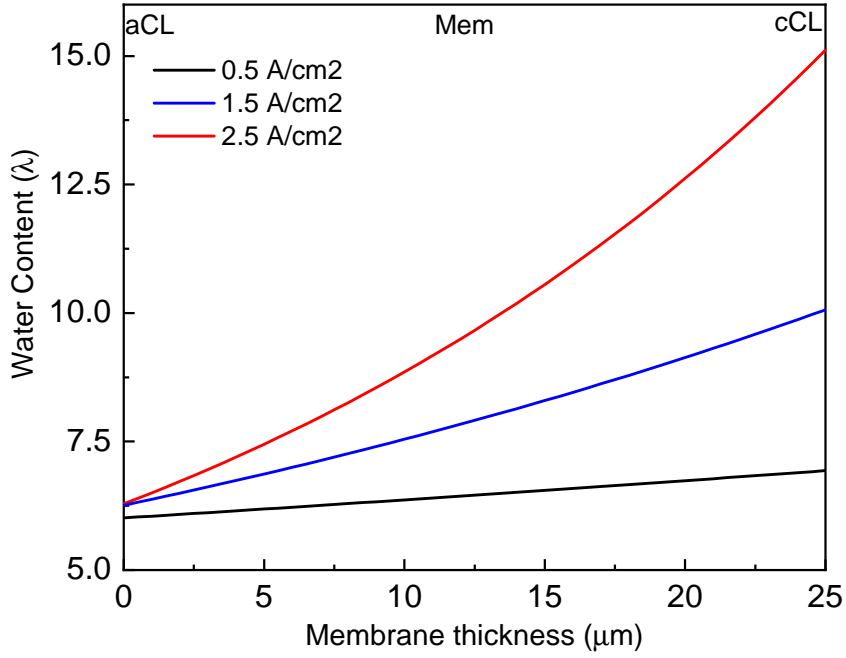


Figure 4.19: Membrane water uptake, λ , distribution in the membrane at three different current densities

tortuosity (τ/ϵ). This is an intrinsic property of the material which needs to be determined by in-situ or ex-situ experimental methods. For this simulation, the ratio is obtained from the slope in figure 4.15(c). In addition to the τ/ϵ ratio, the diffusion media anisotropy also plays a role in the transport resistance. In this simulation, the in-plane to through-plane diffusivity has been taken to be 1.8 [68,71]. This anisotropy is accounted for in the model by the f_{geo} factor in the transport equation. Apart from these material properties, the cell geometry also has an effect on the diffusion media transport resistance. The ratios of land/channel width and DM thickness/channel width are also factors that impacts f_{geo} . The value of f_{geo} used for this simulation is 1.540 and it has been calculated by solving Fick's diffusion equation.

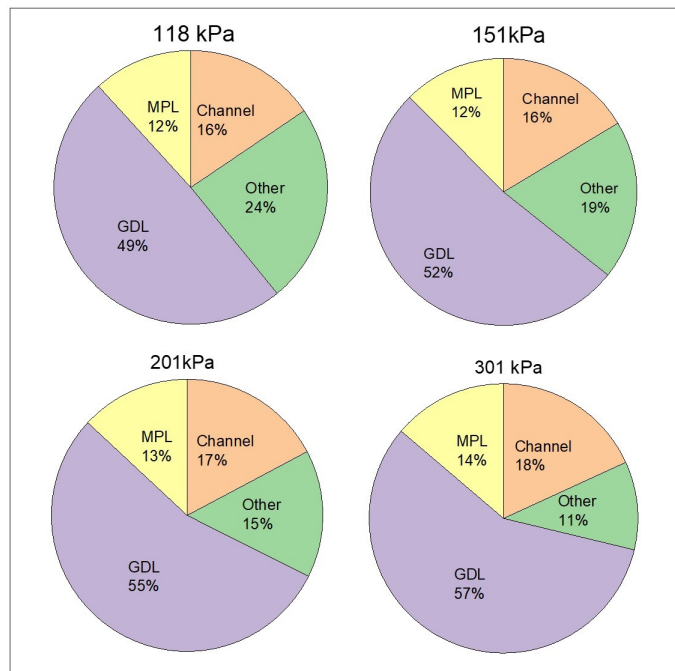


Figure 4.20: Simulation results of transport resistance contribution of diffusion media, channel and non-fickian resistances

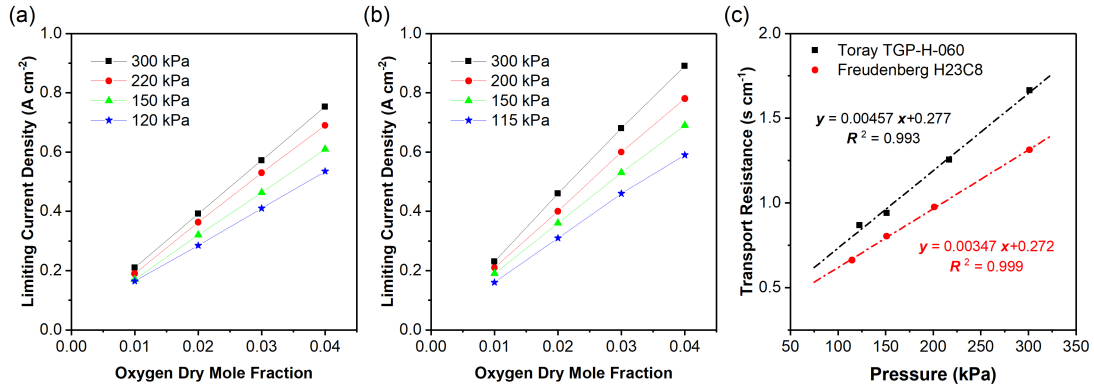


Figure 4.21: Limiting current as a function oxygen dry mole fraction for (a) Toray TGP-H-060 and (b) Freudenberg H23C8 and (c) the comparison of oxygen transport resistance as a function a pressure at 80 °C and 64 % RH.

4.10 Investigation water transport in GDL

In this section, an application of the developed 1-D model to investigate the effect of coupled heat and water transport on water condensation in the GDL is presented. Toray TGP-H-060 and Freudenberg H23C8 are two of the most widely used commercial gas diffusion materials for PEMFC applications. Freudenberg has smaller pore size and the pores are more randomly distributed compared to Toray [111]. The thermal transport properties of these two diffusion media also show significant differences due to material and processing differences [69]. The reported values of through-plane thermal conductivity of Toray and Freudenberg are $1.24 \text{ W m}^{-1} \text{ K}^{-1}$ and $0.11 \text{ W m}^{-1} \text{ K}^{-1}$, respectively [68, 17, 18]. In addition, Toray TGP-H-060 is slightly thinner than Freudenberg H23C8. The compressed thickness of Toray TGP-H-060 and Freudenberg H23C8 is $165 \mu\text{m}$ and $180 \mu\text{m}$, respectively. Due to the aforementioned structural and transport property differences cells built with Toray and Freudenberg GDL exhibit very different performance under dry and wet operating conditions due to their differences in structural and thermal transport properties.

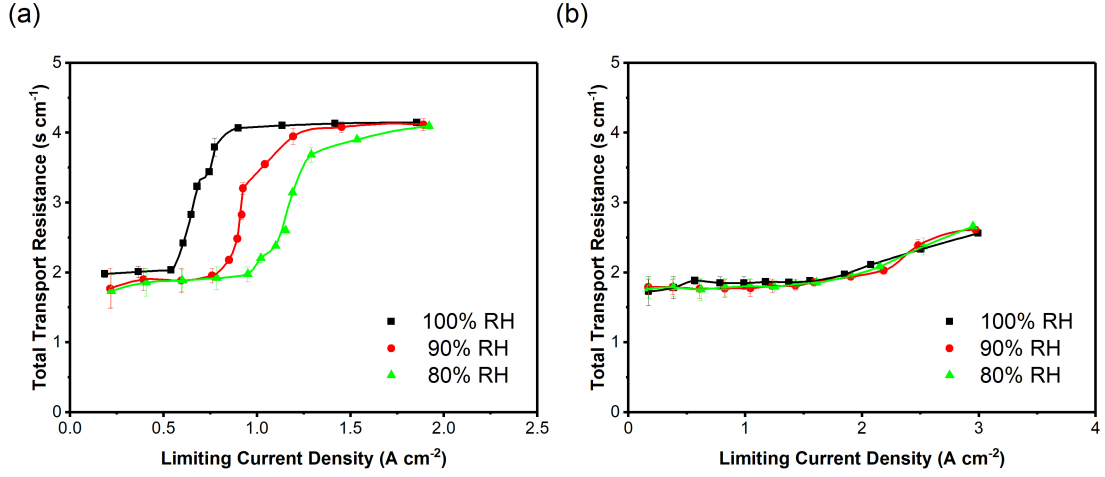


Figure 4.22: Wet oxygen transport as a function of relative humidity and limiting current for (a) Toray TGP-H-060 and (b) Freudenberg H23C8 at 70 °C and 300 kPa.

4.10.1 Experimental Observations

Results from limiting current experiment conducted at at 80 °C and 64 % RH is shown in figure 4.21(a) and (b). Based on the Equation 3.3, the total oxygen transport resistance can be calculated as a function of pressure. As shown in 4.21(c), Toray TGP-H-060 has a significantly higher oxygen transport resistance than Freudenberg H23C8. Following the analyses developed by Baker et al. and Rahman et al. [8, 7, 120], the ratio of tortuosity to porosity is calculated to be 5.0 and 3.5 for Toray TGP-H-060 and Freudenberg H23C8, respectively. The dry limiting current results demonstrate that, despite being thinner, the structure of TGP-H-060 has a higher gas transport impedance than the Freudenberg H23C8.

In contrast to the dry limiting current measurement, the wet limiting current tests were conducted to probe the oxygen transport resistance from the onset of liquid water condensation to reaching maximum liquid water saturation in the GDL by increasing oxygen concentration from 1 % to 21 %. Figure 4.22 shows the total transport resistances of both GDLs operating at 70 °C, 300 kPa, and three relative humidity conditions. Toray TGP-H-060 exhibits a clear transition of the transport resistance from no liquid water ($\approx 2 \text{ s cm}^{-1}$) to the maximum saturation ($\approx 4 \text{ s cm}^{-1}$). In addition, the onset water condensation of Toray TGP-H-060 has

	Unit	Toray	Freudenberg
Thermal Conductivity, k	$W m^{-1} K^{-1}$	1.24 [68]	0.11 [17]
Tortuosity over porosity, τ/ε		4.64	3.79
$k \left(\frac{\tau}{\varepsilon}\right)$	$W m^{-1} K^{-1}$	5.75	0.42

Table 4.3: Through-plane thermal conductivity and gas diffusivity of the GDL in Toray TGP-H-060 and Freudenberg H23C8.

an immediate effect on total transport resistance, which shows a rapid increase as in Figure 4.22(a). This explains why the limiting current density associated with onset water condensation increases with increasing channel RH. Similar to the observations from Caulk et al. [21], the transport resistance of Toray TGP-H-060 reaches a wet plateau, which indicates that the maximum saturation in the GDL is achieved. In contrast, the transport resistances of the Freudenberg H23C8 only increased gradually with increasing limiting current densities, regardless of the channel RH, as shown in Figure 4.22(b).

To investigate the reason for this phenomenon Chuang et. al. [28] employed neutron radiography to study water distribution in both GDLs and observed that water first condenses in Toray GDL near MPL and then propagates throughout the thickness. In contrast, water in the Freudenberg GDL first condenses in the GDL under the land and extends toward the MPL and leaves the GDL under the channel open for oxygen transport. The observation of the liquid water accumulation in the GDL explains the distinct trends of wet oxygen transport resistance.

4.10.2 1-D modeling analysis

To study the water condensation behavior, the 1-D steady-state simulation with the Toray and Freudenberg material properties is performed at a current density of $1.50 A cm^{-2}$ under 300 kPa, 70 °C and 90% RH. The ratios of the tortuosity over porosity are obtained from the limiting current measurement. The through-plane thermal conductivity of the two materials can be found in the literature [68, 17]. Both the thermal conductivity and gas diffusivity are material properties as listed in Table 4.3.

Calculated from the input operating conditions and material properties, figure 4.23 shows the simulation results of water saturation and vapor pressure distribution and relative humidity distribution inside the GDL for both the Toray and

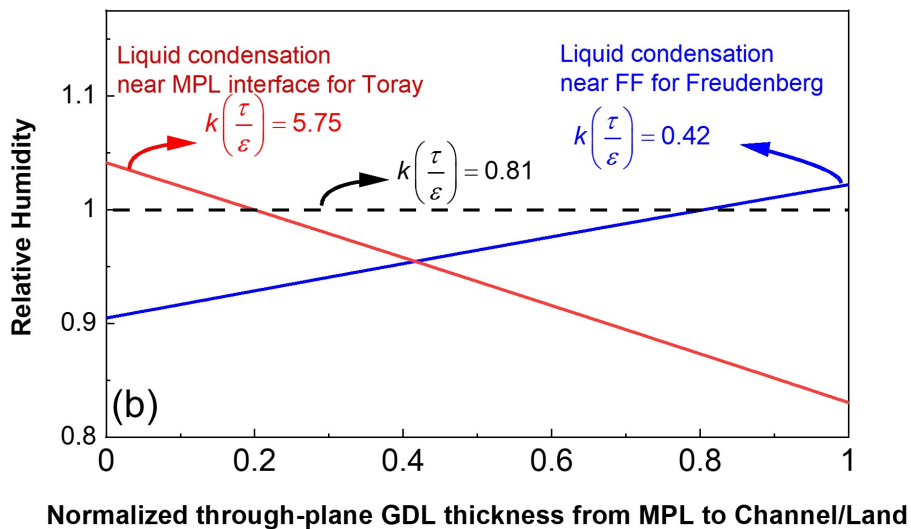
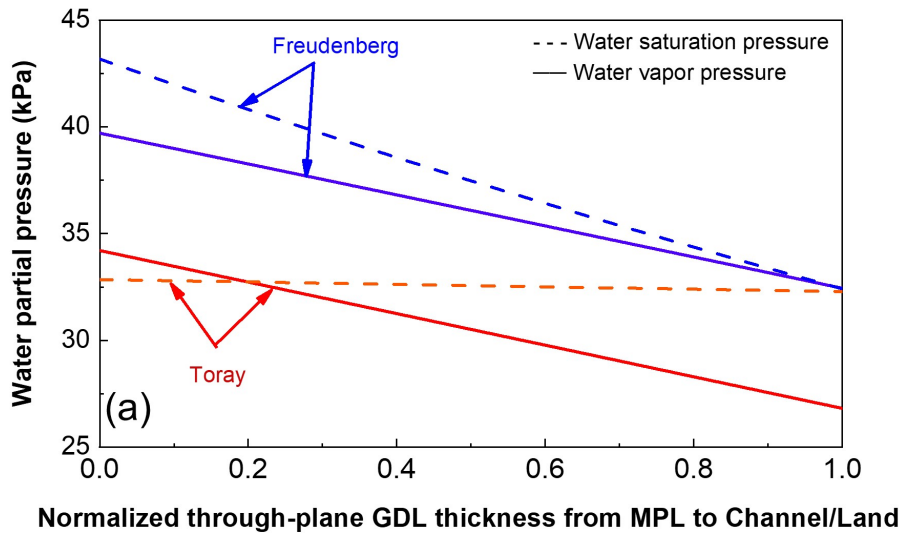


Figure 4.23: Simulation results of (a) Water vapor and saturation pressure and (b) Relative humidity distribution in Toray TGP-H-060 and Freudenberg H23C8 at 1.50 A cm^{-2} , 300 kPa, 70°C and 90% RH.

Freudenberg materials. Water condensation in the GDL occurs when RH exceeds 100%, which means that the water vapor pressure exceeds the saturation pressure. The water saturation pressure is only a function of temperature and the slope increases with decreasing through-plane thermal conductivity as shown in Equation 5.7. On the other hand, the slope of vapor pressure increases with decreasing $D_{eff}^{H_2O}$ or increasing (τ/ε) as shown in Equations 4.39 and 4.27. Due to the difference in the slope of saturation and vapor pressure, the onset of water condensation can happen in the GDL near the MPL interface, like the Toray material, or the channel/land interface, like the Freudenberg material, as shown in Figure 4.23(b). Even though the 1-D steady-state model only deals with vapor transport, the RH distribution in the GDL provides key insights into the onset water condensation location. The simulation results agree well with the liquid water distribution observed Chuang et. al. [28].

In summary, the location of onset condensation in the cathode GDL is governed by the complex interaction of the coupled heat and gas transport. The identified critical transport parameter is $k(\frac{\tau}{\varepsilon})$. Table 4.3 shows the critical transport parameter for both the Toray TGP-H-060 and the Freudenberg H23C8. When the value of $k(\frac{\tau}{\varepsilon})$ is high, such as for the Toray material, liquid condensation first occurs in the GDL near the MPL interface and directly blocks the oxygen paths. Therefore, liquid water in Toray materials causes a significant increase in oxygen transport resistance, as shown in Figure 4.22(a). On the other hand, with a small $k(\frac{\tau}{\varepsilon})$ value, such as observed for the Freudenberg material, liquid condensation first occurs in the GDL near the channel/land interface. Due to high convective flux and low heat transfer at the GDL and channel interface, water is less likely to condense. As a result, water condensation only occurs in the GDL under the land. This also explains why liquid water in the Freudenberg GDL only induces a gradual increase of oxygen transport resistance as shown in Figure 4.22(b). Based on our simulation results, the transition of the onset condensation location exists when the critical transport parameter, $k(\frac{\tau}{\varepsilon})$, is at around $0.81 W m^{-1} K^{-1}$ as shown in Figure 4.23(b) at $70^\circ C$ and 300 kPa. Further, this transition of the critical transport parameter increases with (1) cell operating temperature due to the increasing gradient of water saturation pressure and (2) decreasing total operating pressure because of the increase in diffusivity. Even though the transition of the critical transport parameter varies

with the operating conditions, the same guiding principle applies for optimizing GDL material design to reach high power density operation.

4.11 Summary

In this chapter a 1-D modeling framework for predicting dry oxygen transport resistance and limiting current has been presented. This model considers non-isothermal heat transfer, convective and diffusive gas transport, electrochemical reaction, shorting and cross over current, effects of land/channel geometry, membrane water balance, and proton resistance based on non-linear water content in the membrane. Limiting current experiments were conducted at 115.8 kPa, 151.34 kPa, 201.34 kPa and 301.34 kPa, at 80°C and 64% relative humidity. A dry polarization test was conducted at 70°C, 100 kPa and 60% relative humidity. Non-pressure dependent resistance and the ratio of porosity to tortuosity are obtained from the limiting current experiment to use in the model. Results from the 1-D model simulation were compared with both limiting current and dry polarization tests. Detailed discussion on incorporating water balance, heat transfer and mass transport was presented. It was demonstrated that at high current densities the membrane water content distribution becomes highly non-linear so modeling ohmic resistance with constant membrane conductivity or linear water content yields inaccurate result. In addition, inclusion of a non-isothermal temperature distribution inside the PEMFC sandwich is also important since a temperature gradient of 5-6 degrees exist at the high current density region. For modeling mass transport in a 1-D model, inclusion of “ f_{geo} ” factor is also crucial. “ f_{geo} ” accounts for land/channel geometry and anisotropic diffusion coefficients.

In addition, an application of the 1-D model is also presented where the effect of coupled heat and mass transport on water condensation in GDL is studied. This model has established a good basis for simulating dry performance of PEMFCs. However, under wet operating conditions, the two-phase transport characteristics will be very different from the dry operating conditions and the current model outputs will deviate significantly from the experimental results. In chapter 5 the physics to enhance models capability in two-phase flow conditions is presented.

Chapter 5

MODELING TWO-PHASE WATER TRANSPORT

In this chapter, a novel approach to simulate water transport in the gas diffusion media is presented. In addition to the two phase-flow in the gas diffusion media, a correlation for catalyst utilization with predicted electrode water activity based on experimental data is also developed to investigate the reduction of catalyst at high water saturation conditions. The overall model algorithm and the governing equations including reversible cell voltage, HOR kinetics, proton transport loss in membrane and electrode and mass transport loss remain same as the 1-D dry model.

5.1 Water tendril model in the GDL

When PEMFCs are operated at high humidity or high current density operating condition local water vapor pressure in the GDL exceeds the saturation pressure and water starts to condense in the GDL while filling up the pores, significantly inhibiting the diffusive gas transport. The increase in gas transport resistance primarily occurs due to the reduction of porosity (ϵ) and increase in tortuosity (τ), which reduces the overall effective diffusivity for gas transport. The increase in gas transport resistance with water saturation in the GDL can be observed from the limiting current experiment results shown in figure 5.1. The operating condition for the experiment were 300 kPa 70 °C 90%RH. From the oxygen transport resistance vs the limiting current density plot we can easily identify the three distinct regions: dry, transition and wet. In the dry region, oxygen transport resistance does not increase with limiting current and vapor diffusion is the primary transport mechanism for water. In the transition region, liquid water starts to condense in the GDL and the Oxygen transport resistance R_{O_2} starts to increase. In the wet region, entire diffusion media is saturated and essentially liquid water is transported through the water tendrils formed in the GDL. Wet region can be identified by the plateau in the oxygen transport resistance.

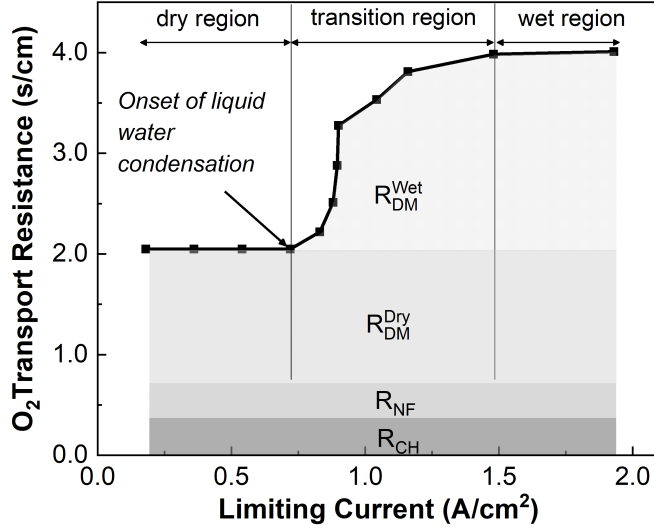


Figure 5.1: Experimental results from limiting current result showing the change of Oxygen transport resistance with increase in limiting current density at 300 kPa 70°C 90% RH

Based on this observations, Caulk and Baker [22] proposed an alternative two-phase water transport model and in this work we also adopted a very similar approach. For the purpose of modeling water transport in the GDL, the diffusion media can be separated into distinct dry and wet regions. When the local water partial pressure, $P_W(x)$ is less than the saturation pressure $P_{sat}(x)$, the diffusion media is considered dry. On the other hand, liquid water condensation occurs and the water tendril is formed when the local water partial pressure is greater than the saturation pressure. The schematic of the liquid water tendril model is shown in figure 5.2.

Depending on the operating condition and material properties the diffusion media can be fully dry, fully wet or partially wet throughout the thickness and even though the GDL is fully wet throughout the thickness, there are still pores available for gas transport due to its hydrophobicity [28, 12]. The length of the wet region of the diffusion media is defined as the “Tendril Length, $L_{tendril}$ ”. In the wet region, capillary pressure gradient is negligible and the oxygen transport resistance is a function of effective diffusivity. From the limiting experimental results, we can

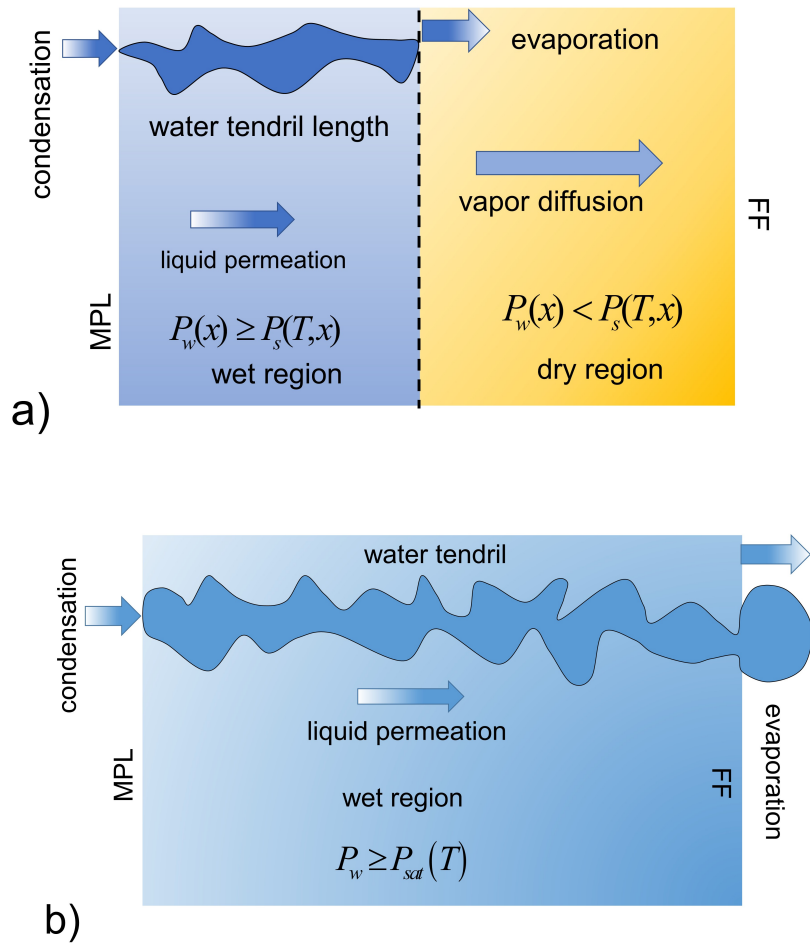


Figure 5.2: Schematic representation of water transport in GDL based on Caulk and Baker's [22] water tendril model (a) partially wet GDL ($t_{tendrils} < t_{GDL}$) (b) fully wet GDL ($t_{tendrils} = t_{GDL}$)

calculate the ratio of tortuosity to porosity of GDL as:

$$\frac{D}{D_{eff}} = \frac{\tau}{\epsilon} = \frac{(R_{O_2}^{Total} - R_{O_2}^{Ch} - R_{O_2}^{NF}) \times D_{O_2}^{OM}}{f_{geom} \times t_{GDL}} \quad (5.1)$$

where $R_{O_2}^{Total}$ is the total oxygen transport resistance (s/cm), $R_{O_2}^{Ch}$ is the oxygen transport in the channel, $R_{O_2}^{NF}$ is the non-fickian transport resistance from the MPL and electrode, f_{geom} is the geometriy correction factor for land/channel geometry and anisotropic diffusion, t_{GDL} is the thickness of the GDL. From equation 5.1 we can calculate effective diffusivity under dry and wet GDL. When diffusion media is dry, the gaseous species transport is calculated based on the dry effective diffusivity as:

$$\frac{\partial}{\partial x} \left(\frac{D_{eff,i}^{Dry}}{f_{geo}RT} \frac{\partial P_i}{\partial x} \right) = 0 \quad (5.2)$$

where P_i is the partial pressure of gaseous species ($i = O_2, H_2O$), and $D_{eff,i}^{Dry}$ the effective dry diffusivity for oxygen or water vapor ($i = O_2, H_2O$), R is the universal gas constant, T is the temperature. When the diffusion media is wet ($P_w \geq P_{sat}$), the gas transport is inhibited due to pore blockage from liquid water and the mass transport equation is corrected with wet effective diffusivity as:

$$\frac{\partial}{\partial x} \left(\frac{D_{eff}^{wet}}{f_{geo}RT} \frac{\partial P_i}{\partial x} \right) = 0 \quad (5.3)$$

Water transport in the GDL is primarily divided into vapor diffusion and liquid water permeation. When the GDL is dry, vapor water is transported via vapor diffusion.

$$\frac{\partial}{\partial x} \left(\frac{D_{eff}^{Dry}}{f_{geo}RT} \frac{\partial P_{H_2O}}{\partial x} \right) = 0 \quad (5.4)$$

When the GDL is partially or fully wet, water vapor is transported upto saturation pressure gradient:

$$\frac{\partial}{\partial x} \left(\frac{D_{eff}^{wet}}{f_{geo}RT} \frac{\partial P_s}{\partial x} \right) = 0 \quad (5.5)$$

For partially wet GDL, $t_{tendrill} < t_{GDL}$, as a result vapor diffusion occurs up to dry GDL thickness $t_{GDL,dry} = t_{GDL} - t_{tendrill}$. The liquid water flux $N_L(x)$ in the water

tendrils is obtained by subtracting the water vapor flux from the total water flux.

$$N_L(x) = (1 - f_w) \frac{I}{2F} - \frac{D_{eff}^{wet}}{RT} \frac{\partial P_s}{\partial x} = -\frac{\Delta P_{H_2O}^{liq}}{R_{H_2O}^{liq}} \quad (5.6)$$

Here f_w is the fraction of generated water that is transported from cathode to anode. In the wet GDL liquid water transport through the water tendrils and the water tendrils provide a very effective water removal pathway for with minimal transport resistance. It is assumed that the resistance for liquid water transport through the diffusion media is almost negligible i.e, $\partial P_{H_2O}^{liq} \approx 0$.

5.1.1 Two-phase heat transfer

Similar to gas and water transport, heat transfer is also divided into dry and wet regions. When GDL is dry, the local temperature can be solved by the energy conservation equation:

$$\frac{\partial}{\partial x} \left(k_{dry} \frac{\partial T}{\partial x} \right) = 0 \quad (5.7)$$

Where k_{dry} ($W/m - K$) is the dry thermal conductivity of the GDL, T (K) is the local temperature. For heat transfer in the wet region, water can be condensed or evaporated in the diffusion media. Therefore, associated latent heat (H) needs to be accounted for in the heat equation [22].

$$\frac{\partial}{\partial x} \left(k_{wet} \frac{\partial T}{\partial x} \right) = mH \quad (5.8)$$

5.1.2 Boundary Conditions

If the GDL is dry, the boundary conditions for heat and mass transfer at the GDL/MPL interface are:

$$q_c'' = -k_{dry} \frac{\partial T}{\partial x} (0) \quad (5.9)$$

$$(1 - f_w) \frac{I}{2F} = -\frac{D_{eff}^{dry}}{f_{geo}RT} \frac{\partial P_w}{\partial x} (0) \quad (5.10)$$

Where q_c'' is the heat flux towards cathode side and it is obtained from the solution of thermal resistance network discussed in [120]. If the GDL is wet then the boundary conditions are:

$$q_c'' + m_L H = -k_{wet} \frac{\partial T}{\partial x} \quad (0) \quad (5.11)$$

$$N_L = (1 - f_w) \frac{I}{2F} - \frac{D_{eff}^{wet}}{RT} \frac{\partial p_s}{\partial x} \quad (0) \quad (5.12)$$

Equation 5.7 to 5.12 are implemented in the heat and mass transport iteration loop of the model.

5.2 Local oxygen transport resistance

Experimental results from Suzuki et al. [134, 133], Kongkanand et al. [70, 71], Banham et al. [9] show that with low platinum loaded electrodes the oxygen transport resistance increases and this additional transport resistance is pressure independent and can generally be modeled with an additional resistance term in the electrode. Typically, the non-fickian transport resistance consists of three transport resistance, one from small pores in the microporous layer, one from the small pores in cathode and the third for a region close to the Pt surface.

$$R_{NF} = R_{NF}^{MPL} + R_{NF}^{CCL} + \frac{R_{O_2}^{Pt}}{r.f.} \quad (5.13)$$

Greszler et al [45] conducted limiting current experiment to quantitatively evaluate the non-Fickian transport resistance for low Pt loaded cells. They found electrodes with low roughness factor show a higher non-Fickian O_2 transport resistance. When roughness factor is reduced more oxygen must be delivered to a smaller Pt surface and this results in a higher transport resistance. We hypothesis that the same phenomena can also occur in PEMFCs with relatively highly loaded (0.3-0.4 mg) Pt electrodes during severe electrode flooding. Even though the original roughness factor is relatively high, at high current density liquid water can flood the active reaction sites. This can reduce roughness factor which results in a higher oxygen transport resistance at electrode. Kongkonad et al. [71] experimentally calculated the correlation between non-Fickian O_2 transport resistance and roughness factor

as, $R_{NF} = \frac{11.2}{r.f.} + 0.053$. This correlation is implemented in the model to account for the non-Fickian transport resistance as roughness factor is reduced due to water flooding or low Pt loading.

5.3 Results: 1-D Wet Model

5.3.1 Experimental validation of the tendril model

In order to validate the simulation results with PEMFC experimental performance limiting current and polarization tests were conducted. Dry limiting current tests were conducted at 80 °C, 64% RH and 100,200 and 300 kPa with varying Dry oxygen mole fraction of oxygen from 4% to 1%. For wet limiting current experiment operating conditions were:300 kPa, 80°C and 80% and 90% RH with oxygen with varying dry oxygen mole fraction from 21% to 1%. Figure 5.3 shows the comparison simulation results with limiting current and polarization experiments after inclusion of tendril model to the 1-D dry model. It can be observed from figure 5.3(a) and 5.3(b) that the model is capable of predicting the oxygen transport resistance R_{O_2} under both dry and wet operating condition condition. The authors would like to draw attention to the fact that, while most of the models published in literature can predict the polarization performance none has shown to be effective at predicting the oxygen transport resistance under fully humidified condition and the importance of predicting OTR at wet operating condition has been highly neglected. This shows the efficacy of the tendril model approach to simulate two phase transport resistance. The tendril model is very effective to predict the dry transport, the onset of liquid water condensation point and full GDL saturation with high accuracy. However, the prediction of the onset of liquid condensation point and the transition region is very sensitive to the water transport parameters used. For this simulation the water diffusivity values from Zawodzinski et al [160] and EODC from Gottesfield et al [123] is used. Details of the model sensitivity to water diffusivity and EODC is discussed in section 5.3.5.

Simulation results of polarization performance is compared with the experimental results in figure 5.3(c) and it can be observed that while the model can still predict the diffusion limiting current due to GDL flooding, it fails to capture the performance losses originating from electrode to low catalyst utilization in the electrode due to electrode flooding. To capture these effects we adopted an empirical

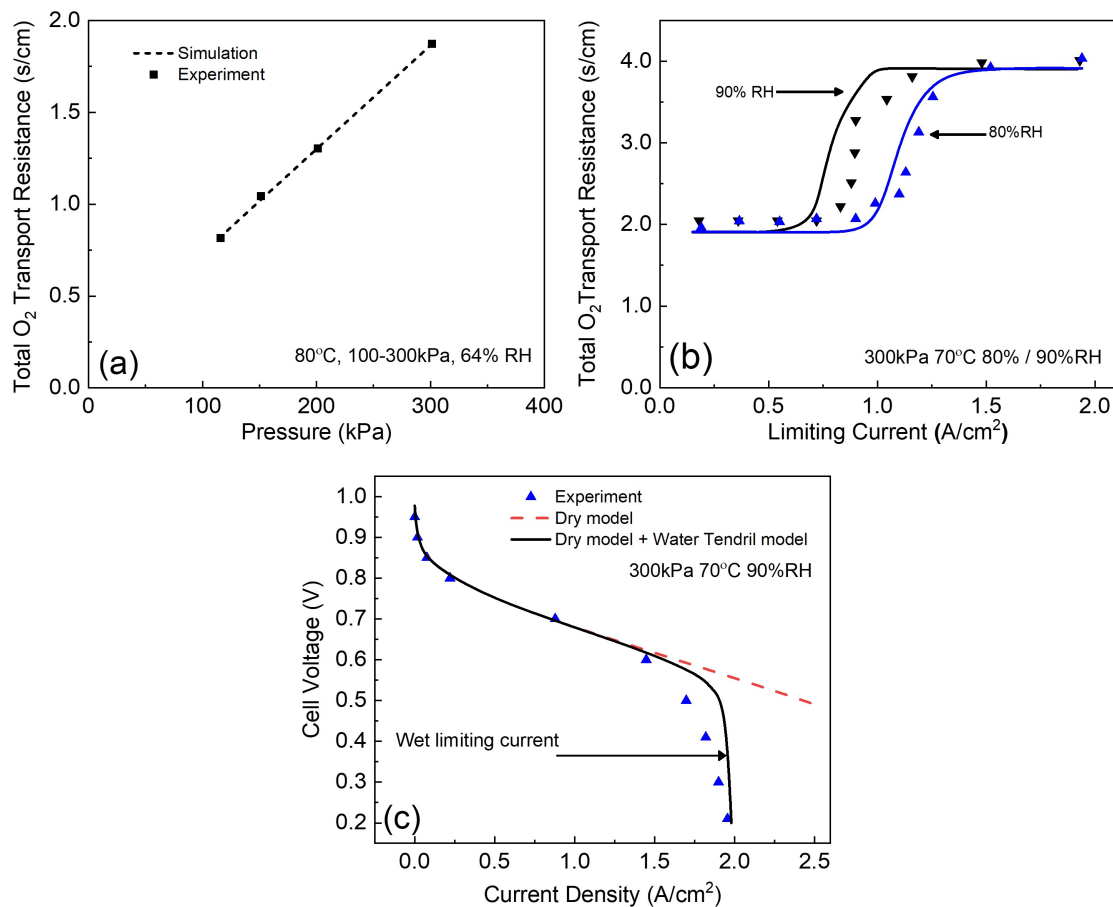


Figure 5.3: Comparison of 1-D simulation results with limiting current experiment for Oxygen transport resistance under (a) dry operating condition, 100-300 kPa, $80^\circ C$, 64% RH (b) wet operating conditions 300kPa $70^\circ C$ 80%/90% RH (c) polarization performance compared with 1-D dry and 1-D dry with water tendril model under wet operating condition 300kPa $70^\circ C$ 90%RH

approach.

5.3.2 Additional Performance losses

At high humidity and high current density operation liquid water starts to condense in the PEMFC electrode and this phenomenon is referred as the electrode flooding. At high water saturation levels in electrode the active reaction sites get blocked by liquid water resulting in a reduced catalyst utilization. Modeling liquid water transport inside the catalyst layer is extremely challenging due to both nano scale transport of water inside the CL and the uncertainty associated with key transport properties, which can only be determined by ex-situ experiments. In addition, the structure of the catalyst layer is extremely complex as it includes carbon agglomerates, primary and secondary pores, thin film of ionomer and Pt particles of different size and shapes [23]. Experimentally measuring the two-phase transport properties of thin electrode layer is very difficult and uncertain. In order to accurately model liquid water transport in electrode one would need to simulate at an agglomerate scale [24, 56, 88] which is computationally very expensive requiring high performance computing resources to solve the coupled transport and kinetics equation over the millions of nodes in a single agglomerate. While this approach is informative at the agglomerate scale, these simulations are almost impossible couple in a full PEMFC simulation model because of the order of magnitude difference in PEMFC geometries.

In this work, we derived an empirical correlation to model liquid water condensation and water coverage in the cathode catalyst layer. In the developed 1-D model the performance losses from HOR kinetics and Pt-oxide coverage dependent ORR kinetics, ohmic loss in catalyst layer and membrane, and mass transport due to reactant depletion in the electrode have already been accounted. We assume that the performance loss that is observed in high current density operation under wet operating condition is due to the reduced catalyst utilization as a result of water condensation inside the catalyst layer. To calculate the reduced catalyst utilization, simulations were fitted with roughness factor ($r.f. = ECSA \times Pt\ loading$) to match the experimental cell performance.

In figure 5.4 simulation result of water activity a_w in the cathode electrode is plotted along side the polarization performance. Simulation results show that at

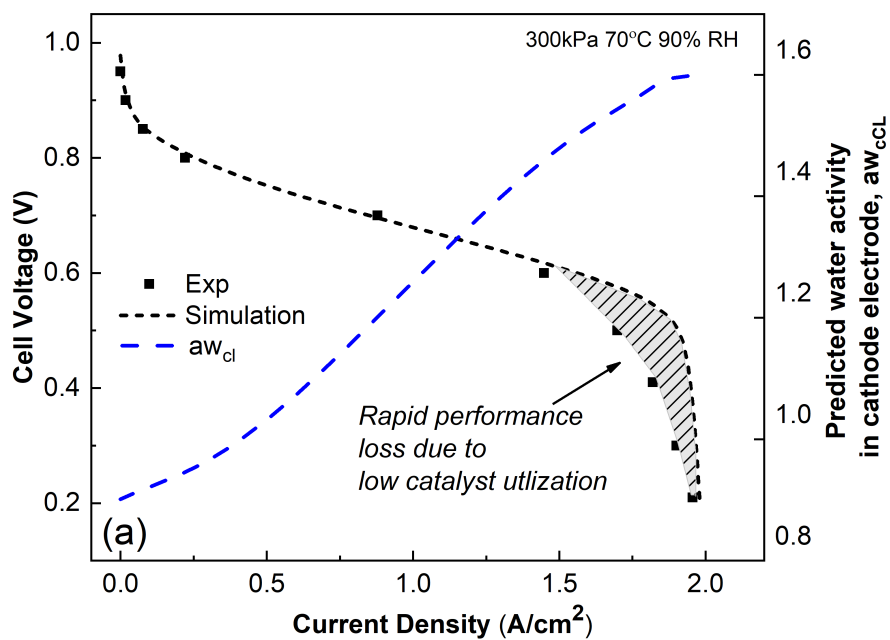


Figure 5.4: Experimental results showing rapid performance loss due to low catalyst utilization at electrode flooding at 300kPa 70°C 90%RH. Shaded region represents the performance loss not captured with GDL tendril model.

300 kPa 70°C and 90%RH operating condition water activity in the electrode is less than 1 until 0.50 A/cm^2 . As current density is increased the catalyst layer water activity is also increased finally reaching a value of 1.60. The gray shaded region in figure 5.4 shows the performance loss due to low catalyst utilization as a result of liquid water coverage in the catalyst layer. To address this additional performance loss from liquid water coverage the reduction in roughness factor was calculated to match the cell performance. The catalyst utilization factor is defined as:

$$\chi = \frac{r.f.}{r.f._{dry}} \quad (5.14)$$

Where $r.f._{dry}$ is the roughness factor of the dry electrode calculated as

$$r.f._{dry} = EC SA \times Pt \text{ loading} \quad (5.15)$$

To formulate an empirical correlation between the catalyst utilization factor χ and water activity in the electrode, seven wet polarization experimental results were fitted with reduced roughness factor to capture the additional performance losses. Figure 5.5 shows the catalyst utilization factors at different operating conditions with the predicted water activity in the electrode. The catalyst utilization factor (χ) shows a repetitive pattern where the value of χ remains 1 until a certain water activity and then it drops rapidly. The catalyst utilization factor and local water activity results can be fitted with a sigmoid function as:

$$\chi = \chi_{wet} + \left(\frac{\chi_{dry} - \chi_{wet}}{1 + \exp\left(\frac{a_w^{cCL} - a_w^{cr}}{A_1}\right)} \right) \quad (5.16)$$

where χ_{dry} is the catalyst utilization of the completely dry electrode, χ_{wet} is the catalyst utilization factor of the fully wet electrode, a_w^{cCL} is the water activity of the catalyst layer, a_w^{cr} is the onset water activity point after which catalyst utilization starts to reduce rapidly. The liquid water coverage of the catalyst layer can be obtained as:

$$\theta_w = (1 - \chi) \quad (5.17)$$

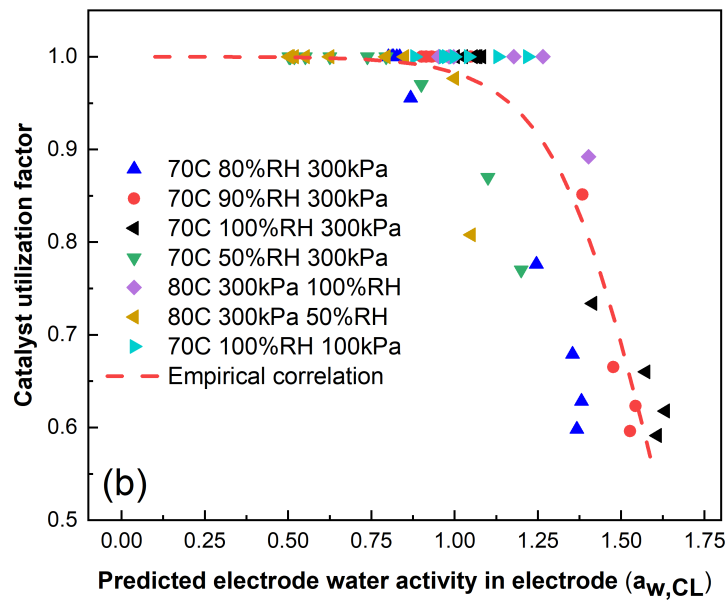


Figure 5.5: Simulated catalyst utilization factor with local water activity in the electrode at different wet operating conditions at 300kPa 70°C 90%RH.

The roughness factor in the Pt-oxide coverage dependent ORR model (equation 5.18) can be corrected with the liquid water coverage term to capture the performance losses associated with water condensation in the electrode as shown here:

$$i = i_o \times (1 - \theta_w) rf \times \left(\frac{P_{O_2}}{P_{O_2,ref}} \right)^m (1 - \theta_{PtO_x}) \exp \left(\frac{-\alpha F \eta}{RT} \right) \exp \left(\frac{-\omega \theta_{PtO_x}}{RT} \right) \quad (5.18)$$

Here, P_{O_2} is the oxygen partial pressure in the electrode, $P_{O_2,ref}$ is the oxygen partial pressure at reference atmospheric condition, θ_{Pt-O_x} is the Pt oxide coverage, α is the reaction symmetry coefficient, ω is the energy parameter for Temkin isotherm, R is the universal gas constant and T is the temperature in electrode. The values of the all modeling parameters are provided in table 5.3.3.

5.3.3 Polarization experiment

With the implementation of water tendril and the empirical catalyst utilization model, the 1-D model can predict polarization performance with very good accuracy. In figure 5.6, simulation result is compared with fuel cell experimental performance at 300 kPa, 90% RH, 70°C. To fit the model in the kinetic region, the value of exchange current density, i_0 is adjusted. Value of Tafel slope has been used as $70mV/dec$. Ohmic resistance in membrane and electrode is calculated based on the local water content λ . The dotted line represents the 1-D dry model and the solid line represents the 1-D two-phase PEMFC model. The 1-D dry model can simulate the performance up to 0.50V with reasonably high accuracy. However as the cell voltage is further lowered the model starts to deviate from the experimental measurements. This is because at high current density water starts to condense in the GDL and in electrode an the single phase model fails to capture the physics. To predict the fuel cell performance at low cell voltage/high current density, it is extremely important to capture the effects of water condensation in the GDL and electrode. The τ/ϵ values are obtained from the limiting current measurements for both dry and wet diffusion media but the electrode flooding parameters are adjusted to fit the polarization curve at high current density.

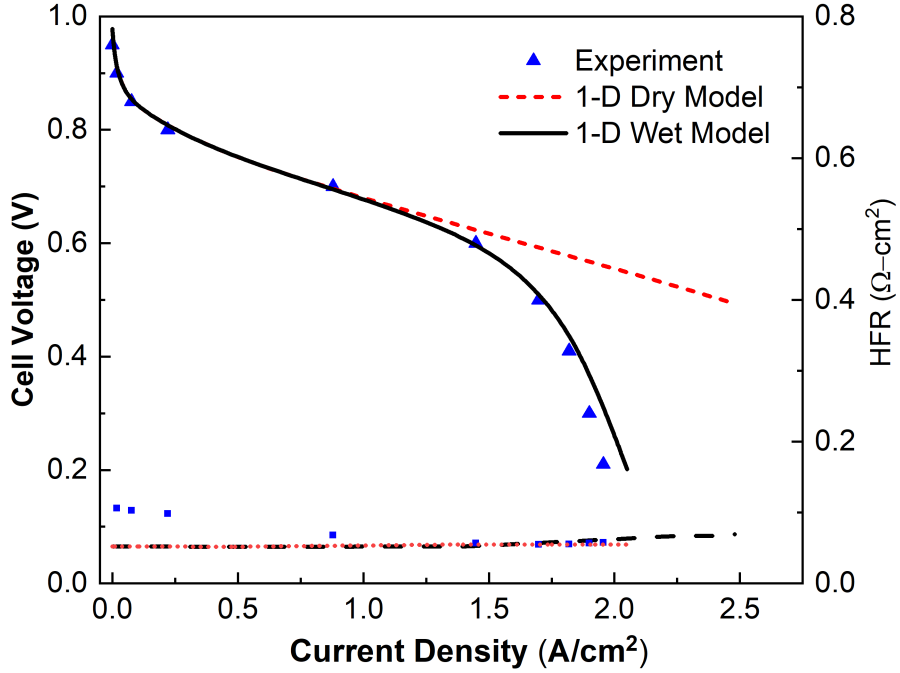


Figure 5.6: Simulation of polarization performance at 300kPa 90%RH, 70°C showing the performance comparison between dry and two-phase PEMFC model.

5.3.4 GDL and electrode flooding

At high current density or highly humidified operating conditions, water condense inside fuel cell. Lister et al [87, 88] have shown that liquid water forms finger like tendrils while penetrating through the hydrophobic diffusion media. In this model we have defined tendrill length as the ratio of wet ($P_{H_2O}(x) > P_{sat}(x)$) and total GDL thickness. The tendrill length, L_t/t_{GDL} provides a quantitative understanding of the water tendrill propagation through the GDL. The growth of normalized water tendrill length is plotted with current density at two different operating conditions in figure 5.7. It can be observed that as relative humidity is increased, the onset of liquid water condensation point shifts towards left side. This indicates at higher RH, water condensation in GDL occurx at much lower current densities. For the 90%RH case, tendrill length reaches the full length of the GDL at 1.20 A/cm^2

Table 1. Parameters for 1-D model

Tendril model parameters	
Ratio of tortuosity and porosity at dry GDL $(\tau/\epsilon)_{dry}$ (calculated)	4.56
Ratio of tortuosity and porosity at wet GDL $(\tau/\epsilon)_{wet}$ (calculated)	10.78
Thermal conductivity of dry GDL, (k_{dry}) , $W/m - K$ [68]	1.21
Thermal conductivity of wet GDL, (k_{dry}) , $W/m - K$	1.41
Latent heat of condensation, H (kJ/Kg)	2268
Oxide coverage dependent ORR kinetics	
Exchange current density, i_0 , A/cm^2 (fitted)	3.0×10^{-5}
Energy parameter of Temkim isotherm, ω , $Joule$ [131]	3.0×10^3
Tafel slope, $b = 2.303RT/\alpha F$, mV/dec	70
Reaction order, m [131]	0.75
Electrode catalyst utilization model	
Dry cathode roughness factor, (χ_{dry})	1
Fully saturated cathode roughness factor (χ_{wet})	0.20
Transition water electrode water activity, $a_{w,cr}$	1.20

Table 5.1: Simulation parameters for the water tendril, ORR kinetics and electrode catalyst utilization model

current density and for 80%RH case, it occurs at $1.70 A/cm^2$. Thus the oxygen transport resistance increases very rapidly as the effective diffusion coefficient is reduced.

Benziger et al [12] also observed that once the water tendrils are formed, with a very small increase in capillary pressure the GDL can sustain the flow of water through the GDL. Based on this we assume a very low water transport resistance inside the water tendrils. It needs to be noted that even when the GDL is fully flooded, only a fraction of the pores are blocked by liquid water and the rest are available for gas phase transport. Even when water tendril length equals to the thickness of the total diffusion media, not all the pores are not blocked by liquid water.

Figure 5.8 shows simulation results of how electrode flooding occurs as current density is increased. Due to the complex microstructure of the electrode predicting liquid water flooding inside the electrode is extremely difficult. In this work we formulated simplistic electrode flooding model based on an empirical correlation. The simulation results show that after a critical water activity at the electrode, liquid water coverage increases rapidly. The liquid water blocks the active reaction

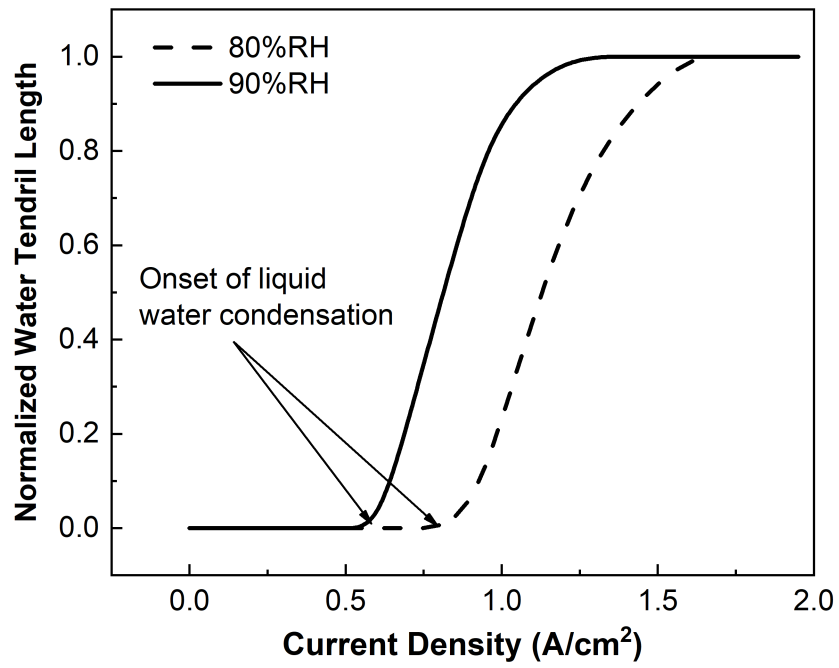


Figure 5.7: 1-D simulation of water tendril growth in GDL with increasing limiting current density at 300 kPa 70°C 80%, 90%RH.

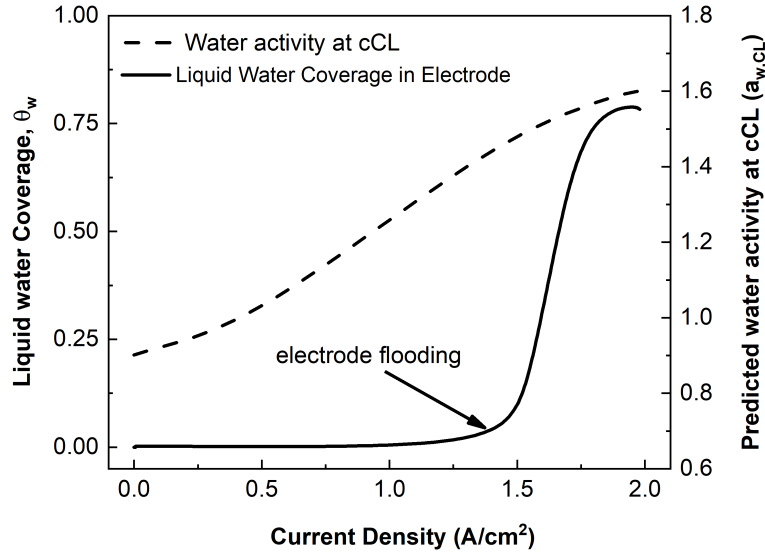


Figure 5.8: Simulation result of local water activity and liquid water coverage in electrode at 300 kPa 70°C and 90%RH

sites and reduces the roughness factor. This effect is observed in the polarization curve from the rapid decline in cell voltage at very high current densities. Our model predicts that at very high current density almost 75% of the active reaction sites can be blocked by liquid water coverage. Thus improving fuel cell performance at high current density is reliant upon excellent water management of the cell.

5.3.5 Effect of membrane water transport properties on tendril model

Accurate calculation water transport across the membrane is critical for simulating two-phase flow in the diffusion media as the value of f_w can severely impact water partial pressure inside the cell. Water transport across membrane is a complex and intricate balance between water back diffusion and electro-osmotic drag. In PEMFCs water is generated in the cathode side and as a result water concentration in the cathode side is generally higher than the anode side. Because of this concentration gradient water diffuses towards the anode from the cathode and this phenomenon is commonly referred as water back-diffusion. In addition the generated protons from HOR reaction in anode moves towards cathode catalyst layer and drag one or more water molecule during the proton transport process. This is

phenomenon is known as electro-osmotic drag and the electro-osmotic drag coefficient (n_{drag}) is used to quantify the number of water molecules that are dragged per proton. Applying the mass conservation principle in membrane, water balance equation is formulated as:

$$n_{H_2O}'' = -f_w \frac{i}{2F} = \frac{i}{F} n_{drag} \frac{\lambda}{22} - \frac{\rho_{dry,mem}}{M_{mem}} D_\lambda \frac{d\lambda}{dz} \quad (5.19)$$

Where λ is the membrane water content, $\rho_{dry,mem}$ is the density of the dry membrane, M_{mem} is the membrane equivalent weight and D_λ is the water diffusivity through membrane. The reported values of D_λ and n_{drag} shows significant variation in literature. For example, the values of D_λ varies by order of magnitudes depending on the experimental measurement technique. Compared to water diffusivity, there is slightly more agreement on the values and overall trend of n_{drag} but still the variation is considerably high. A. Kosuglu et. al. reviewed this issue in detail [82]. To study the effect of D_λ and n_{drag} on simulating the oxygen transport resistance most widely cited experimental measurements from the literature has been selected [20, 39, 40, 160, 100, 98, 62, 41]. Simulations were run at 300 kPa, 70°C and 90%RH and the corresponding oxygen transport resistance values are compared with experimental measurements as shown in figure 5.10

Figure 5.9 shows the simulation results of oxygen transport resistance with n_{drag} measurements from Fuller et. al.[39], Zawodzinski et. al. [160], Gottesfield et. al. [123], Ge et. al. [41] and Ise et. al. [62]. While studying the effect of n_{drag} , the values of D_λ was unchanged and the correlation by Zawodzinski et. al. [160] was used. The n_{drag} values from Fuller predicts early water condensation in the GDL while the correlation by Zawodzinski predicts the most delayed liquid water condensation in the GDL. The experimental measurements from Ise and Gottesfield agrees well with experimental results.

The effect of D_λ on simulation of oxygen transport resistance is shown in figure 5.9. For all D_λ sensitivity simulations, n_{drag} correlation for Zawodzinski was used. The D_λ values by reported by Caulk et al.[20], Motupally et al. [100] and Fuller et. al.[40] is much higher compared to Mittlesteadt[98] and Zawodzinski[160]. Due to this higher back diffusion water condensation in the GDL is delayed and the model predicts much lower oxygen transport resistance values compared to the

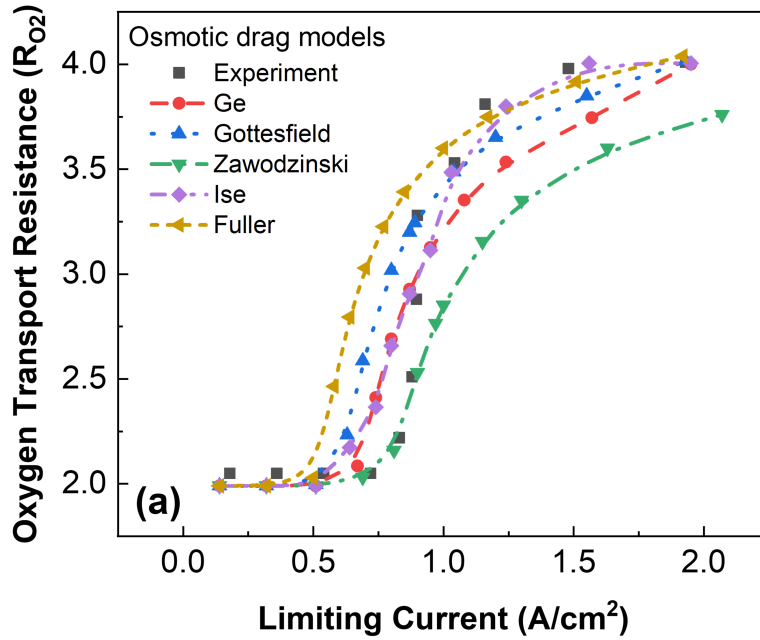


Figure 5.9: Simulation of Oxygen transport resistance with different values of electro-osmotic drag [39, 160, 123, 41, 62] reported on literature.

experiment. Model shows the best agreement with the experimental measurements Zawodzinski et. al. [160]. Compared n_{drag} the D_λ values vary much more significantly and as a result the model shows much higher sensitivity to D_λ .

5.4 Summary

A simplistic alternative to the Darcy law based two-phase water transport model is proposed based on the work by Caulk et al [22]. This simple model considers liquid water saturation to be constant and uniform whenever diffusion media is wet and provides a mathematical advantage of removing liquid water saturation as a state variable since liquid water saturation no longer varies when the diffusion media is wet. In addition, the newly developed 1-D model eliminates the need to specify the saturation boundary condition at the channel-diffusion media interface. The saturation dependent material transport properties (e.g relative permeability) is also not required to model water transport through the GDL since Darcy law is not utilized. To implement this model only the ratio of tortuosity over porosity

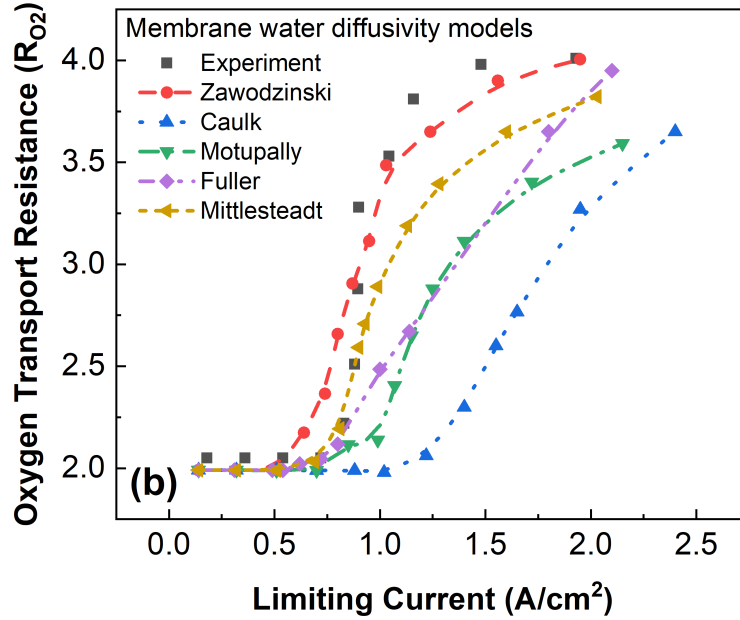


Figure 5.10: Simulation of Oxygen transport resistance with different values membrane water diffusivity [20, 40, 160, 100, 98] reported on literature.

(τ/ϵ) is required which can be very easily obtained from limiting current experiments. To capture the effects of liquid water flooding in the electrode, an empirical approach has been adopted. During liquid water condensation in the electrode the active sites are covered by liquid water and it reduces the catalyst utilization of the electrode. To calculate how catalyst utilization varies with local water activity polarization experiments were conducted at carefully designed wet operating conditions and the experimental results were fitted with 1-D simulation. It has been found that the correlation between catalyst utilization and electrode water activity exhibits a sigmoid function behavior. The roughness factor of the electrode rapidly declines after the onset water activity in the electrode. The newly developed 1-D model has been validated with both limiting current and polarization experiments. Wet limiting current and polarization experiments are conducted at 300kPa 70°C, 80% and 90%RH. It has been demonstrated with the inclusion of water tendril and catalyst utilization model, oxygen transport resistance and polarization test can be very accurately predicted at dry and wet operating conditions. Simulation results

showed liquid water coverage in the electrode can be as high as 75% under high humidity operating conditions.

Chapter 6

DEVELOPMENT OF DOWN-THE-CHANNEL MODEL

6.1 Down-the-Channel Framework

While the 1-D model discussed in chapter 4 and 5 can accurately predict PEMFC performance under both dry and wet operating conditions, the effect of flow-orientation, stoichiometric ratio, pressure drop and coolant temperature effect on cell performance cannot be captured. The 1-D model is limited to only high stoichiometric operations with minimal pressure drop. To overcome this limitation a 1+1-D model framework is developed based on the 1-D model.

In the 1+1-D model, the flow channel is discretized in multiple segments and the 1-D model is used a probe to calculate the cell conditions. Local pressure, temperature, RH and mole flux is provided to the 1-D model as an input and the cell voltage at each node is calculated. The input mole flux at each node is calculated based on mass conservation and discussed in 6.2. To solve for the cell voltage for an applied current density, the anode FF voltage is set to ground and the current density distribution is optimized to obtain an equipotential cathode FF. Since the bipolar plates are made of metals with high electronic conductivity the assumption of equipotential FF is reasonable for fuel cell applications. During co-flow operation the reactants flow in the same direction for both anode and cathode. For counter-flow operation anode flow direction is altered to the opposite to cathode flow direction. Coolant flow direction remains the same for both co-flow and counter flow. Figure 1 shows the schematic of the 1+1-D model for both co-flow and counter-flow orientation.

6.2 Channel discretization

Applying the conservation of mass equation on control volume z the oxygen ($N_{O_2}^z$) and water vapor molar flow rate ($N_{H_2O,C}^z$) is calculated as

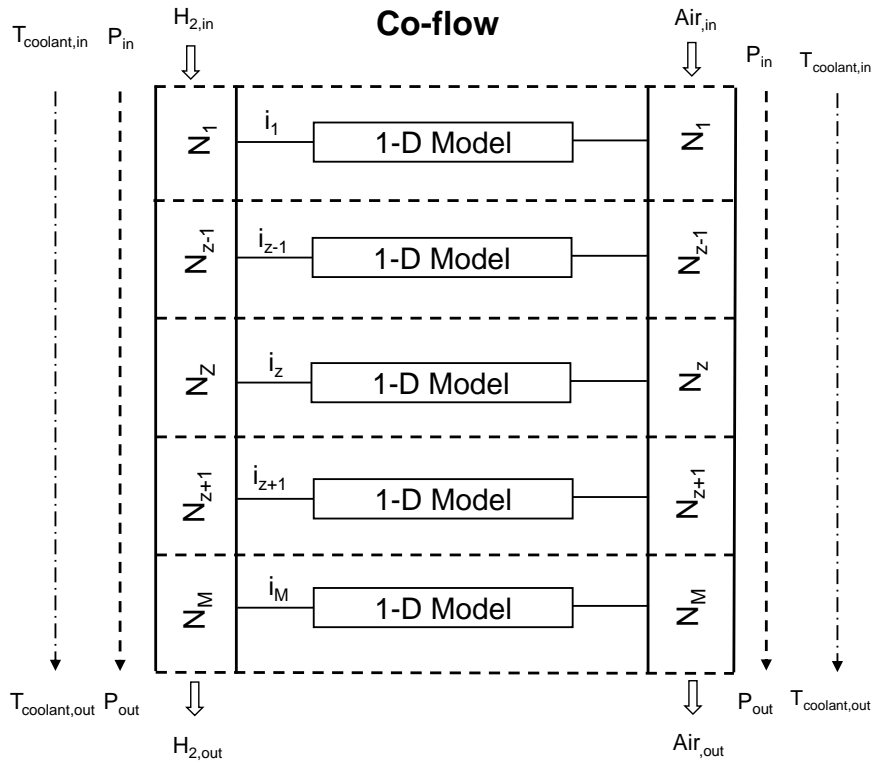


Figure 6.1: Implementation of co-flow orientation with the resistance network of the 1+1-D model where multiple 1-D cells are represented by electric circuits coupled with the gas flow in the flow-channels

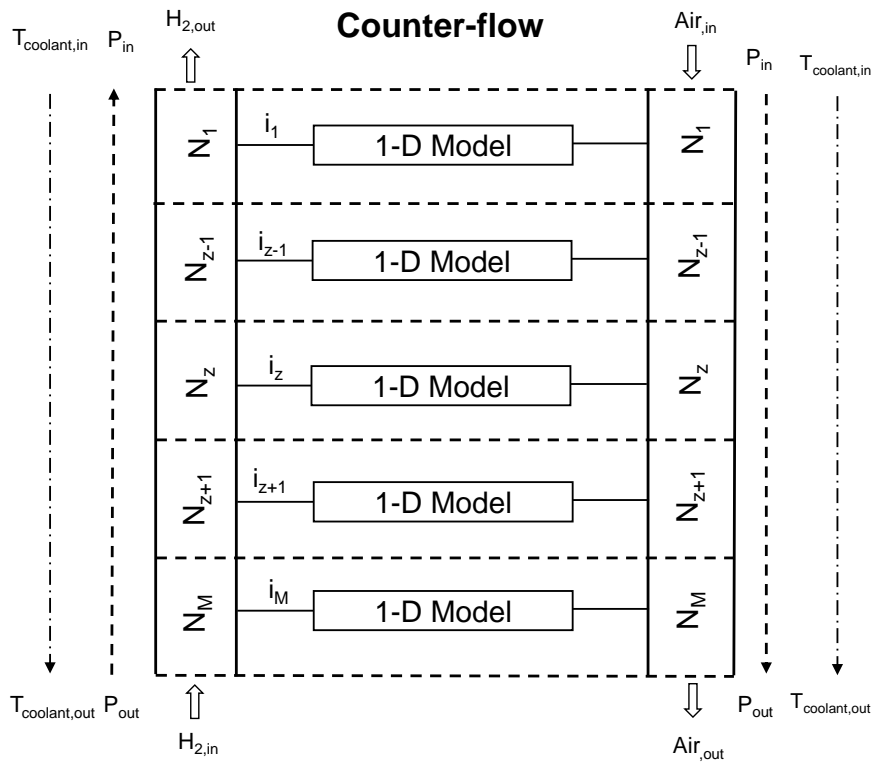


Figure 6.2: Counter-flow orientation implementation of the 1+1-D model where multiple 1-D cells are represented by electric circuits coupled with the gas flow in the flow-channels

$$N_{O_2}^z - N_{O_2}^{z-1} - \frac{i_{local}^{z-1}}{(M-1) \times 4F} = 0 \quad (6.1)$$

$$N_{H_2O,C}^z - N_{H_2O,C}^{z-1} + (1 - f_w^{z-1}) \frac{i_{local}^{z-1}}{(M-1) \times 2F} = 0 \quad (6.2)$$

Here M is the total number of nodes in flow channel, i_{local} is the local current density at node z , f_w is the fraction of generated water transferred to anode side from cathode side and F is the faraday's constant. Similarly the molar flow rate of hydrogen ($N_{H_2}^z$) and water vapor ($N_{H_2O,a}^z$) in anode side for control volume z can be obtained

$$N_{H_2}^z - N_{H_2}^{z-1} - \frac{i_{local}^{z-1}}{(M-1) \times 2F} = 0 \quad (6.3)$$

$$N_{H_2O,a}^z - N_{H_2O,a}^{z-1} - f_w^{z-1} \frac{i_{local}^{z-1}}{(M-1) \times 2F} = 0 \quad (6.4)$$

At the Cathode inlet, the water vapor mole fraction $X_{H_2O,c}^{in}$ is calculated based on the inlet RH ($RH_{c,in}$) and total inlet pressure, (P_{in})

$$X_{H_2O,C}^{in} = \frac{P_{H_2O,C}}{P_{in}} = \frac{RH_{c,in} \times P_{sat}(T_{coolant,in})}{P_{in,cathode}} \quad (6.5)$$

Here the saturation pressure P_{sat} is calculated based on the coolant inlet temperature. Oxygen mole fraction ($X_{O_2}^{in}$) is obtained as

$$X_{O_2}^{in} = \frac{P_{O_2}^{in}}{P_{in,cathode}} = \frac{X_{O_2,dry} (P_{in} - RH_{c,in} \times P_{sat}(T_{coolant,in}))}{P_{in,cathode}} \quad (6.6)$$

The inlet molar flux rate is a function of stoichiometric ratio and it is calculated as,

$$N_{O_2}^{in} = St \times \frac{i_{applied}}{4F} \quad (6.7)$$

Water vapor ($N_{H_2O,c}^{in}$) and nitrogen mole fraction ($N_{N_2}^{in}$) are obtained following the ideal gas law,

$$N_{H_2O,c}^{in} = N_{O_2}^{in} \times \frac{X_{H_2O,C}^{in}}{X_{O_2}^{in}} \quad (6.8)$$

$$N_{N_2}^{in} = N_{O_2}^{in} \frac{X_{N_2}^{in}}{X_{O_2}^{in}} \quad (6.9)$$

Similarly, the inlet mole fractions of hydrogen ($X_{H_2}^{in}$) and water ($X_{H_2O,a}^{in}$) in anode side are calculated as.

$$X_{H_2}^{in} = \frac{P_{H_2}}{P_{in,anode}} = \frac{P_{in} - RH_{in}^a \times P_{sat}(T_{coolant,in})}{P_{in}} \quad (6.10)$$

$$X_{H_2O,a}^{in} = \frac{P_{H_2O,a}}{P_{in}} = \frac{RH_a^{in} \times P_{sat}(T_{coolant,in})}{P_{in,anode}} \quad (6.11)$$

Here, RH_a^{in} refers to the inlet relative humidity, $P_{in,anode}$ is the inlet pressure for anode.

6.3 Results: Down-the-Channel Model

6.3.1 Experimental validation

The developed 1+1-D down-the-channel model is validated with steady state experimental results conducted by General Motors on a PEMFC stack. Simulation results at 1.50 A/cm² is shown in figure 6.5. The measured value of HFR is compared simulation predicted results. A HFR of 0.608 $\Omega - cm^2$ is predicted by the simulation where the experimentally measured value was 0.610 $\Omega - cm^2$. The comparison between experimentally measured and simulation predicted current density distribution along the flow channel which is plotted in figure 6.5 and good agreement is found in the current density distribution with slight deviations near the end of the flow channel.

6.3.2 Effect of Stoichiometry and Flow-orientation on PEMFC performance

To investigate the effect of stoichiometry and flow-orientation simulations were carried out at stoichiometries of 2.0 and 1.0 for both dry (150 kPa, 80°C, 20%RH) and wet (150 kPa, 80°C, 100%RH) operating conditions. As shown in figure 6.6(a), cell performance under extreme dry condition is sensitive to both stoichiometric flow rate and flow-orientation. At extreme dry conditions low stoichiometry performance is higher than high stoichiometry and flow orientation does

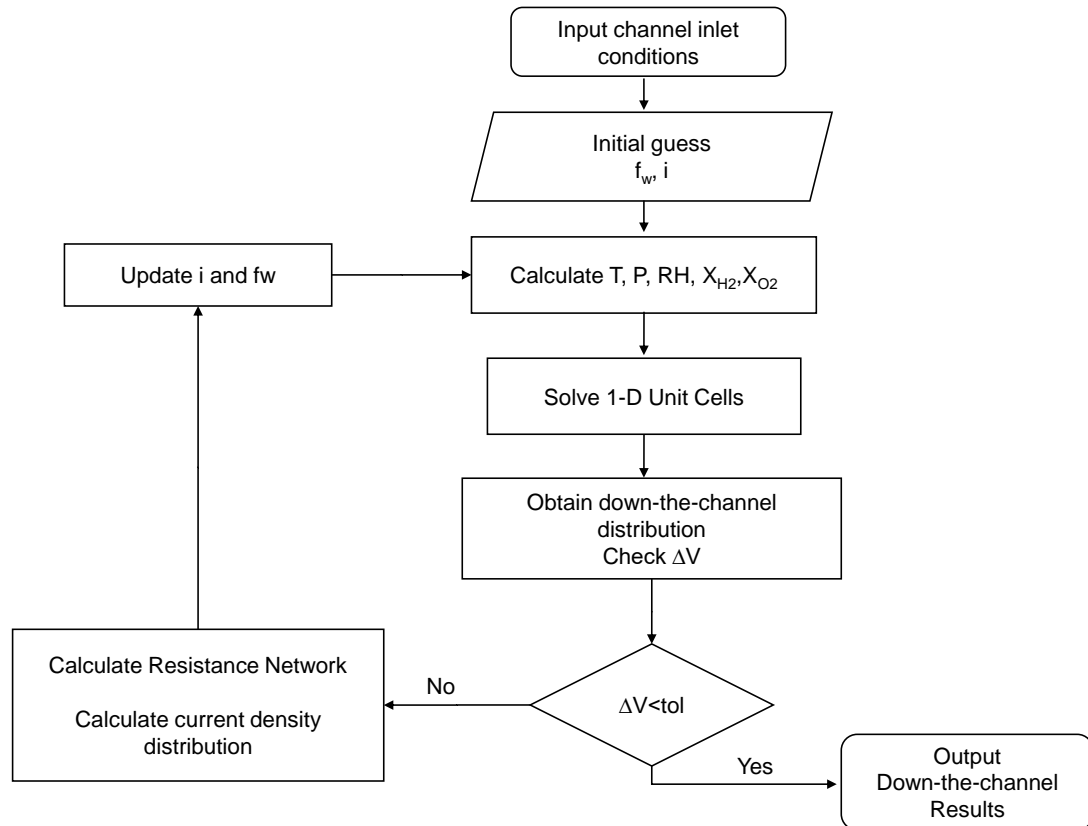


Figure 6.3: Solution algorithm for obtaining equipotential cathode BP and current density distribution in the down-the-channel model.

```

while (dV>tolerance)
    Vmax =max[V(z)]   Vmin =min[V(z)]
    V =  $\frac{\sum V(z)}{N-1}$ 
    dV = Vmax - Vmin
    Rtotal(z) = RHOR(z) + RORR(z) + Rohmic(z) + Rmass(z)
    if dV < tolerance
        break
    else
        cd(z) = cd(z) +  $\frac{V(z)-V}{R_{total}(z)} \times \text{relaxation}$ 
    end
    cdsum =  $\frac{\sum_{i=1}^N cd(z)}{N-1}$ 
    cd(z) = iinput ×  $\frac{cd(z)}{cd_{sum}}$ 
end

```

Figure 6.4: Pseudo code showing the algorithm for obtaining equipotential cathode bipolar plate

not have any noticeable effect on cell performance. For stoichiometry ratio of 2, counter-flow performance is much higher compared to co-flow. The performance gain for counter-flow operation is mostly from the lower HFR values. High stoichiometric flows have a drying effect on the cell which is detrimental to cell performance under extreme condition.

The cell performance with varying stoichiometry and flow-rates under wet operating (150 kPa, 80°C, 100%RH) condition is plotted in figure 6.6(b). Under wet operating condition cell performance is not sensitive to flow-orientation but stoichiometric ratio has a much more noticeable effect. Since inlet gas feed is fully humidified HFR values are almost identical for all cases. But we observe a higher mass transport losses at high current density due to liquid water condensation and it is more pronounced at low stoichiometry condition.

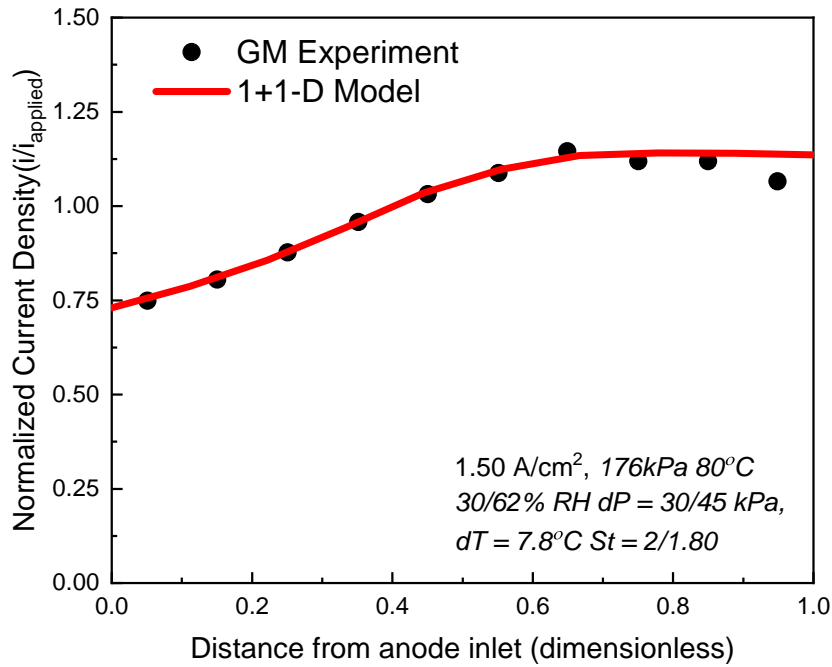


Figure 6.5: Down-the-channel current distribution experiment and model predictions at 1.50 A/cm^2 current density and counter-flow orientation. Operating condition 176 kPa $30/60\% \text{RH}$ 80°C , Pressure drop $30/45 \text{ kPa}$, Coolant temperature difference 7.8°C

6.3.3 Down-the-channel distribution

To investigate the effect of stoichiometric ratio and flow-orientation on down-the-channel distribution of critical performance parameters simulations were run at 1.5 A/cm^2 under both dry (150 kPa 80°C , $20\% \text{RH}$) and wet (150 kPa 80°C , $100\% \text{RH}$) operating condition. The channel pressure drop was kept at $30/45 \text{ kPa}$ and coolant temperature difference was kept constant at 7.8°C .

At high stoichiometric flow rates current density distribution remains uniform through-out the channel length which is desirable but at low stoichiometry condition current density show high gradient between inlet to outlet locations. Current density distribution for co-flow orientation shows more than 20% variation between the local minima and maxima where counter flow shows only 6% variation. The simulation

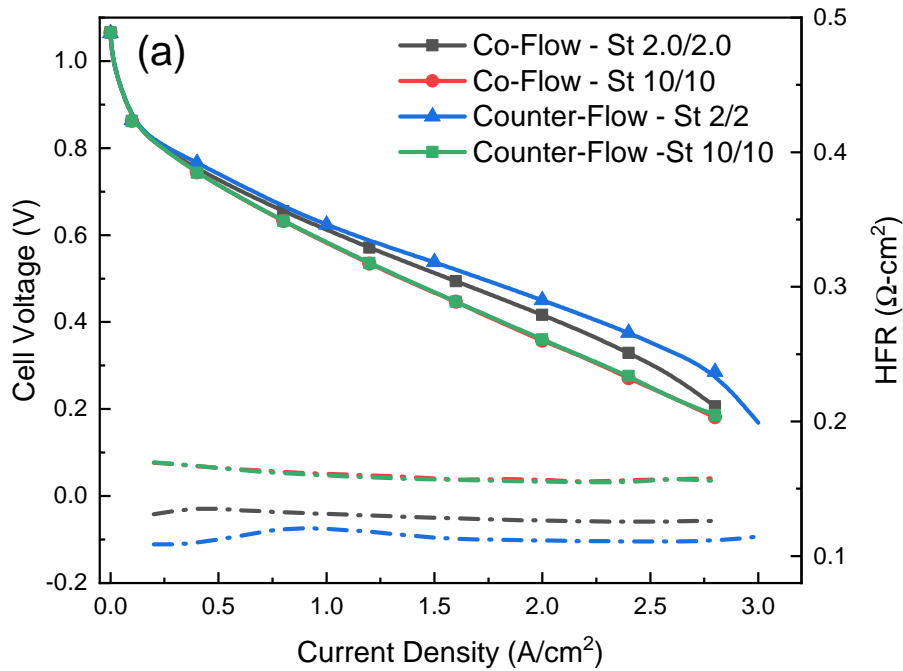


Figure 6.6: 1+1-D simulation result showing the effect of stoichiometric flow rate on PEMFC under dry operating conditions with co-flow and counter-flow orientation. Operating condition: 150 kPa 80°C, 20% RH (Dry), 100%RH (Wet), Pressure drop 30/45 kPa, Coolant temperature difference 7.8°C

results indicate more uniform current density is achieved for counter-flow at low stoichiometry.

The fraction of generated water transported from cathode side to anode side (f_w) is plotted in figure 6.9(a). At high stoichiometric flow rates water transport across the membrane is less than 5%. However at low stoichiometry water transport across membrane becomes more prominent. For co-flow, f_w shows a gradual increase from cathode inlet to exit with values of f_w less than 5% near cathode inlet and 20% near the cathode exit. For counter-flow operation, f_w shows a completely different trend. f_w is highest near the cathode inlet and becomes negative near cathode exit which essentially shows water is transported towards the cathode from anode. This phenomenon is referred as internal circulation of water as the water that is

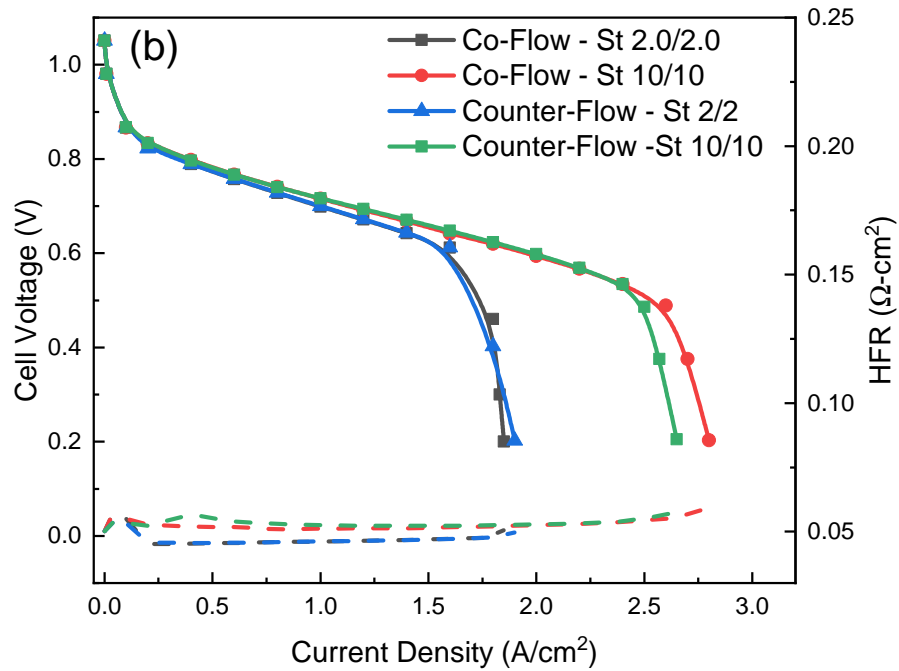


Figure 6.7: 1+1-D simulation result showing the effect of stoichiometric flow rate on PEMFC under wet operating conditions with co-flow and counter-flow orientation. Operating condition: 150 kPa 80°C, 20% RH (Dry), 100%RH (Wet), Pressure drop 30/45 kPa, Coolant temperature difference 7.8°C

transported to anode is dragged back to the cathode side. The effect of internal water circulation can be observed in the HFR distribution as shown in figure 6.9(b). HFR values are significantly reduced at low stoichiometric flow rates regardless of the flow orientation but counter-flow shows a more uniform and low HFR. However, for co-flow orientation HFR shows a steep decrease from inlet to exit.

The anode and cathode channel relative humidity distribution in down-the-channel direction for co-flow and counter-flow is plotted in figure 6.10(a) and 6.10(b) respectively. RH in both anode and cathode channel is increased as lower stoichiometric flow rates are used. For co-flow orientation (figure 6.10(a)), both anode and cathode gas flow is in the same direction. Relative humidity gradually increases towards the channel exit as a result for co-flow orientation the cell remains more

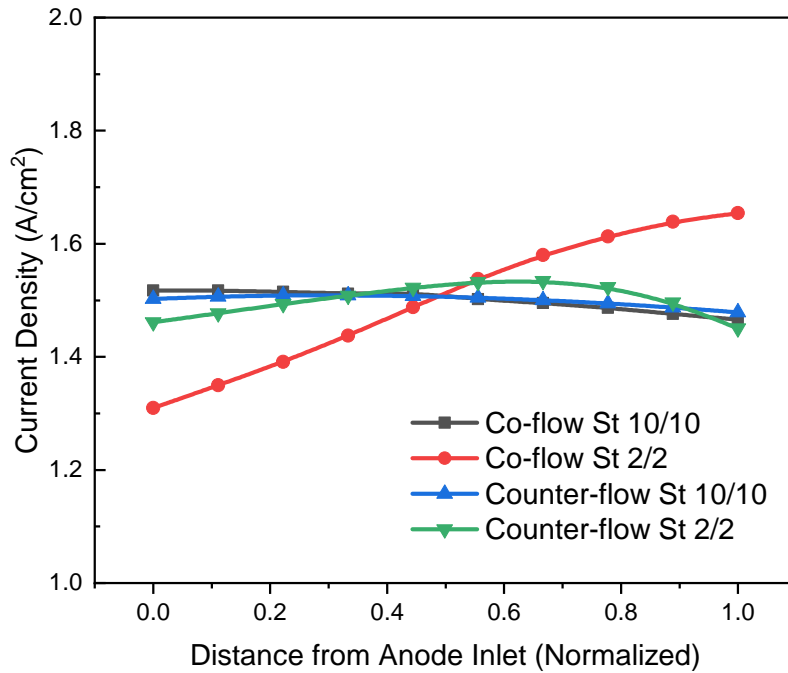


Figure 6.8: Down-the-channel current distribution at 1.50 A/cm^2 applied current density and counter-flow orientation. Operating condition 150 kPa 20/20%RH 80°C , Pressure drop 30/45 kPa, Coolant temperature difference 7.8°C

humidified near the channel exit. Cathode RH is higher than anode all through the channel since water generation is in the cathode side. For counter-flow orientation, the flow direction for anode is changed. Even though, the general trend of increasing RH near the channel exit remains the same but because of the opposite flow direction overall humidification level of the cell is more improved in co-flow orientation.

6.4 Investigation of water balance

For all the simulations in this section, the base line operating condition is 150kPa 80°C and 20/20% (An/Ca) RH with 30/45kPa pressure drop and 7.8°C coolant temperature rise. 130/130 μm GDL and 25 μm membrane has been used as the base-line geometry for all simulations.

6.4.1 Asymmetric GDL

Figure 6.11 shows the distribution of cathode to anode water transport (f_w) in down-the-channel direction for counter-flow operation at 1.5 A/cm², 150 kPa 80°C, 20% RH. It can be observed that assembling cells with different anode/cathode GDL thickness can significantly alter water transport across the membrane. For example, increasing GDL thickness in cathode side leads to higher values f_w whereas anode GDL thickness have a very negligible effect. Since the water diffusivity in hydrogen is four times higher than water diffusivity in air, increasing GDL thickness in anode side does not significantly increase the transport resistance and as a result f_w is not as sensitive to anode GDL thickness as the cathode counterpart. The cell with 230/130 μm GDL, shows highest water transport and this leads to a higher membrane water uptake as shown in figure 6.12(a). Membrane hydration is extremely critical under dry operating conditions since PEMFC performance is primarily limited by ohmic loss at automotive fuel cell operating condition (0.67V) as per DOE guideline. A thicker cathode GDL decreases the membrane ohmic resistance (HFR) by providing better membrane humidification. the author would like point out that that increasing GDL thickness will also increase the oxygen transport resistance which may lead to higher mass transport losses at high current densities. Hence, the balance between mass transport loss and ohmic loss must be taken into consideration.

6.4.2 Membrane thickness

It is well understood in literature that lowering membrane thickness reduces the proton transport loss in membrane. In this section, simulation results of cells with 25, 15 and 10 μm membrane thickness is compared to study the effect of membrane thickness on cell water balance, water uptake (λ) and channel RH distribution. 1+1-D simulation results of HFR and membrane water uptake (λ) are shown in figure 6.13. Consistent with the existing literature it is observed from figure 6.13(b) that lowering membrane thickness reduces the HFR. However, it is important to note that membrane water uptake (λ) also improves with thinner membranes as shown in figure 6.13(a). The cell with 25 μm membrane shows high water uptake (λ) gradient between channel inlet to exit which is known to have detrimental effect on membrane degradation whereas the cell with 10 μm membrane exhibits

a higher and more uniform water uptake (λ) distribution which both improves cell performance and membrane degradation. Figure 6.14(a) shows the water transport from cathode anode in the down-the-channel direction for cells with 25, 15 and 10 μm membrane thickness. Thinner membranes transport more water towards cathode compared to the thicker membrane. Water back diffuses from anode to cathode because of the water gradient between the two sides and a thinner membrane leads to lower back diffusion resistance resulting in more water transport towards anode side. Higher water transport (f_w) also improves the anode RH as shown in figure 6.14 (b). The channel RH distribution shows equal anode and cathode RH levels are achieved near the middle of the channel length when a 10 μm membrane is used which explains the uniform water uptake (λ) distribution.

6.4.3 Asymmetric channel inlet RH

To study the effect of relative humidity of channel inlet, simulations were run at 60/20, 20/20 and 20/60% (An/Ca) inlet RH conditions. The operating pressure and temperature was kept constant at 150 kPa and 80°C respectively. For all the simulations 130/130 μm GDL and 25 μm membrane was used.

In figure 6.15(a) water uptake (λ) distribution is plotted for the aforementioned conditions. 20/60% RH case shows the highest membrane water uptake whereas 20/20 %RH shows the lowest membrane water uptake. HFR values from 6.15(b) also follows the same trend as membrane conductivity is directly correlated with water uptake (f_w). 20/60% RH case shows the lowest HFR and 20/20%RH case shows the highest HFR distribution in down-the-channel direction. The reason for lower HFR values or higher water uptake values for 20/60% RH case can be understood from the water balance and channel RH distributions in figure 6.16(a) and (b) respectively. Higher RH in cathode side transports more water to anode as back-diffusion becomes the dominant driving force and because of the higher water transport across membrane anode side remains more humidified. High anode RH does not improve membrane humidification as much as water transport from anode side to cathode side depends primarily on electro-osmotic drag which is a function of ionic potential difference across the membrane. To summarize, asymmetric RH can help reduce the membrane proton transport resistance when higher cathode RH values are utilized.

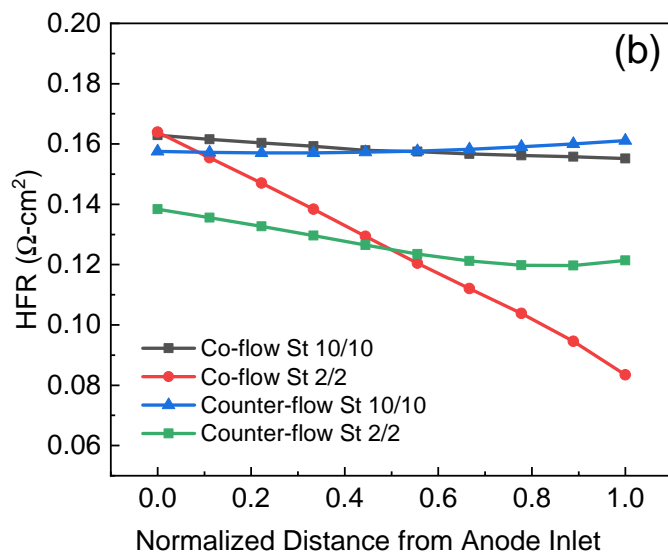
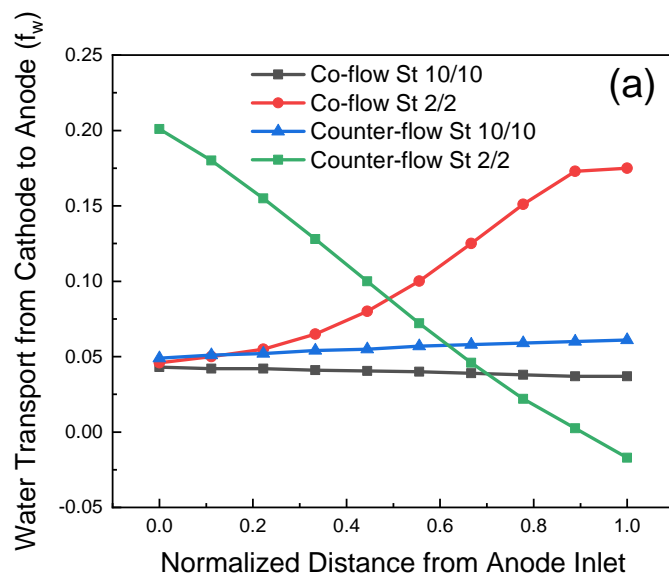


Figure 6.9: Down-the-channel distribution of (a) water transport from cathode to anode (b) HFR at co-flow and counter-flow orientation for stoichiometric flow rates of 2 and 10. Operation conditions: 150 kPa 80°C 20% RH.

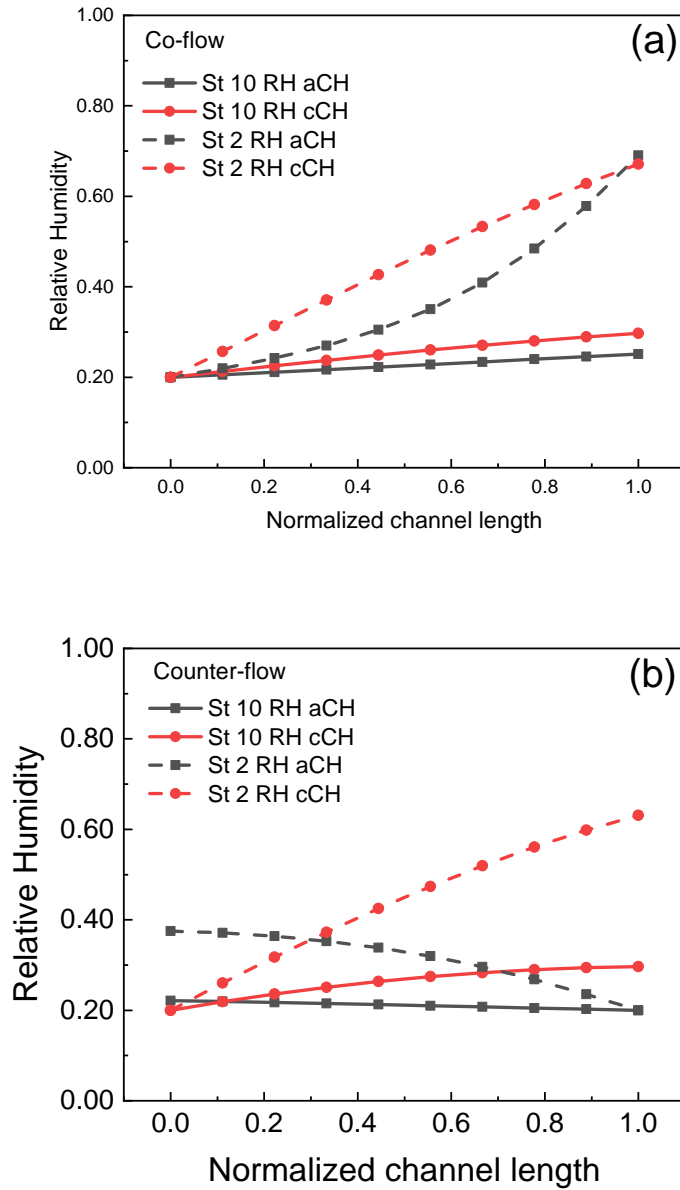


Figure 6.10: Relative humidity distribution in down-the-channel direction at stoich of 10 and 2 for (a) co-flow orientation (b) counter-flow orientation. Operation conditions: 150 kPa 80°C 20% RH.

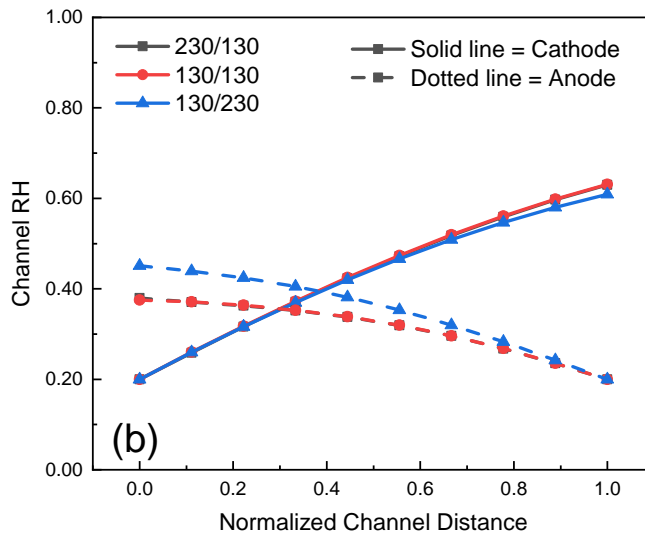
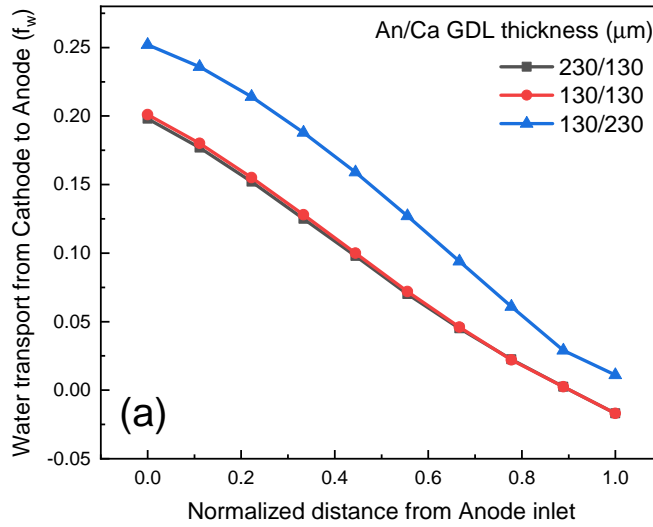


Figure 6.11: Down-the-channel distribution of (a) cathode to anode water transport (b) channel relative humidity with varying anode/cathode GDL thickness at 150 kPa 80°C, 20% RH

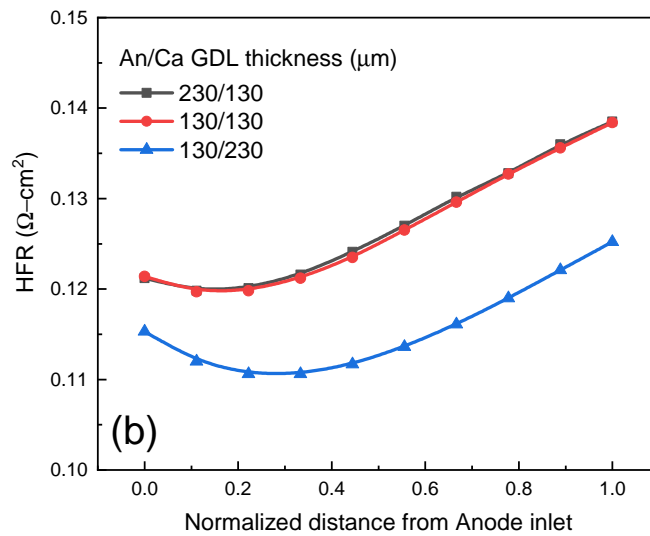
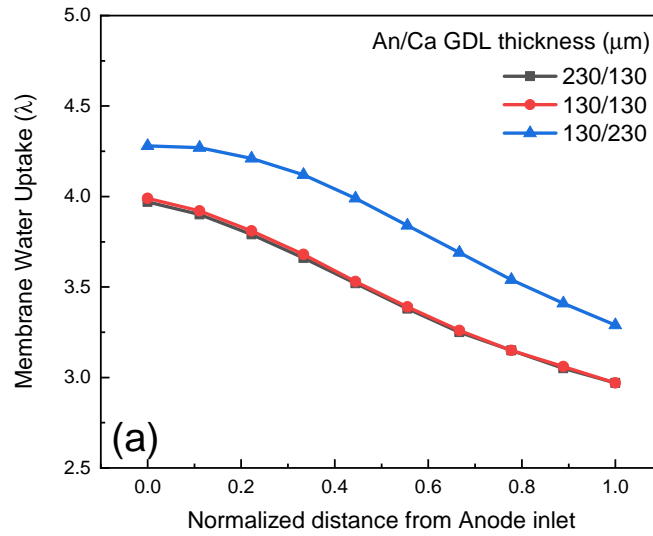


Figure 6.12: Effect of GDL thickness on along the-channel distribution of (a) membrane water uptake (b) HFR distribution at at 150 kPa 80°C, 20% RH

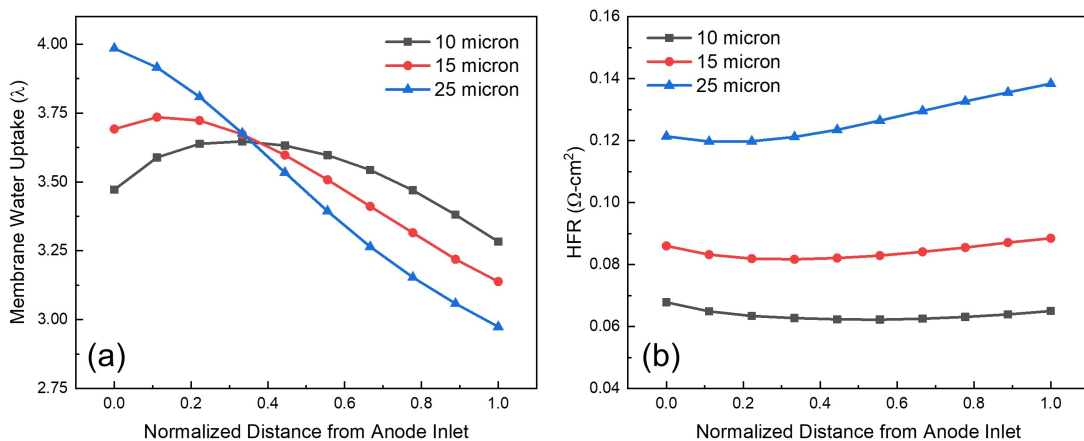


Figure 6.13: Effect of membrane thickness on along-the-channel distribution of (a) membrane water uptake (b) HFR distribution at at 150 kPa 80°C, 20% RH

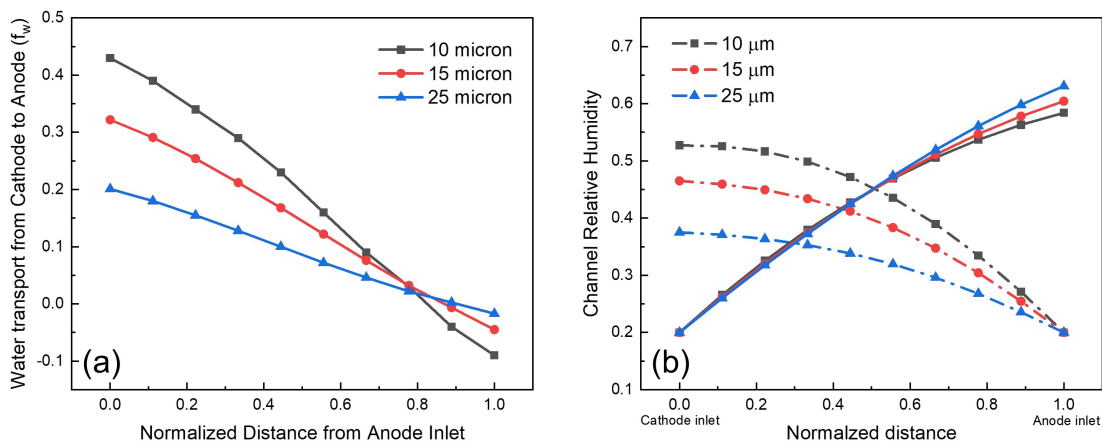


Figure 6.14: Down-the-channel distribution of (a) cathode to anode water transport (b) channel relative humidity with varying membrane thickness at 150 kPa 80°C, 20% RH

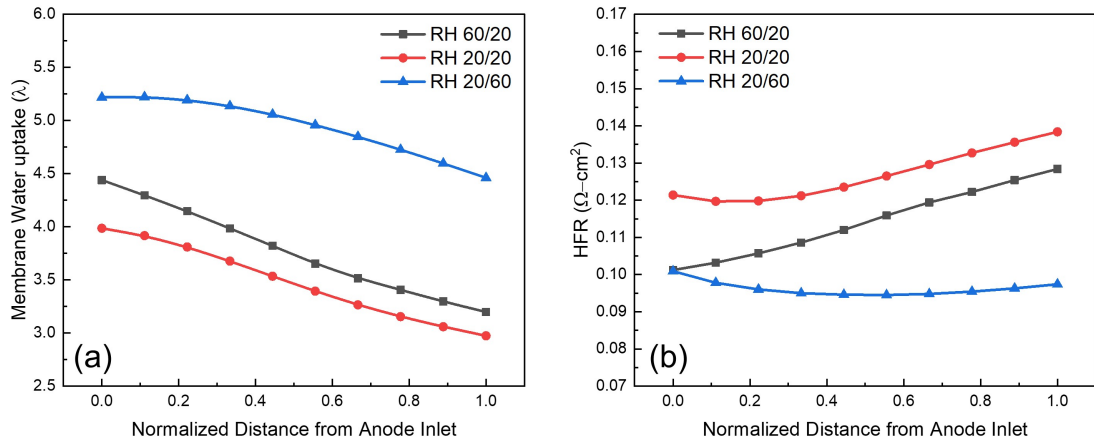


Figure 6.15: Effect of asymmetric channel inlet RH on (a) membrane water uptake (λ) (b) membrane proton transport resistance (HFR) at at 150 kPa 80°C, 20% RH

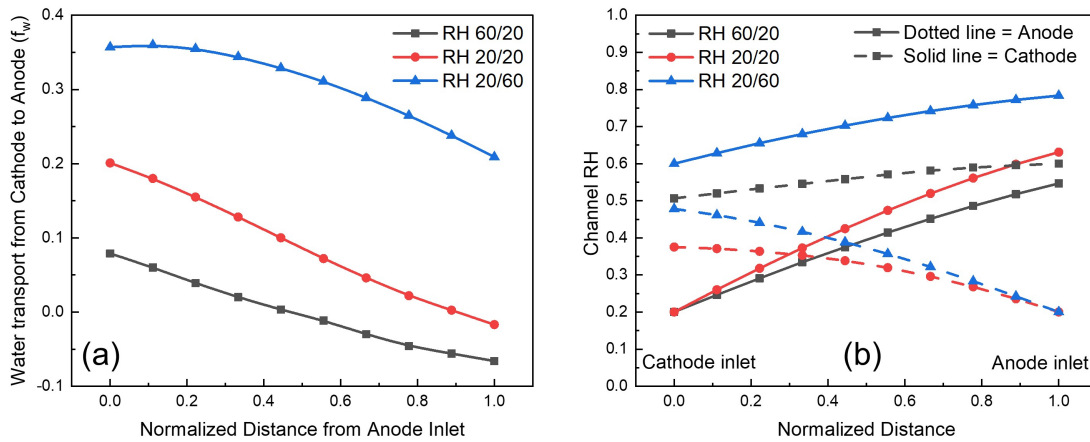


Figure 6.16: Effect of asymmetric channel inlet RH on (a) water transport from cathode to anode (f_w) (b) RH distribution in the down-the-channel direction at at 150 kPa 80°C, 20% RH

Chapter 7

CONCLUSION

In this thesis, a comprehensive down-the-channel performance model is presented. To formulate the down-the-channel model at first a 1-D dry model is developed. The 1-D model assumes fully developed flow in the flow channels and a constant reactant concentration in the flow-channel GDL interface. The pressure in the modeling domain is considered as isobaric. For mass transport in the gas diffusion layer and micro porous layer, diffusion is considered as the only transport mechanism. Both Fickian and Non-Fickian diffusion is included in transport resistance but the pressure independent Non-Fickian diffusion terms like Knudsen diffusion are lumped into a constant resistance parameter term in the transport equations, R_{others} is obtained experimentally. Anisotropic diffusion in the gas diffusion media is modeled with a correction factor f_{geo} . Homogeneous and isotropic properties for porosity, tortuosity and thermal conductivity are assumed throughout the spatial domain. The 1-D dry model considers non-isothermal heat transfer, convective and diffusive gas transport, electrochemical re-action, shorting and cross over current, effects of land/channel geometry, membrane water balance, and proton resistance based on non-linear water content in the membrane. Limiting current experiments were conducted at 115.8 kPa, 151.34 kPa, 201.34 kPa and 301.34 kPa, at 80°C and 64% relative humidity. A dry polarization test was conducted at 70°C, 100 kPa and 60% relative humidity. Non-pressure dependent resistance and the ratio of porosity to tortuosity are obtained from the limiting current experiment to use in the model. Results from the 1-D model simulation have been compared with both limiting current and dry polarization tests. Detailed discussion on incorporating water balance, heat transfer and mass transport have been presented in chapter 4. It has been demonstrated that at high current densities the membrane water content distribution becomes highly non-linear so modeling ohmic resistance with

constant membrane conductivity or linear water content yields inaccurate result. In addition, inclusion of a non-isothermal temperature distribution inside the PEMFC sandwich is also important since a temperature gradient of 5-6 degrees exist at the high current density region. For modeling mass transport in a 1-D model, inclusion of “ f_{geo} ” factor is also crucial. “ f_{geo} ” accounts for land/channel geometry and anisotropic diffusion coefficients. The main objective of the 1-D modeling framework is to accurately predict PEMFC physics at dry operating condition and it has been achieved successfully.

In addition, an application of the 1-D model also has been presented where the effect of coupled heat and mass transport on water condensation in GDL is studied. Two of the most widely used commercial gas diffusion materials, the Toray TGP-H-060 and Freudenberg H23C8, were selected for this case study due to their difference in thermal properties. The through-plane thermal conductivity of Toray material is one order of magnitude higher than that of the Freudenberg material. Limiting current experiments were conducted to determine oxygen transport resistance under both dry and wet operating conditions. The Toray material shows a sharp increase in oxygen transport resistance after the onset of water condensation, while Freudenberg material exhibits a gradual increase. The polarization curves under dry and wet conditions agreed with the effect of thermal and oxygen transport properties. Toray performs better under dry conditions, but worse under wet conditions. 1-D modeling analysis showed the performance variation is due the differences in thermal conductivity and gas diffusivity properties . A critical controlling parameter, $k \left(\frac{\tau}{\varepsilon} \right)$, has been obtained from the 1-D coupled heat and water vapor transport equations. A gas diffusion material with high $k \left(\frac{\tau}{\varepsilon} \right)$ performs well under hot and dry conditions, but suffers from drastic oxygen transport loss as soon as liquid water condensation occurs in the GDL. On the other hand, a gas diffusion material with low $k \left(\frac{\tau}{\varepsilon} \right)$ is more suitable for cold and wet operating conditions. Therefore, there exists an optimal material design that yields an intermediate $k \left(\frac{\tau}{\varepsilon} \right)$ value, which allows the material to have robust performance across a broad range of operating conditions. The findings of this case study provide clear guidelines for designing PEMFC materials to significant boost fuel cell energy conversion efficiency for future application.

Next, to expand the models capability to predict PEMFC performance at

high humidity operation two-phase water transport has been implemented. A simplistic alternative to the Darcy law based two-phase water transport model is proposed based on the work by Caulk et al [22]. This simple model considers liquid water saturation to be constant and uniform whenever diffusion media is wet and provides a mathematical advantage of removing liquid water saturation as a state variable since liquid water saturation no longer varies when the diffusion media is wet. In addition, the newly developed 1-D model eliminates the need to specify the saturation boundary condition at the channel-diffusion media interface. The saturation dependent material transport properties (e.g relative permeability) is also not required to model water transport through the GDL since Darcy law is not utilized. To implement this model only the ratio of tortuosity over porosity (τ/ϵ) is required which can be very easily obtained from limiting current experiments. To capture the effects of liquid water flooding in the electrode, an empirical approach has been adopted. During liquid water condensation in the electrode the active sites are covered by liquid water and it reduces the catalyst utilization of the electrode. To calculate how catalyst utilization varies with local water activity polarization experiments were conducted at carefully designed wet operating conditions and the experimental results were fitted with 1-D simulation. It has been found that the correlation between catalyst utilization and electrode water activity exhibits a sigmoid function behavior. The roughness factor of the electrode rapidly declines after the onset water activity in the electrode. The newly developed 1-D model has been validated with both limiting current and polarization experiments. Wet limiting current and polarization experiments are conducted at 300kPa 70°C, 80% and 90%RH. It has been demonstrated with the inclusion of water tendril and catalyst utilization model, oxygen transport resistance and polarization test can be very accurately predicted at dry and wet operating conditions. Simulation results showed liquid water coverage in the electrode can be as high as 75% under high humidity operating conditions.

Finally the 1-D two phase model is extended to a 1+1-D down-the-channel model where the flow-channel was discretized in multiple segments using the mass conservation principle. Local channel information such as the pressure, temperature, RH, gas composition is provided as input to the 1-D model and cell voltage at each segment was calculated. To solve for the cell voltage at an applied current

density the anode flowfield was set to ground and the current density distribution was iterated to obtain an equipotential cathode. Co-flow and counter-flow orientation was achieved by switching the direction of anode flow. Coolant flow direction was kept the same regardless of flow orientation. The 1+1-D model has been validated with experimental current density distribution measured by General Motors and the model shows excellent agreement. 1+1-D simulations were run under dry (150kPa 80°C, 20%RH) and wet (150kPa 80°C, 100%RH) operating conditions with both co-flow and counter-flow. The channel pressure drop was kept constant at 30/45 kPa and coolant temperature gradient was maintained at 7.8 °C. The effect of flow orientation did not show any significant impact under wet or high stoichiometric flow rates. However, counter-flow operation showed improved performance at low humidity and low stoichiometric flow rates. Simulation results showed Counter flow operation provided more uniform current density distribution, enabled internal water circulation and lowered the membrane ohmic resistance.

Chapter 8

FUTURE WORK

The developed down-the-channel model opens a lot of research opportunities to move the current research forward. A summary of potential model improvements are listed below.

1. Improving model convergence at stoichiometry flow rates lower than 1.50 with high coolant temperature gradient and counter flow orientation.
2. Option to change coolant flow direction should be added.
3. The current iterative algorithm for membrane water balance exhibits ill-convergence and increases computation time. Developing a more robust membrane water balance algorithm is necessary to further improve the model.
4. Currently performance losses from the catalyst layer flooding and mass transport are based on empirical correlation. To further improve the model a catalyst layer agglomerate model with liquid water condensation effects should be added.
5. 1+1-D models capability to predict PEMFC performance straight and serpentine flow channel designs needs to be validated with experimental results.
6. Current water tendril model can capture the oxygen transport resistance for Toray type diffusion media (high thermal conductivity and low gas transport resistance). A mathematical formulation should be implemented to predict the oxygen transport resistance for Freudenberg type diffusion media (low thermal conductivity and high gas transport resistance)

7. Current 1-D model assumes the heat source to be localized in the cathode catalyst layer. The local heat generation effects such as: ohmic heating, reaction impossibilities needs to be accounted.

APPENDIX A

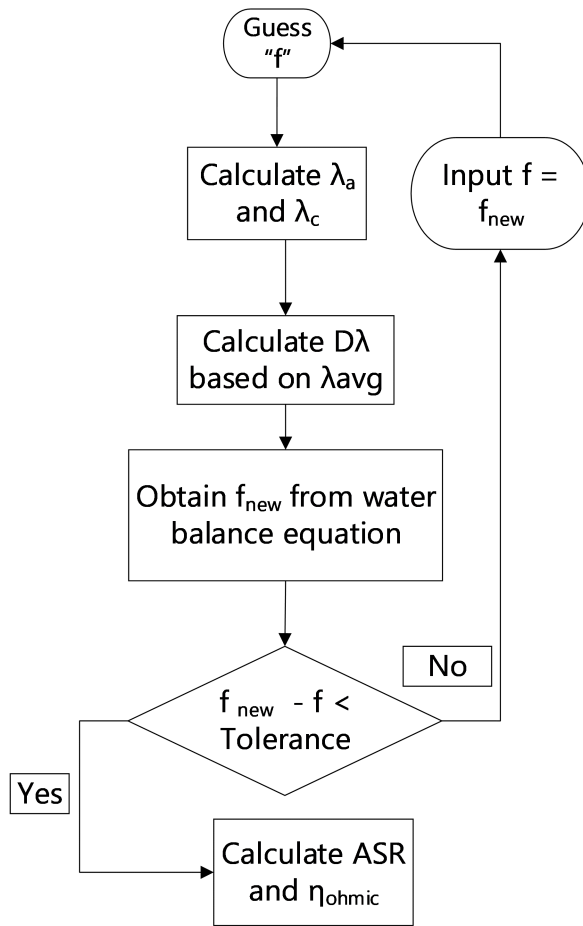


Figure A.1: Iteration loops for calculating fraction of generated water transported towards anode side from cathode side

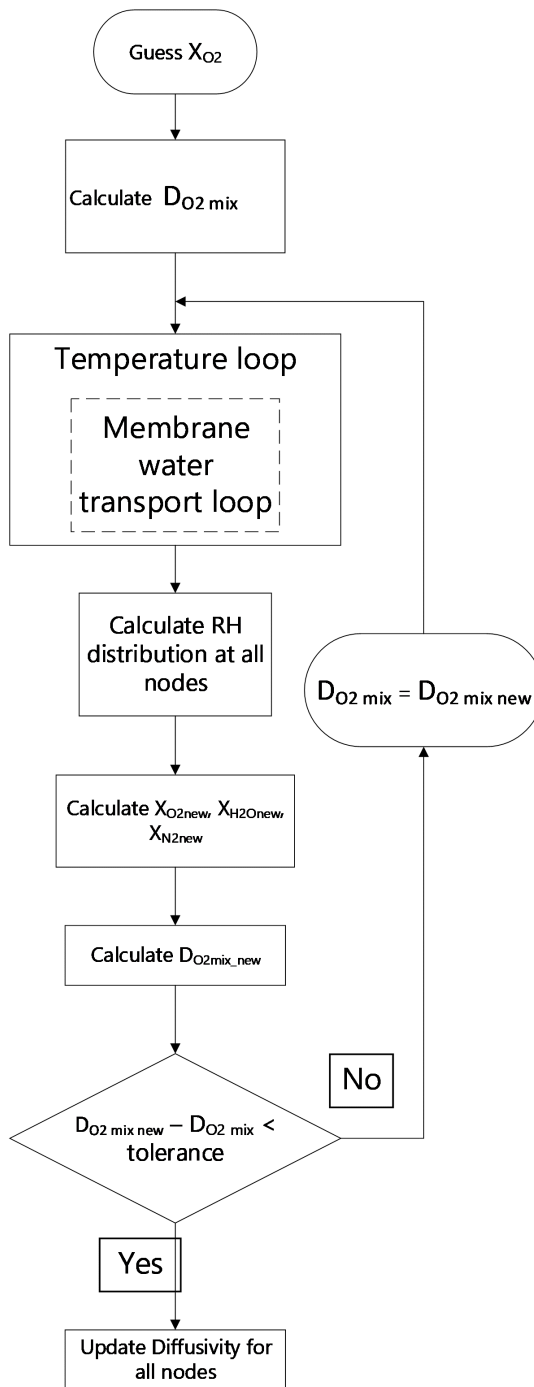


Figure A.2: Iteration loops for solving 1-D heat equation

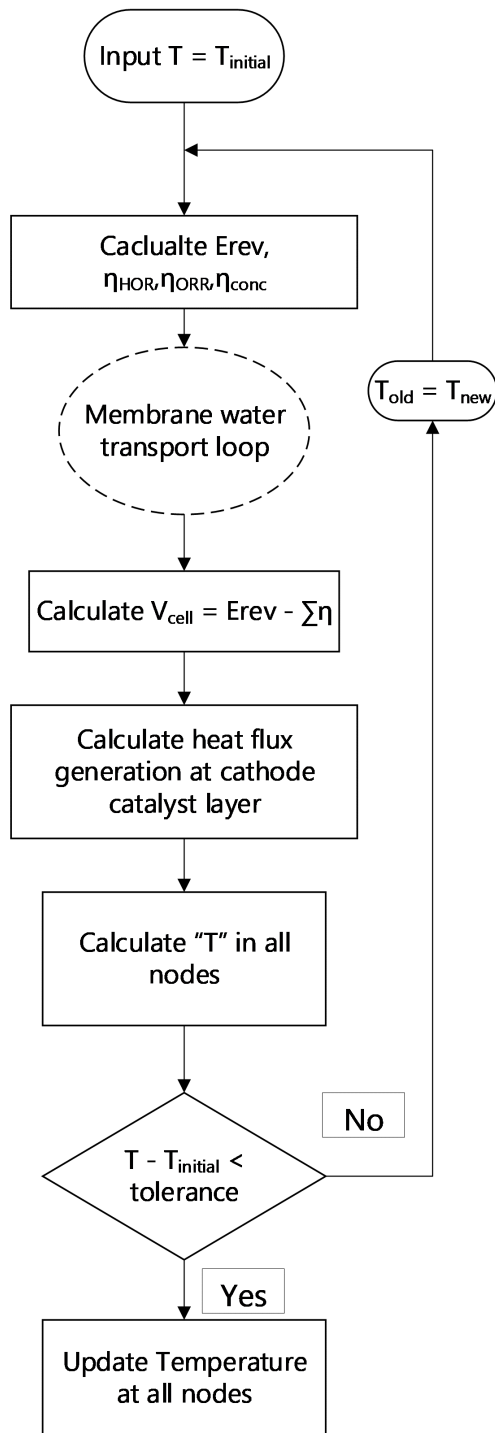


Figure A.3: Iteration loop for solving 1-D mass conservation equation

Bibliography

- [1] Z. Abdin, C.J. Webb, and E.MacA. Gray. “PEM fuel cell model and simulation in Matlab–Simulink based on physical parameters”. In: *Energy* 116 (Dec. 2016), pp. 1131–1144.
- [2] M Acosta et al. “Modeling non-isothermal two-phase multicomponent flow in the cathode of PEM fuel cells”. In: *Journal of power sources* 159.2 (2006), pp. 1123–1141.
- [3] United States Environmental Protection Agency. “State CO2 Emissions from Fossil Fuel Combustion”. In: (2018).
- [4] Ibrahim Alaefour et al. “The role of flow-field layout on the conditioning of a proton exchange membrane fuel cell”. In: *Fuel* 230 (2018), pp. 98–103.
- [5] J. C. Amphlett. “Performance Modeling of the Ballard Mark IV Solid Polymer Electrolyte Fuel Cell”. In: *Journal of The Electrochemical Society* 142.1 (1995), p. 1.
- [6] J.C. Amphlett et al. “A model predicting transient responses of proton exchange membrane fuel cells”. In: *Journal of Power Sources* 61.1 (1996), pp. 183–188. ISSN: 0378-7753.
- [7] Daniel R. Baker et al. “Measurement of Oxygen Transport Resistance in PEM Fuel Cells by Limiting Current Methods”. In: *Journal of The Electrochemical Society* 156.9 (Sept. 2009), B991. ISSN: 00134651. DOI: 10.1149/1.3152226.
- [8] Daniel R. Baker et al. “The Use of Limiting Current to Determine Transport Resistance in PEM Fuel Cells”. In: *ECS Transactions*. ECS, 2006. DOI: 10.1149/1.2356218.

- [9] Dustin Banham and Siyu Ye. “Current status and future development of catalyst materials and catalyst layers for proton exchange membrane fuel cells: an industrial perspective”. In: *ACS Energy Letters* 2.3 (2017), pp. 629–638.
- [10] J.J Baschuk and Xianguo Li. “Modelling of polymer electrolyte membrane fuel cells with variable degrees of water flooding”. In: *Journal of Power Sources* 86.1-2 (Mar. 2000), pp. 181–196.
- [11] David J Bents et al. “Hydrogen-oxygen PEM regenerative fuel cell development at Nasa Glenn Research Center”. In: *Fuel Cells Bulletin* 2006.1 (2006), pp. 12–14.
- [12] Jay Benziger et al. “Water flow in the gas diffusion layer of PEM fuel cells”. In: *Journal of Membrane Science* 261.1-2 (2005), pp. 98–106.
- [13] Dawn M. Bernardi. “A Mathematical Model of the Solid-Polymer-Electrolyte Fuel Cell”. In: *Journal of The Electrochemical Society* 139.9 (1992), p. 2477.
- [14] Dawn M. Bernardi and Mark W. Verbrugge. “Mathematical model of a gas diffusion electrode bonded to a polymer electrolyte”. In: *AIChE Journal* 37.8 (Aug. 1991), pp. 1151–1163.
- [15] T Berning and N Djilali. “A 3D, multiphase, multicomponent model of the cathode and anode of a PEM fuel cell”. In: *Journal of the Electrochemical Society* 150.12 (2003), A1589–A1598.
- [16] Torsten Berning, DM Lu, and N Djilali. “Three-dimensional computational analysis of transport phenomena in a PEM fuel cell”. In: *Journal of power sources* 106.1-2 (2002), pp. 284–294.
- [17] Robert Bock et al. “Experimental Study of Thermal Conductivity and Compression Measurements of the GDL-MPL interfacial composite region”. In: *ECS Transactions* 75.14 (2016), pp. 189–199.
- [18] Odne S Burheim et al. “Through-plane thermal conductivity of PEMFC porous transport layers”. In: *Journal of Fuel Cell Science and Technology* 8.2 (2011), p. 021013.
- [19] Zachary P. Cano et al. “Batteries and fuel cells for emerging electric vehicle markets”. In: *Nature Energy* 3.4 (Apr. 2018), pp. 279–289. ISSN: 2058-7546.

- [20] DA Caulk, AM Brenner, and SM Clapham. “A steady permeation method for measuring water transport properties of fuel cell membranes”. In: *Journal of The Electrochemical Society* 159.9 (2012), F518.
- [21] David A Caulk and Daniel R Baker. “Heat and water transport in hydrophobic diffusion media of PEM fuel cells”. In: *Journal of The Electrochemical Society* 157.8 (2010), B1237–B1244.
- [22] David A Caulk and Daniel R Baker. “Modeling two-phase water transport in hydrophobic diffusion media for PEM fuel cells”. In: *Journal of The Electrochemical Society* 158.4 (2011), B384–B393.
- [23] Firat C Cetinbas and Rajesh K Ahluwalia. “Agglomerates in polymer electrolyte fuel cell electrodes: Part II. Transport characterization”. In: *Journal of The Electrochemical Society* 165.13 (2018), F1059–F1066.
- [24] Firat C Cetinbas et al. “Effects of porous carbon morphology, agglomerate structure and relative humidity on local oxygen transport resistance”. In: *Journal of The Electrochemical Society* 167.1 (2020), p. 013508.
- [25] Firat C Cetinbas et al. “Hybrid approach combining multiple characterization techniques and simulations for microstructural analysis of proton exchange membrane fuel cell electrodes”. In: *Journal of Power Sources* 344 (2017), pp. 62–73.
- [26] Sudarshan L. Chavan and Dhananjay B. Talange. “Modeling and performance evaluation of PEM fuel cell by controlling its input parameters”. In: *Energy* 138 (Nov. 2017), pp. 437–445.
- [27] S. Chevalier, C. Josset, and B. Auvity. “Analytical solutions and dimensional analysis of pseudo 2D current density distribution model in PEM fuel cells”. In: *Renewable Energy* 125 (Sept. 2018), pp. 738–746.
- [28] Po-Ya Abel Chuang et al. “The interactive effect of heat and mass transport on water condensation in the gas diffusion layer of a proton exchange membrane fuel cell”. In: *Journal of Power Sources* 480 (2020), p. 229121.
- [29] Prodip K. Das, Xianguo Li, and Zhong-Sheng Liu. “Analysis of liquid water transport in cathode catalyst layer of PEM fuel cells”. In: *International Journal of Hydrogen Energy* 35.6 (Mar. 2010), pp. 2403–2416.

- [30] Prodip K. Das, Xianguo Li, and Zhong-Sheng Liu. “Analytical approach to polymer electrolyte membrane fuel cell performance and optimization”. In: *Journal of Electroanalytical Chemistry* 604.2 (June 2007), pp. 72–90.
- [31] Yulong Ding, Xiaotao Bi, and David P Wilkinson. “3D simulations of the impact of two-phase flow on PEM fuel cell performance”. In: *Chemical Engineering Science* 100 (2013), pp. 445–455.
- [32] Yulong Ding et al. “Simulations of two-phase flow distribution in communicating parallel channels for a PEM fuel cell”. In: *International Journal of Multiphase Flow* 52 (2013), pp. 35–45.
- [33] Nedjib Djilali and Dongming Lu. “Influence of heat transfer on gas and water transport in fuel cells”. In: *International Journal of Thermal Sciences* 41.1 (2002), pp. 29–40.
- [34] M. Eikerling and A.A. Kornyshev. “Modelling the performance of the cathode catalyst layer of polymer electrolyte fuel cells”. In: *Journal of Electroanalytical Chemistry* 453.1-2 (Aug. 1998), pp. 89–106.
- [35] Kathi Epping Martin, John P Kopasz, and Kevin W McMurphy. “Status of fuel cells and the challenges facing fuel cell technology today”. In: *Fuel cell chemistry and operation*. ACS Publications, 2010, pp. 1–13.
- [36] D.S. Falcao et al. “Water transport through a PEM fuel cell: A one-dimensional model with heat transfer effects”. In: *Chemical Engineering Science* 64.9 (May 2009), pp. 2216–2225.
- [37] Rui B Ferreira et al. “1D+ 3D two-phase flow numerical model of a proton exchange membrane fuel cell”. In: *Applied Energy* 203 (2017), pp. 474–495.
- [38] Rui B Ferreira et al. “A one-dimensional and two-phase flow model of a proton exchange membrane fuel cell”. In: *Journal of Chemical Technology & Biotechnology* 90.9 (Sept. 2015), pp. 1547–1551.
- [39] Thomas F Fuller and John Newman. “Experimental determination of the transport number of water in Nafion 117 membrane”. In: *Journal of the Electrochemical Society* 139.5 (1992), p. 1332.

- [40] Thomas F Fuller and John Newman. “Water and thermal management in solid-polymer-electrolyte fuel cells”. In: *Journal of the Electrochemical Society* 140.5 (1993), p. 1218.
- [41] Shanhai Ge, Baolian Yi, and Pingwen Ming. “Experimental determination of electro-osmotic drag coefficient in Nafion membrane for fuel cells”. In: *Journal of The Electrochemical Society* 153.8 (2006), A1443.
- [42] Dietmar Gerteisen et al. “Effect of operating conditions on current density distribution and high frequency resistance in a segmented PEM fuel cell”. In: *international journal of hydrogen energy* 37.9 (2012), pp. 7736–7744.
- [43] Jeffrey T Gostick et al. “Capillary pressure and hydrophilic porosity in gas diffusion layers for polymer electrolyte fuel cells”. In: *Journal of power sources* 156.2 (2006), pp. 375–387.
- [44] Shimshon Gottesfeld and Tom A Zawodzinski. “Polymer electrolyte fuel cells”. In: *Advances in electrochemical science and engineering* 5 (1997), pp. 195–302.
- [45] Thomas A Greszler, David Caulk, and Puneet Sinha. “The impact of platinum loading on oxygen transport resistance”. In: *Journal of The Electrochemical Society* 159.12 (2012), F831.
- [46] W Gu et al. “Proton exchange membrane fuel cell (PEMFC) down-the-channel performance model”. In: *Handbook of Fuel Cells* (2010).
- [47] W. Gu et al. “Proton exchange membrane fuel cell (PEMFC) down-the-channel performance model”. In: *Handbook of Fuel Cells*. Chichester, UK: John Wiley & Sons, Ltd, Dec. 2010. ISBN: 9780470974001.
- [48] Vladimir Gurau, Frano Barbir, and Hongtan Liu. “An Analytical Solution of a Half-Cell Model for PEM Fuel Cells”. In: *Journal of The Electrochemical Society* 147.7 (July 2000), p. 2468.
- [49] Vladimir Gurau, Thomas A. Zawodzinski, and J. Adin Mann. “Two-Phase Transport in PEM Fuel Cell Cathodes”. In: *Journal of Fuel Cell Science and Technology* 5.2 (Apr. 2008).

- [50] Shaker Haji. “Analytical modeling of PEM fuel cell i–V curve”. In: *Renewable Energy* 36.2 (Feb. 2011), pp. 451–458. DOI: 10.1016/J.RENENE.2010.07.007.
- [51] PJ Hamilton and BG Pollet. “Polymer electrolyte membrane fuel cell (PEMFC) flow field plate: design, materials and characterisation”. In: *Fuel cells* 10.4 (2010), pp. 489–509.
- [52] Guangli He et al. “A two-fluid model for two-phase flow in PEMFCs”. In: *Journal of Power Sources* 163.2 (Jan. 2007), pp. 864–873.
- [53] Wensheng He, Jung S Yi, and Trung Van Nguyen. “Two-phase flow model of the cathode of PEM fuel cells using interdigitated flow fields”. In: *AIChE Journal* 46.10 (2000), pp. 2053–2064.
- [54] Bo Ki Hong and Sae Hoon Kim. “Recent advances in fuel cell electric vehicle technologies of Hyundai”. In: *ECS Transactions* 86.13 (2018), p. 3.
- [55] Elham Hosseinzadeh and Masoud Rokni. “Development and Validation of a Simple Analytical Model of the Proton Exchange Membrane Fuel Cell (PEMFC) in a Fork-Lift Truck Power System”. In: *International Journal of Green Energy* 10.5 (May 2013), pp. 523–543.
- [56] Tim Hsu et al. “High performance modeling of heterogeneous SOFC electrode microstructures using the MOOSE framework: ERMINE (Electrochemical Reactions in Microstructural Networks)”. In: *MethodsX* 7 (2020), p. 100822.
- [57] Mingruo Hu et al. “Three dimensional, two phase flow mathematical model for PEM fuel cell: Part II. Analysis and discussion of the internal transport mechanisms”. In: *Energy Conversion and Management* 45.11-12 (July 2004), pp. 1883–1916.
- [58] J. J. Hwang. “Heat Transfer in a Porous Electrode of Fuel Cells”. In: *Journal of Heat Transfer* 128.5 (Oct. 2005), pp. 434–443.
- [59] J. J. Hwang. “Thermal-Electrochemical Modeling of a Proton Exchange Membrane Fuel Cell”. In: *Journal of The Electrochemical Society* 153.2 (2006), A216.
- [60] J.J. Hwang. “A complete two-phase model of a porous cathode of a PEM fuel cell”. In: *Journal of Power Sources* 164.1 (Jan. 2007), pp. 174–181.

- [61] Jenn-Jiang Hwang. “Sustainability study of hydrogen pathways for fuel cell vehicle applications”. In: *Renewable and Sustainable Energy Reviews* 19 (2013), pp. 220–229.
- [62] M Ise, KD Kreuer, and J Maier. “Electroosmotic drag in polymer electrolyte membranes: an electrophoretic NMR study”. In: *Solid State Ionics* 125.1-4 (1999), pp. 213–223.
- [63] Hyunchul Ju, Hua Meng, and Chao-Yang Wang. “A single-phase, non-isothermal model for PEM fuel cells”. In: *International Journal of Heat and Mass Transfer* 48.7 (Mar. 2005), pp. 1303–1315. DOI: 10.1016/j.ijheatmasstransfer.2004.10.004.
- [64] S Yi Jung and Trung V Nguyen. “An along-the-channel model for proton exchange membrane fuel cells”. In: *Journal of the Electrochemical Society* 145.4 (1998), p. 1149.
- [65] Satish G Kandlikar and Zijie Lu. “Thermal management issues in a PEMFC stack—A brief review of current status”. In: *Applied Thermal Engineering* 29.7 (2009), pp. 1276–1280.
- [66] N Khajeh-Hosseini-Dalasm, Kazuyoshi Fushinobu, and Ken Okazaki. “Three-dimensional transient two-phase study of the cathode side of a PEM fuel cell”. In: *International journal of hydrogen energy* 35.9 (2010), pp. 4234–4246.
- [67] Manish Khandelwal and MM Mench. “Direct measurement of through-plane thermal conductivity and contact resistance in fuel cell materials”. In: *Journal of Power Sources* 161.2 (2006), pp. 1106–1115.
- [68] Manish Khandelwal and MM Mench. “Direct measurement of through-plane thermal conductivity and contact resistance in fuel cell materials”. In: *Journal of Power Sources* 161.2 (2006), pp. 1106–1115.
- [69] Vinaykumar Konduru and Jeffrey S Allen. “Material and Morphological Heat Transfer Properties of Fuel Cell Porous Transport Layers”. In: *Journal of The Electrochemical Society* 164.13 (2017), F1316.
- [70] Anusorn Kongkanand, Wenbin Gu, and Mark F Mathias. *Proton-Exchange Membrane Fuel Cells with Low-Pt Content*. Tech. rep. General Motors Global Propulsion Systems Pontiac, Pontiac, MI (United States), 2017.

- [71] Anusorn Kongkanand and Mark F Mathias. “The priority and challenge of high-power performance of low-platinum proton-exchange membrane fuel cells”. In: *The journal of physical chemistry letters* 7.7 (2016), pp. 1127–1137.
- [72] A.A. Kornyshev and A.A. Kulikovsky. “Characteristic length of fuel and oxygen consumption in feed channels of polymer electrolyte fuel cells”. In: *Electrochimica Acta* 46.28 (Aug. 2001), pp. 4389–4395.
- [73] A. A. Kulikovsky. “Catalyst Layer Performance in PEM Fuel Cell: Analytical Solutions”. In: *Electrocatalysis* 3.2 (Mar. 2012), pp. 132–138.
- [74] A. A. Kulikovsky. “Dead Spot in the PEM Fuel Cell Anode”. In: *Journal of The Electrochemical Society* 160.4 (2013), F401–F405.
- [75] A.A. Kulikovsky. “Heat transport in a PEFC: Exact solutions and a novel method for measuring thermal conductivities of the catalyst layers and membrane”. In: *Electrochemistry Communications* 9.1 (Jan. 2007), pp. 6–12.
- [76] A.A. Kulikovsky. “Semi-analytical 1D model of a polymer electrolyte fuel cell”. In: *Electrochemistry Communications* 6.10 (Oct. 2004), pp. 969–977.
- [77] A.A. Kulikovsky and J. McIntyre. “Heat flux from the catalyst layer of a fuel cell”. In: *Electrochimica Acta* 56.25 (Oct. 2011), pp. 9172–9179.
- [78] AA Kulikovsky. “The effect of stoichiometric ratio λ on the performance of a polymer electrolyte fuel cell”. In: *Electrochimica Acta* 49.4 (2004), pp. 617–625.
- [79] EC Kumbur, KV Sharp, and MM Mench. “A design tool for predicting the capillary transport characteristics of fuel cell diffusion media using an artificial neural network”. In: *Journal of Power Sources* 176.1 (2008), pp. 191–199.
- [80] EC Kumbur, KV Sharp, and MM Mench. “Validated Leverett approach for multiphase flow in PEFC diffusion media I. Hydrophobicity effect”. In: *Journal of the Electrochemical Society* 154.12 (2007), B1295–B1304.
- [81] EC Kumbur, KV Sharp, and MM Mench. “Validated Leverett approach for multiphase flow in PEFC diffusion media II. Compression effect”. In: *Journal of the Electrochemical Society* 154.12 (2007), B1305–B1314.

- [82] Ahmet Kusoglu and Adam Z Weber. “New insights into perfluorinated sulfonic-acid ionomers”. In: *Chemical reviews* 117.3 (2017), pp. 987–1104.
- [83] M.C. Leverett. “Capillary Behavior in Porous Solids”. In: *Transactions of the AIME* 142.01 (Dec. 1941), pp. 152–169.
- [84] Guangyu Lin, Wensheng He, and Trung Van Nguyen. “Modeling Liquid Water Effects in the Gas Diffusion and Catalyst Layers of the Cathode of a PEM Fuel Cell”. In: *Journal of The Electrochemical Society* 151.12 (2004), A1999.
- [85] Vincenzo Liso et al. “Modeling and experimental validation of water mass balance in a PEM fuel cell stack”. In: *International Journal of Hydrogen Energy* 41.4 (Jan. 2016), pp. 3079–3092.
- [86] S Litster and G McLean. “PEM fuel cell electrodes”. In: *Journal of power sources* 130.1-2 (2004), pp. 61–76.
- [87] S Litster, D Sinton, and N Djilali. “Ex situ visualization of liquid water transport in PEM fuel cell gas diffusion layers”. In: *Journal of Power Sources* 154.1 (2006), pp. 95–105.
- [88] S Litster et al. “Morphological analyses of polymer electrolyte fuel cell electrodes with nano-scale computed tomography imaging”. In: *Fuel Cells* 13.5 (2013), pp. 935–945.
- [89] Jia Xing Liu et al. “Two-dimensional analytical model of a proton exchange membrane fuel cell”. In: *Energy* 119 (Jan. 2017), pp. 299–308. ISSN: 0360-5442. DOI: 10.1016/J.ENERGY.2016.12.075.
- [90] Xunliang Liu, Guofeng Lou, and Zhi Wen. “Three-dimensional two-phase flow model of proton exchange membrane fuel cell with parallel gas distributors”. In: *Journal of Power Sources* 195.9 (2010), pp. 2764–2773.
- [91] Yuxiu Liu et al. “Proton Conduction and Oxygen Reduction Kinetics in PEM Fuel Cell Cathodes: Effects of Ionomer-to-Carbon Ratio and Relative Humidity”. In: *Journal of The Electrochemical Society* 156.8 (2009), B970.
- [92] G Maggio, V Recupero, and L Pino. “Modeling polymer electrolyte fuel cells: an innovative approach”. In: *Journal of Power Sources* 101.2 (Oct. 2001), pp. 275–286.

- [93] Erasmo Mancusi et al. “Numerical study of two-phase flow patterns in the gas channel of PEM fuel cells with tapered flow field design”. In: *International journal of hydrogen energy* 39.5 (2014), pp. 2261–2273.
- [94] Ronald F. Mann et al. “Development and application of a generalised steady-state electrochemical model for a PEM fuel cell”. In: *Journal of Power Sources* 86.1-2 (Mar. 2000), pp. 173–180.
- [95] C Marr and X Li. “An engineering model of proton exchange membrane fuel cell performance”. In: *ARI-An International Journal for Physical and Engineering Sciences* 50.4 (1997), pp. 190–200.
- [96] Curtis Marr and Xianguo Li. “Composition and performance modelling of catalyst layer in a proton exchange membrane fuel cell”. In: *Journal of Power Sources* 77.1 (Jan. 1999), pp. 17–27.
- [97] Minoru Matsunaga, Tatsuya Fukushima, and Kuniaki Ojima. “Powertrain system of Honda FCX Clarity fuel cell vehicle”. In: *World Electric Vehicle Journal* 3.4 (2009), pp. 820–829.
- [98] Cortney K Mittelsteadt and John Staser. “Simultaneous water uptake, diffusivity and permeability measurement of perfluorinated sulfonic acid polymer electrolyte membranes”. In: *ECS Transactions* 41.1 (2011), pp. 101–121.
- [99] F Mojica et al. “Experimental Study of Three Channel Designs with Model Comparison in a PEM Fuel Cell”. In: *Fuel Cells* 20.5 (2020), pp. 547–557.
- [100] Sathya Motupally, Aaron J Becker, and John W Weidner. “Diffusion of water in Nafion 115 membranes”. In: *Journal of the Electrochemical Society* 147.9 (2000), p. 3171.
- [101] Dilip Natarajan and Trung Van Nguyen. “Three-dimensional effects of liquid water flooding in the cathode of a PEM fuel cell”. In: *Journal of power sources* 115.1 (2003), pp. 66–80.
- [102] K. C. Neyerlin et al. “Cathode Catalyst Utilization for the ORR in a PEMFC”. In: *Journal of The Electrochemical Society* 154.2 (Feb. 2007), B279.

- [103] K. C. Neyerlin et al. “Effect of Relative Humidity on Oxygen Reduction Kinetics in a PEMFC”. In: *Journal of The Electrochemical Society* 152.6 (2005), A1073. DOI: 10.1149/1.1897368.
- [104] Phong Thanh Nguyen, Torsten Berning, and Ned Djilali. “Computational model of a PEM fuel cell with serpentine gas flow channels”. In: *Journal of Power Sources* 130.1-2 (2004), pp. 149–157.
- [105] Trung V. Nguyen and Ralph E. White. “A Water and Heat Management Model for Proton-Exchange-Membrane Fuel Cells”. In: *Journal of The Electrochemical Society* 140.8 (Aug. 1993), p. 2178. ISSN: 00134651. DOI: 10.1149/1.2220792.
- [106] Ryan O’hayre et al. *Fuel cell fundamentals*. John Wiley & Sons, 2016.
- [107] Tatsuhiko Okada, Gang Xie, and Yoshikazu Tanabe. “Theory of water management at the anode side of polymer electrolyte fuel cell membranes”. In: *Journal of Electroanalytical Chemistry* 413.1-2 (Sept. 1996), pp. 49–65. ISSN: 1572-6657.
- [108] Hossein Ostadi et al. “3D reconstruction of a gas diffusion layer and a microporous layer”. In: *Journal of Membrane Science* 351.1-2 (2010), pp. 69–74.
- [109] JP Owe01 et al. “Investigation of micro-and macro-scale transport processes for improved fuel cell performance”. In: *FY 2011 Annual Progress Report, DOE Hydrogen and Fuel Cells Program* (2011), pp. 827–832.
- [110] Lalit M Pant et al. “Along-the-channel modeling and analysis of PEFCs at low stoichiometry: Development of a 1+ 2D model”. In: *Electrochimica Acta* 326 (2019), p. 134963.
- [111] N Parikh, JS Allen, and RS Yassar. “Microstructure of gas diffusion layers for PEM fuel cells”. In: *Fuel Cells* 12.3 (2012), pp. 382–390.
- [112] Sehkyu Park, Jong-Won Lee, and Branko N Popov. “A review of gas diffusion layer in PEM fuel cells: Materials and designs”. In: *International Journal of Hydrogen Energy* 37.7 (2012), pp. 5850–5865.
- [113] U Pasaogullari. “Heat and water transport models for polymer electrolyte fuel cells”. In: *Handbook of Fuel Cells* (2010).

- [114] Ugur Pasaogullari and Chao-Yang Wang. “Two-Phase Modeling and Flooding Prediction of Polymer Electrolyte Fuel Cells”. In: *Journal of The Electrochemical Society* 152.2 (2005), A380.
- [115] Ugur Pasaogullari and Chao-Yang Wang. “Two-phase transport and the role of micro-porous layer in polymer electrolyte fuel cells”. In: *Electrochimica Acta* 49.25 (2004), pp. 4359–4369.
- [116] Ugur Pasaogullari and CY Wang. “Liquid Water Transport in Gas Diffusion Layer of Polymer Electrolyte Fuel Cells”. In: *Journal of The Electrochemical Society* 151.3 (2004), A399–A406.
- [117] Ashok S Patil et al. “Portable fuel cell systems for America’s army: technology transition to the field”. In: *Journal of Power Sources* 136.2 (2004), pp. 220–225.
- [118] Peng Quan and Ming-Chia Lai. “Numerical study of water management in the air flow channel of a PEM fuel cell cathode”. In: *Journal of Power Sources* 164.1 (2007), pp. 222–237.
- [119] Paria Rahimian, Ryan Anderson, and Lifeng Zhang. “Predictions of flow regimes in proton exchange membrane fuel cells: An analytical approach”. In: *International Journal of Hydrogen Energy* 42.7 (Feb. 2017), pp. 4679–4689.
- [120] Md Azimur Rahman et al. “Development of 1-D multiphysics PEMFC model with dry limiting current experimental validation”. In: *Electrochimica Acta* 320 (2019), p. 134601.
- [121] Srinivasan Raman et al. “Effects of water induced pore blockage and mitigation strategies in low temperature PEM fuel cells – A simulation study”. In: *International Journal of Hydrogen Energy* 42.37 (2017), pp. 23799–23813.
- [122] Julien Ramousse et al. “Modelling of heat, mass and charge transfer in a PEMFC single cell”. In: *Journal of Power Sources* 145.2 (2005), pp. 416–427.
- [123] Xiaoming Ren et al. “Methanol transport through nation membranes. electro-osmotic drag effects on potential step measurements”. In: *Journal of the Electrochemical Society* 147.2 (2000), p. 466.

- [124] J. Antonio Salva et al. “Validation of cell voltage and water content in a PEM (polymer electrolyte membrane) fuel cell model using neutron imaging for different operating conditions”. In: *Energy* 101 (Apr. 2016), pp. 100–112.
- [125] Denise Rocco de Sena et al. “Effect of water transport in a PEFC at low temperatures operating with dry hydrogen”. In: *Journal of Electroanalytical Chemistry* 477.2 (1999), pp. 164–170.
- [126] O. Shamardina et al. “A simple model of a high temperature PEM fuel cell”. In: *International Journal of Hydrogen Energy* 35.18 (Sept. 2010), pp. 9954–9962. DOI: 10.1016/J.IJHYDENE.2009.11.012.
- [127] Chao Si et al. “Gas diffusion layer properties on the performance of proton exchange membrane fuel cell: pc-s relationship with K-function”. In: *International Journal of Hydrogen Energy* 41.46 (Dec. 2016), pp. 21827–21837.
- [128] Christoph Simon, Frédéric Hasché, and Hubert A Gasteiger. “Influence of the gas diffusion layer compression on the oxygen transport in PEM fuel cells at high water saturation levels”. In: *Journal of The Electrochemical Society* 164.6 (2017), F591–F599.
- [129] B SIVERTSEN and N DJILALI. “CFD-based modelling of proton exchange membrane fuel cells”. In: *Journal of Power Sources* 141.1 (Feb. 2005), pp. 65–78.
- [130] T. E. Springer, T. A. Zawodzinski, and S. Gottesfeld. “Polymer Electrolyte Fuel Cell Model”. In: *Journal of The Electrochemical Society* 138.8 (Aug. 1991), p. 2334. DOI: 10.1149/1.2085971.
- [131] NP Subramanian et al. “Pt-oxide coverage-dependent oxygen reduction reaction (ORR) kinetics”. In: *Journal of The Electrochemical Society* 159.5 (2012), B531.
- [132] Hong Sun, Hongtan Liu, and Lie-Jin Guo. “PEM fuel cell performance and its two-phase mass transport”. In: *Journal of Power Sources* 143.1-2 (Apr. 2005), pp. 125–135.
- [133] Takahisa Suzuki, Kenji Kudo, and Yu Morimoto. “Model for investigation of oxygen transport limitation in a polymer electrolyte fuel cell”. In: *Journal of Power Sources* 222 (2013), pp. 379–389.

- [134] Takahisa Suzuki et al. “Modeling of Oxygen Diffusion Resistance in Polymer Electrolyte Fuel Cells in the Intermediate Potential Region”. In: *Journal of The Electrochemical Society* 165.3 (2018), F166.
- [135] Anthony Thomas et al. “Thermal and water transfer in PEMFCs: investigating the role of the microporous layer”. In: *International Journal of Hydrogen Energy* 39.6 (2014), pp. 2649–2658.
- [136] Eric L. Thompson et al. “PEM Fuel Cell Operation at -20°C . II. Ice Formation Dynamics, Current Distribution, and Voltage Losses within Electrodes”. In: *Journal of The Electrochemical Society* 155.9 (2008), B887.
- [137] CR Tsai et al. “An analytical solution for transport of oxygen in cathode gas diffusion layer of PEMFC”. In: *Journal of power sources* 160.1 (2006), pp. 50–56.
- [138] Kent S Udell. “Heat transfer in porous media considering phase change and capillarity—the heat pipe effect”. In: *International Journal of Heat and Mass Transfer* 28.2 (1985), pp. 485–495.
- [139] Sukkee Um, C-Y Wang, and KS Chen. “Computational fluid dynamics modeling of proton exchange membrane fuel cells”. In: *Journal of the Electrochemical society* 147.12 (2000), p. 4485.
- [140] Sukkee Um and CY Wang. “Three-dimensional analysis of transport and electrochemical reactions in polymer electrolyte fuel cells”. In: *Journal of Power Sources* 125.1 (2004), pp. 40–51.
- [141] Krishna Vijayaraghavan, Jake DeVaal, and Mohammad Narimani. “Dynamic model of oxygen starved proton exchange membrane fuel-cell using hybrid analytical-numerical method”. In: *Journal of Power Sources* 285 (July 2015), pp. 291–302.
- [142] Chao-Yang Wang. “Fundamental Models for Fuel Cell Engineering”. In: *Chemical Reviews* 104.10 (Oct. 2004), pp. 4727–4766.
- [143] Lina Wang et al. “Fe-NC catalysts for PEMFC: Progress towards the commercial application under DOE reference”. In: *Journal of Energy Chemistry* 39 (2019), pp. 77–87.

- [144] ZH Wang, CY Wang, and KS Chen. “Two-phase flow and transport in the air cathode of proton exchange membrane fuel cells”. In: *Journal of power sources* 94.1 (2001), pp. 40–50.
- [145] Marvin Warshay et al. “The NASA fuel cell upgrade program for the space shuttle orbiter”. In: *IECEC-97 Proceedings of the Thirty-Second Intersociety Energy Conversion Engineering Conference (Cat. No. 97CH6203)*. Vol. 1. IEEE. 1997, pp. 228–231.
- [146] Adam Z Weber and John Newman. “Effects of membrane-and catalyst-layer-thickness nonuniformities in polymer-electrolyte fuel cells”. In: *Journal of the Electrochemical Society* 154.4 (2007), B405.
- [147] Adam Z Weber and John Newman. “Effects of microporous layers in polymer electrolyte fuel cells”. In: *Journal of the Electrochemical Society* 152.4 (2005), A677.
- [148] Adam Z Weber et al. “A critical review of modeling transport phenomena in polymer-electrolyte fuel cells”. In: *Journal of The Electrochemical Society* 161.12 (2014), F1254–F1299.
- [149] Adam Z. Weber, Robert M. Darling, and John Newman. “Modeling Two-Phase Behavior in PEFCs”. In: *Journal of The Electrochemical Society* 151.10 (2004), A1715.
- [150] Adam Z. Weber and John Newman. “Coupled Thermal and Water Management in Polymer Electrolyte Fuel Cells”. In: *Journal of The Electrochemical Society* 153.12 (Dec. 2006), A2205. DOI: 10.1149/1.2352039.
- [151] Adam Z. Weber and John Newman. “Effects of Microporous Layers in Polymer Electrolyte Fuel Cells”. In: *Journal of The Electrochemical Society* 152.4 (Apr. 2005), A677.
- [152] Adam Z. Weber and John Newman. “Transport in Polymer-Electrolyte Membranes”. In: *Journal of The Electrochemical Society* 150.7 (July 2003), A1008.
- [153] CR Wilke and CY Lee. “Estimation of diffusion coefficients for gases and vapors”. In: *Industrial & Engineering Chemistry* 47.6 (1955), pp. 1253–1257.
- [154] Minkmas V Williams et al. “Characterization of gas diffusion layers for PEMFC”. In: *Journal of the Electrochemical Society* 151.8 (2004), A1173.

- [155] Lei Xing et al. “A two-phase flow and non-isothermal agglomerate model for a proton exchange membrane (PEM) fuel cell”. In: *Energy* 73 (Aug. 2014), pp. 618–634.
- [156] Jung S Yi, J Deliang Yang, and Constance King. “Water management along the flow channels of PEM fuel cells”. In: *AIChE journal* 50.10 (2004), pp. 2594–2603.
- [157] Toshihiko Yoshida and Koichi Kojima. “Toyota MIRAI fuel cell vehicle and progress toward a future hydrogen society”. In: *The Electrochemical Society Interface* 24.2 (2015), p. 45.
- [158] Lixin You and Hongtan Liu. “A two-phase flow and transport model for the cathode of PEM fuel cells”. In: *International Journal of Heat and Mass Transfer* 45.11 (May 2002), pp. 2277–2287.
- [159] Xiao-Zi Yuan et al. “A review of functions, attributes, properties and measurements for the quality control of proton exchange membrane fuel cell components”. In: *Journal of Power Sources* 491 (2021), p. 229540.
- [160] Thomas A Zawodzinski Jr et al. “Determination of water diffusion coefficients in perfluorosulfonate ionomeric membranes”. In: *The Journal of Physical Chemistry* 95.15 (1991), pp. 6040–6044.
- [161] Tianhong Zhou and Hongtan Liu. “A 3D model for PEM fuel cells operated on reformat”. In: *Journal of Power Sources* 138.1-2 (Nov. 2004), pp. 101–110.